University of Alberta

Quantitative Imaging of Diastolic Function using Cardiac Magnetic Resonance Imaging

by

June Cheng Baron

A thesis submitted to the Faculty of Graduate Studies and Research in partial fulfillment of the requirement for the degree of

Doctor of Philosophy

Medical Sciences – Biomedical Engineering

©June Cheng Baron
Spring 2013
Edmonton, Alberta

Permission is hereby granted to the University of Alberta Libraries to reproduce single copies of this thesis and to lend or sell such copies for private, scholarly or scientific research purposes only. Where the thesis is converted to, or otherwise made available in digital form, the University of Alberta will advise potential users of the thesis of these terms.

The author reserves all other publication and other rights in association with the copyright in the thesis and, except as herein before provided, neither the thesis nor any substantial portion thereof may be printed or otherwise reproduced in any material form whatsoever without the authors prior written permission.

Abstract

Diastolic dysfunction is the primary cause of 40–50% of all heart failure cases and is a contributing factor in many cardiac conditions, resulting from delayed or slowed muscle relaxation, increased stiffness of the relaxed heart or from poor systolic function which reduces the elastic recoil of the heart. The study of diastolic function has been hampered by a lack of simple, quantitative, parameters describing diastolic performance.

The current standard of evaluation consists of echocardiography-derived blood and tissue velocities. Magnetic resonance imaging (MRI) provides better spatial coverage and soft tissue contrast, but is relatively unexplored in the context of diastolic function. Goals of this thesis were to improve current and develop new quantitative measures of diastolic function using MRI.

Left ventricular deformation during isovolumic relaxation was studied to reveal that measured changes in left ventricular volume during this interval reflect changes in myocardial strain and are balanced by the inward bowing of the mitral valve leaflets which maintains the isovolumic condition. Next, aspects of the filling portion of the cardiac cycle were studied including mitral blood velocity and flow, left atrial propagation velocity and atrio-ventricular pressure gradients. Mitral blood velocity and flow were found to have distinct time-courses that become more similar with increasing severity of diastolic dysfunction. Velocity propagation, a wave-like pressure wave phenomenon, was observed in the left atrium during systole, early filling and atrial contraction, providing a new measure of diastolic function reflecting atrial stiffness and pressure. Atrio-ventricular pressure gradients however, were not found to provide additional information beyond blood velocity measures.

Finally, there is growing interest in measuring systolic strain in the pres-

ence diastolic dysfunction with preserved ejection fraction, where strains appear abnormal despite normal volumetric function. Conventional MRI-derived strain requires specialized acquisition protocols and onerous post-processing. A method was developed to measure strains from standard anatomical MRI.

MRI is a promising tool for the comprehensive characterization of diastolic function. However, this field of study is still relatively un-established and further studies, similar to those presented here, in larger patient groups are necessary to establish the role of MRI for diastolic function in research and clinically.

Acknowledgments

I would like to acknowledge the financial support, throughout my degree, of the Natural Sciences and Engineering Research Council (NSERC), the Department of Biomedical Engineering and the University of Alberta. Funding for operational grants has been provided by the Canadian Institutes of Health Research (CIHR), the Alberta Heritage Foundation for Medical Research (AHFMR) and the Alberta Heart Failure Etiology and Analysis Research Team (Alberta HEART) team grant. I would also like to thank the many volunteers that have contributed their time and collectively endured many hours of breath-holding in order to make this research possible.

I have been lucky enough to have spent my degree working in an environment with caring and encouraging fellow students, enthusiastic and approachable professors and helpful administrative staff. You have made my experience here incredibly positive and memorable. I would specifically like to thank the graduate students with whom I have worked most closely — Kelvin Chow, Joseph Pagano and Kory Mathewson. I am incredibly grateful for all of the scanning you do, the numerous discussions (work-related or not), the drafts of papers returned with every typo and inconsistency noted and for the many cups of coffee.

Thank you to my supervisor, Richard Thompson. I have gone from knowing absolutely nothing about research and cardiac MRI to knowing enough to make people think I might know something. You have been a wonderful teacher and I truly appreciate all the guidance you have provided me with throughout my degree. Your enthusiasm for research is inspiring. I would also like to thank my supervisory committee, Mark Haykowsky and Alan Wilman, for always being accessible and for providing constructive feedback whenever

necessary.

It has been a pleasure to work with the many collaborators who have contributed ideas, time and effort to the studies conducted throughout my degree. I have learned so much by working with people of diverse academic backgrounds. Particularly, I would like to thank Ian Paterson, who has enabled so much of this thesis and who always takes the opportunity for a teaching moment.

I would like to thank my friends and family for pretending to be interested when I talk about my research. Thank you also for providing me with encouragement, sympathy and plenty to reasons to (occasionally!) neglect my work.

This thesis would not have been possible without my parents. Your unwavering confidence and support along with your (sometimes brutally) honest criticisms have taught me to always strive to be better and not to be afraid of failing.

Finally, I would like to give my most heartfelt thanks to my husband Corey. Thank you for listening to me practice talks over and over, for reading numerous research proposals and papers, for being an excellent volunteer when necessary and for discussing my latest MRI problem with me over dinner. Thank you especially, for sharing in my successes, helping me through the lows, calming me down when I'm stressed and for all of the times in between.

Table of Contents

List of Tables

List of Figures

List of Abbreviations

A-wave	atrial contraction
AF	atrial fibrillation
ANOVA	analysis of variance
AVC	aortic valve closure
AVO	aortic valve opening
BSA	body surface area
bpm	beats per minute
BW	bandwidth
CNR	contrast to noise
COV	coefficient of variation
CT	computed tomography
D-wave	diastolic left atrial filling
HF	heart failure
E-wave	early filling
ECG	electrocardiogram
ED	end-diastole
EDV	end-diastolic volume
EF	ejection fraction
epi	epicardium, epicardial
endo	endocardium, endocardial
ESV	end-systolic volume
f	female
FLASH	fast low-angle shot
FOV	field of view
GRAPPA	generalized autocalibrating partially parallel acquisitions
ICC	interclass correlation coefficient
IVPD	intra-ventricular pressure difference
IVPG	intra-ventricular pressure gradient
IVR	isovolumic relaxation
IVRT	isovolumic relaxation time
LA	left atrium
LV	left ventricle
m	male
MRI	magnetic resonance imaging
MVC	mitral valve closure
MVO	mitral valve opening
PWV	pulse wave velocity
RA	right atrium
RV	right ventricle
S-wave	systolic left atrial filling
SPECT	single-photon emmision computed tomography

SNR	signal to noise
SPAMM	spatial modulation of magnetization
SSFP	steady state free precession
TE	echo time
TR	repetition time
vel	velocity
VPS	views per segment
vol	volume
yrs	years of age

List of Symbols

a	length of left ventricular long-axis
A	peak A-wave velocity
A'	mitral annular velocity during early filling
Ar	pulmonary venous retrograde flow during atrial contraction
b	short-axis radius of left ventricular base
D	early diastolic pulmonary venous velocity
d	distance
E	peak E-wave velocity
E'	mitral annular velocity during early filling
E_{cc}	global circumferential strain
E_{ll}	global longitudinal strain
E_{rr}	global radial strain
$\dot{E}_{cc}$	global circumferential strain rate
$\dot{E}_{ll}$	global longitudinal strain rate
$\dot{E}_{rr}$	global radial strain rate
G	magnetic field gradient
G_b	magnitude of bipolar gradient
G_m	magnitude of modulation gradient
n, N	total number
P	pressure
$P_\circ$	initial pressure
S	systolic pulmonary venous velocity
t	time
T_1	spin-lattice relaxation time
T_2	spin-spin relaxation time
T_A	time of A-wave peak
T_b	time-duration of 1 bipolar gradient lobe
T_E	time of E-wave peak
T_m	time-duration of modulation gradient
v	velocity
$\vec{v_1}$, $\vec{v_2}$	magnetization vectors
V	volume

V_e	volume of a half-ellipsoid
x, y, z	space
$x_\circ$	initial position
α	radiofrequency excitation pulse
Δ	difference
ϵ	strain
ϕ	phase
θ	rotation angle
γ	gyromagnetic ratio
Γ	eccentricity
ρ	density
τ	time constant of left ventricular isovolumic pressure decline

Chapter 1

Introduction

1.1 Overview

Imaging is an important tool for diagnosis, the monitoring of disease progression and the study of the mechanisms of cardiac diseases. Commonly used imaging modalities include including echocardiography [1–3], x-ray angiography [4], positron emission tomography (PET) [5], single-photon emission computed tomography (SPECT) [6], x-ray computed tomography (CT) [1, 4] and magnetic resonance imaging (MRI) [1, 4]. MRI and echocardiography are appealing imaging modalities because they both use non-ionizing radiation. MRI has the additional advantage of excellent soft tissue contrast, more available contrast mechanisms and unrestricted imaging windows. These advantages have made MRI the preferred method for the quantification of cardiac chamber volumes and masses [7–9].

Chamber volumes are used to calculate ejection fraction (EF), the percentage of blood ejected by the left ventricle (LV) per heartbeat relative to its maximum volume. EF is the most commonly reported measure of cardiac function and is often interpreted as a direct measure of systolic function, i.e.

performance of the heart as a pump [10]. It is an appealing parameter because it represents global whole heart function, has direct physical meaning and can be measured non-invasively.

In the past, researchers and clinicians have focused on systolic function to evaluate cardiac performance. However, there is now growing interest in diastolic function, i.e. the filling function of the heart, and its role in heart failure as well as other cardiac diseases [11–14]. It is now accepted that diastolic dysfunction is the primary cause of 40% to 50% of heart failure cases [15] and is a contributing factor in many cardiac conditions including hypertension [12], myocardial ischemia [16] and diabetes [17, 18]. Heart failure, in particular, is the final stage of many cardiac conditions and refers to a physiological state where the heart is unable to efficiently supply blood to the body [19, 20]. It affects an estimated 23 million worldwide and 5.8 million in the United States alone [20, 21]. The prognosis for individuals with heart failure is poor with a 5 year survival rate of 59% for men and 45% for women [19].

Diastole refers to the portion of the cardiac cycle associated with relaxation and filling of the ventricles. Normal diastolic function results in adequate preload, or stretch of the muscle fibers, for ejection as described by the Frank-Starling mechanism and does so at low filling pressures. Abnormal diastolic function, meaning inadequate filling or the need for high diastolic pressures to achieve filling, can occur if the heart chambers have impaired relaxation or increased stiffness. This causes a backup of blood returning to the heart and elevated filling pressures [14, 22, 23]. These elevated pressures, if high enough, lead to a host of problems including pulmonary edema caused by elevated capillary pressure and, if maintained for long enough, mal-adaptive structural changes in heart morphology.

Thus, to understand the different etiologies of heart failure and, with

the ultimate goal of decreasing prevalence and improving prognosis, it is important to study diastolic dysfunction associated with heart failure and other cardiac conditions that precede heart failure. With better understanding of cardiac dysfunction, it will be possible to better guide development of new therapies, to provide tools for earlier and more accurate diagnosis of cardiac diseases and to better monitor response to therapy. However, diastolic function is still not well understood and, unlike EF for systolic function, its study has been hampered by a lack of simple and quantitative parameters that describe diastolic performance.

The gold standard measures of diastolic function require the invasive measurement of diastolic pressures and volumes to estimate the stiffness and relaxation properties of the heart and to measure filling pressures [24]. The equipment and expertise for these measures are not widely available, nor is it desirable to perform cardiac catherization whenever diastolic measures are desired, for example, for research purposes or for serial monitoring of diastolic function. As a result, they have only been measured in a small number of research studies and are not measured clinically.

Instead, echocardiography is the most common method for evaluation of diastolic function [3, 25], where abnormal relaxation, stiffness and filling pressures are detected indirectly though patterns and time-courses of tissue deformation and blood velocity. A large number of blood and tissue velocity parameters have been developed using echocardiography to characterize these changes. However, these parameters can be difficult to interpret because they are indirectly related to the mechanisms modulating diastolic function and must be used in combination for the proper assessment of diastolic function.

While cardiac magnetic resonance imaging (MRI) is the preferred method of evaluation for many aspects of systolic function such as EF [8, 9], it remains

relatively unexplored in the context of diastolic function. Echocardiography is preferred because it has simpler image acquisition and superior temporal resolution which enables the measurement of rapid diastolic events. Despite these advantages, certain aspects of diastolic function cannot be studied using echocardiography and are better suited to MRI due to superior image contrast and unrestricted imaging windows. MRI also allows for the more complete spatial characterization of diastolic events. Furthermore, systolic and diastolic dysfunction often occur together, and it is appealing to be able to measure both using a single exam. The over-arching goal of this thesis was to use MRI to improve current and to develop new quantitative imaging parameters of diastolic function.

Throughout this thesis, several imaging strategies available for cardiac MRI were employed to study different aspects of diastolic function. Steady state free precession (SSFP) cine imaging was used to view heart morphology throughout the cardiac cycle. Phase contrast cine imaging was used to determine blood velocity, and tissue tagging cine imaging was employed to track myocardial deformation throughout the cardiac cycle. These imaging strategies are described in Section 1.3 of this chapter. Further background regarding the heart and diastolic function is provided in Sections 1.2 and 1.4 below.

1.2 The Heart

Current knowledge of the heart and cardiovascular system is described in detail in a wide array of textbooks, review articles and multimedia sources. A basic description of heart anatomy and function at the organ level is provided here. Textbook references are used throughout this section as well as in Section 1.4 below [47–49]. Other references are cited within the text, where applicable.

1.2.1 Anatomy of the Heart

The human heart has 4 chambers and is divided by the atrial and ventricular septums into 2 halves, right and left, that pump in unison (Figure 1.1). The right half is responsible for supplying blood to the pulmonary circuit while the left half is responsible for supplying blood to the systemic circuit. The pathway of blood is described as follows: de-oxygenated blood from the body enters the heart through the superior and inferior vena cava. During ventricular systole, it collects in the right atrium (RA) and is then emptied into the right ventricle (RV) during ventricular diastole. The RV then pumps blood to the lungs via the pulmonary arteries during the next systole. Meanwhile, in synchrony with the right heart, oxygenated blood from the lungs returns to the heart through the pulmonary veins and collects in the LA during systole. Blood then empties from the LA into the LV during diastole. Finally, the left ventricle pumps blood out to the body through the aorta during the next systole.

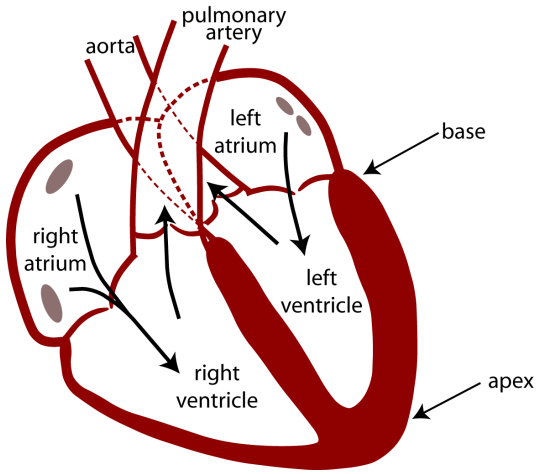

Figure 1.1: Basic anatomy of the heart. Arrows indicate the direction of blood flow.

The atria are thin, elastic chambers that act as reservoirs for blood returning to the heart from the various organs. Blood flow from the atria

to the ventricles occurs largely while the atria are fully relaxed; however, a smaller portion of the blood is delivered to the ventricles by atrial contraction. The ventricles are thicker walled muscular pumps that drive blood circulation. The right ventricle pumps blood to the lungs while the left ventricle must pump to all the remaining organs in the body. As a result it is the thickest, most muscular heart chamber as shown in Figure 1.1. The base of the ventricle refers to the portion of the chamber closest to the atria while the apex refers to the opposite end. The long axis of the heart runs from apex to base.

The heart has 4 valves that prevent blood from flowing in the wrong direction. The mitral and tricuspid valves separate the atria and ventricles on the left and right sides, respectively, and the aortic and pulmonary valves are located in the left and right ventricular outflow tracts. The valves coapt together when closed to prevent retrograde flow. The mitral and tricuspid valves are also attached by chordae tendineae to papillary muscles in the interior of the ventricles to prevent them from turning inside-out during ventricular contraction.

1.2.2 Left Heart Function in the Cardiac Cycle

Isovolumic Contraction

The cardiac cycle can be divided into 2 phases, systole (ventricular contraction) and diastole (ventricular relaxation). Systole can be further divided into isovolumic contraction and ejection, while diastole can be further divided into isovolumic relaxation and filling (Figure 1.2). Immediately prior to systole, the volume of the LV is at its maximum. LV pressure is low, the mitral valve is open and the aortic valve is closed. Systole begins with mitral valve closure (MVC) caused by increasing pressure within the LV chamber as the

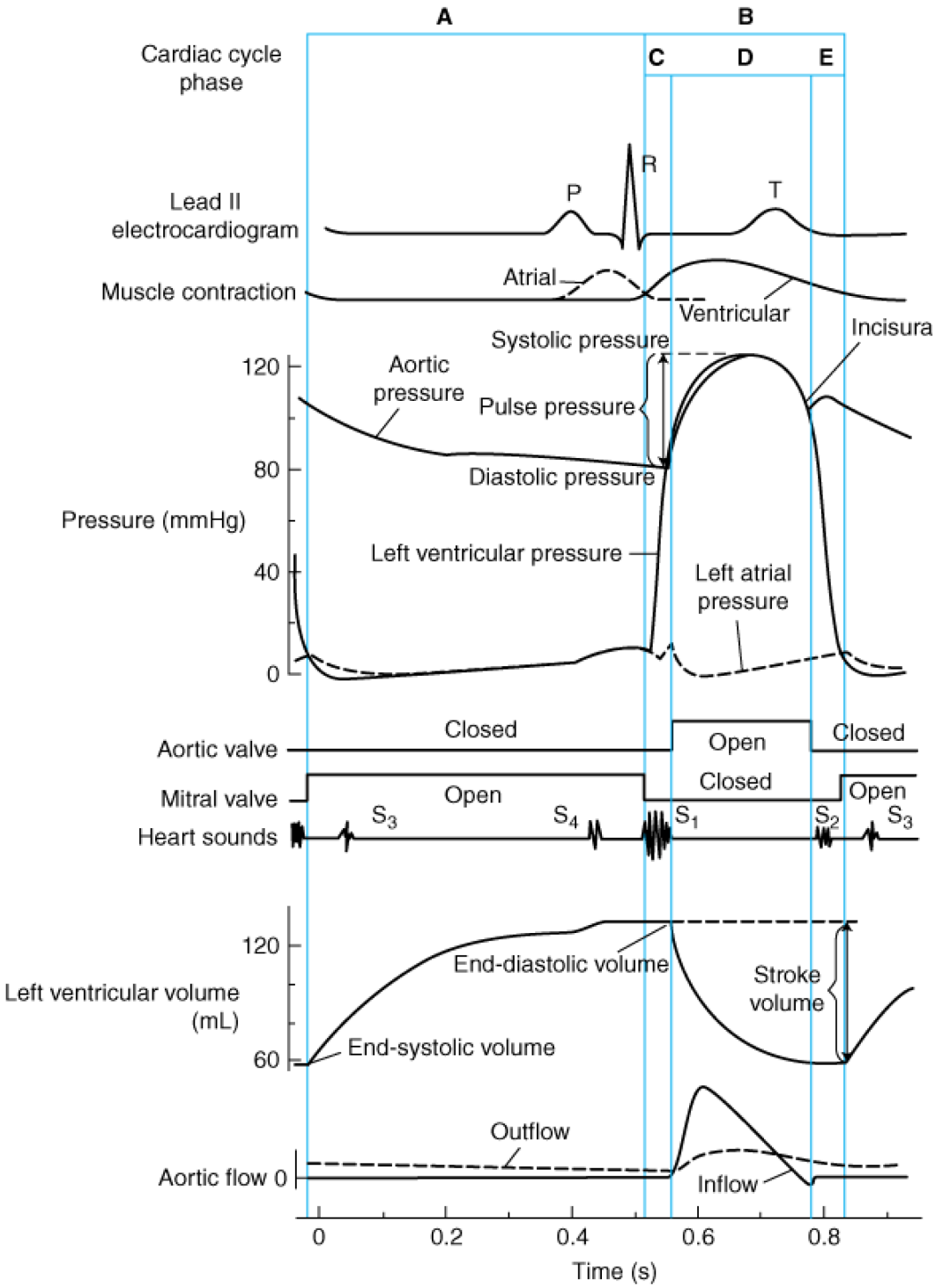

Figure 1.2: The cardiac cycle of the left heart. The cardiac phases are divided into (A) ventricular filling, (C) isovolumic contraction, (D) ejection and (E) isovolumic relaxation. Figure from *Cardiovascular Physiology*, seventh edition [49].

LV begins to contract. When the increasing pressure within the LV exceeds the pressure in the aorta, the aortic valve opens (AVO). The period of time following MVC and preceding AVO is referred to as isovolumic contraction. This phase of the cardiac cycle is characterized by both valves being closed and the volume within the LV being constant.

Ventricular Ejection

Once the aortic valve opens, blood is ejected from the LV causing LV volume to decline. Pressure within the LV however, continues to increase while the LV continues to contract. As more blood is ejected, LV volume continues to decrease, eventually causing LV pressure to fall as well. Aortic valve closure occurs once LV pressure falls below aortic pressure. Ventricular systole occurs simultaneously with atrial filling. During this time, the LA is isolated from LV pressures by the mitral valve. The LA relaxes and fills with blood, which is driven, in part by right ventricular systole causing increased pulmonary pressures and in part by left ventricular myocardial contraction causing the descent of the LV base which expands the LA chamber.

Isovolumic Relaxation

Following AVC, a second isovolumic period occurs where both valves are again closed and LV volume is constant, assuming that neither the mitral nor the aortic valves are leaky. The pressure within the LV declines further, driven by LV myocardial relaxation and elastic recoil. LV relaxation is an active, energy consuming, process requiring calcium removal from the sarcoplasm to release actin-myosin bonds formed during contraction. When LV pressure declines below LA pressure, this causes the mitral valve to open, which indicates the start of ventricular filling and end of IVR.

Ventricular Filling

With the opening of the mitral valve, the LV begins to fill with blood. The beginning of filling is characterized by a continued decline in LV pressure caused by further relaxation of the LV. During this time, blood flow is driven by ventricular suction and the release of elastic energy stored in the stretched left atrium. This is commonly referred to as early filling or the E-wave. As LV volume increases, so does LV pressure, and blood flow to the LV begins to lessen as LA and LV pressures equalize. During the final portion of filling, the LA contracts, pumping an additional volume of blood into the LV. This is referred to as the A-wave and is normally smaller than the E-wave but can exceed the E-wave when early filling is impaired.

1.2.3 The Cardiac Cycle of the Right Heart

The right and left sides of the heart are isolated from each other by the pulmonary and systemic circuits. For this reason, they are often considered independently. They are however, functionally similar, having the same cardiac phases which occur in unison. A brief description of right heart function is provided here; however, the remainder of this thesis will focus on left heart function. The most significant difference lies in RV and pulmonary pressures. The RV pumps blood to the lungs, which have relatively low resistance to flow, in contrast to the LV which must pump blood to all other organs in the body, which have relatively high resistance. As a result, RV and pulmonary pressures are lower than LV and systemic pressures as shown in Figure 1.3 compared to Figure 1.2. The right ventricle is thinner walled than the left because of the lower forces necessary to drive pulmonary circulation.

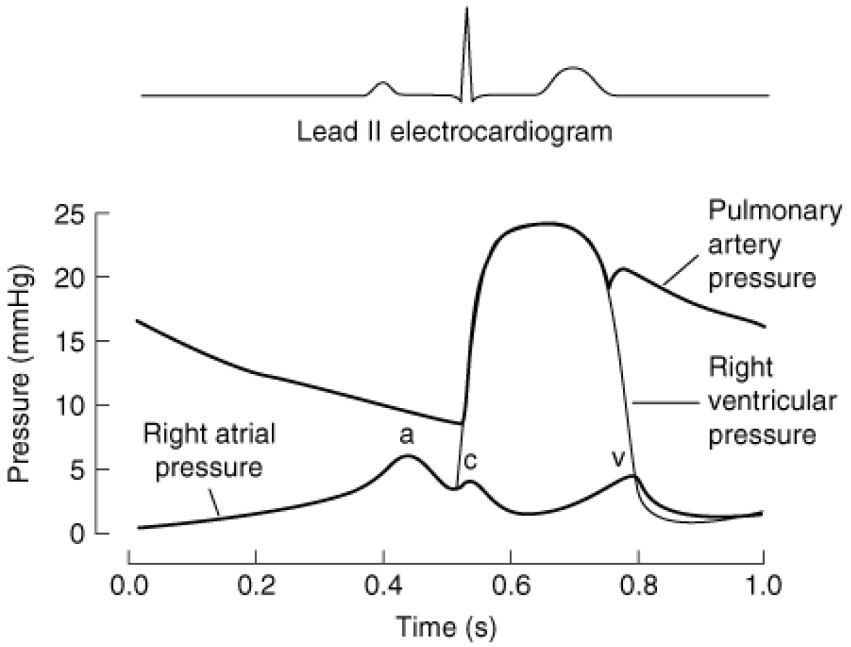

Figure 1.3: The cardiac cycle of the right heart. Figure from *Cardiovascular Physiology*, seventh edition [49].

1.3 Cardiac MRI

1.3.1 Basics of Cardiac MRI

The motion of the heart poses unique challenges for in vivo cardiac MRI. Images have to be acquired quickly with respect to the length of the cardiac cycle in order to obtain images free from temporal blurring. Additionally, it is often desirable to capture the entire cardiac cycle as a cine in order to visualize the time-course of cardiac motion. Respiratory motion is another important consideration since the heart rests against the lungs. In 1981, Hawkes et al. produced some of the first MRI images of the heart [50]. These images were acquired over 150 seconds, and while large features were easily recognized, detailed anatomy was not visible. Over the next 20 years, several important developments have resulted in vast improvements in image quality.

MRI images are acquired in the k-space domain. A plethora of im-

age acquisition strategies exist all with the same goal of generating a grid of k-space data. The Fourier transform of this data is an image. Conventionally, this grid of k-space is acquired one row at a time until all rows of data have been acquired. In 1977 Hinshaw et al. used this method to produce an image of the human wrist [51], and this continues to be the most common image acquisition scheme today. The time to acquire a single line of k-space is termed the repetition time (TR) and the time to acquire an entire image is the number of k-space lines multiplied by the TR. The number of k-space lines together with the field of view, determines the spatial resolution of the image, implying that higher spatial resolutions or larger fields of view require longer acquisitions. In the case of cardiac imaging, where fields of view are large because they must encompass the entire chest, the time to acquire a single image of sufficient spatial resolution is often too long to avoid temporal blurring, particularly during more dynamic periods of the cardiac cycle. A solution to this problem, was first introduced in the late 1970s as a solution for cardiac CT [52]. Electrocardiogram (ECG) gating was applied to acquire different parts of an image over multiple heartbeats, termed gated-segmented imaging. This was first applied for cardiac MRI in the early 1980s [53–55].

ECG gating uses electrodes placed on the surface of the skin to measure the electrical activity of the heart. A schematic of the characteristic pattern of electrical signals recorded is shown at the bottom of Figure 1.4. This pattern repeats with each heartbeat and allows for imaging to be synchronized with a specified phase of the cardiac cycle. "Segmented" refers to acquiring only a portion of the k-space data during each heartbeat. Acquiring only a portion of the data requires less time, and remaining portions are acquired in subsequent heartbeats. Thus a series of heartbeats must be observed to construct a complete image and an assumption that each heartbeat is identical is made.

To reduce respiratory motion, the acquisition can also be performed during a breath-hold.

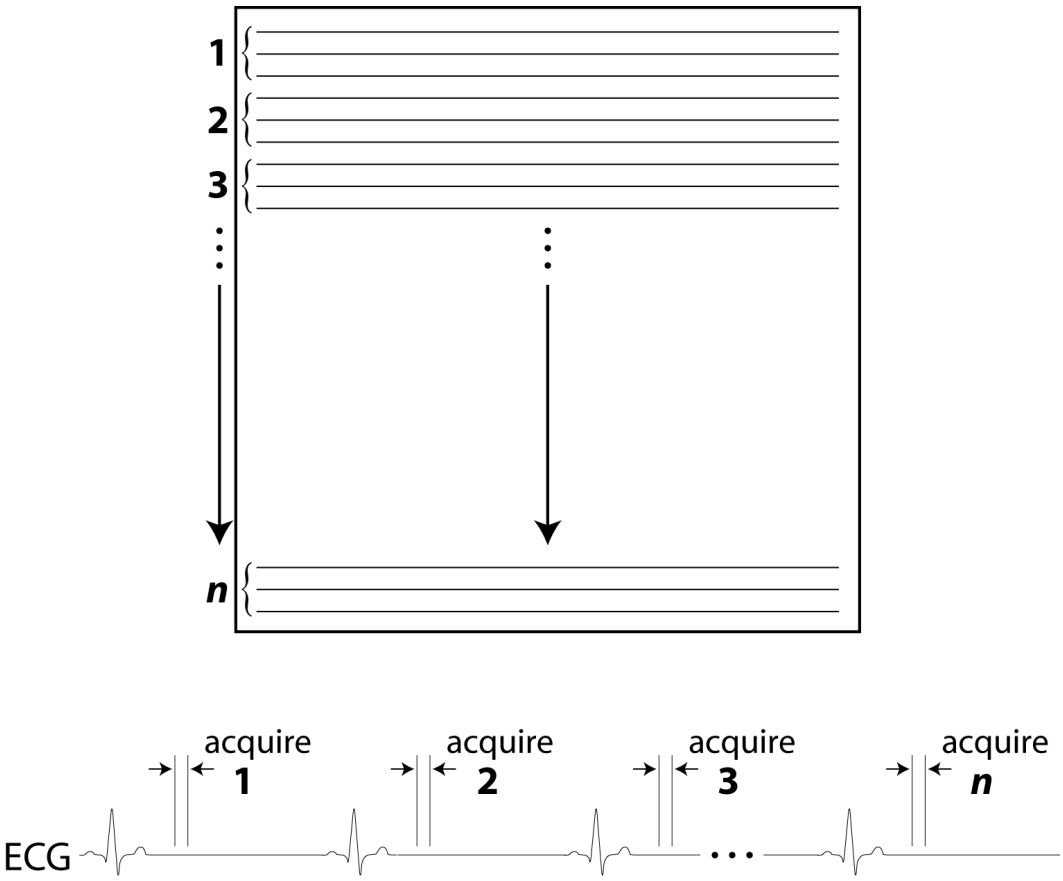

Figure 1.4: Gated-segmented imaging. An example is shown where 3 views per segment is acquired.

Typically, a specified number of k-space lines is acquired per heartbeat, referred to as views per segment (VPS). Figure 1.4 shows an example of an image acquired with 3 VPS over n heartbeats with a total number k-space lines, $N = 3n$ (= VPS $\times$ n). Thus, VPS $\times$ TR determines the length of the acquisition window, greatly reduced from the non-segmented version where the acquisition window would be $N \times (TR)$ (= VPS $\times$ n $\times$ TR). In practice, when determining the number VPS to use, the length of the acquisition window must be balanced with total acquisition time because shortening the acquisition window (reducing VPS) increases the total number of heartbeats

(n), which must not exceed the length of a comfortable breath-hold. Alternatively, assuming a fixed field of view, the acquisition window (VPS) can be traded off with spatial resolution determined by the total number of k-space lines (N) to maintain a comfortable total acquisition time (n).

Cine imaging must be employed to observe events as they occur throughout the cardiac cycle. To produce a cine, a time-series of images must be acquired and subsequently put together as a movie. In the example shown in Figure 1.4, data is only acquired during a very short portion of the cardiac cycle. Therefore, other portions of the cardiac cycle can be used to acquire additional images at other cardiac phases. Continuous data acquisition does not allow time for signal recovery and requires the use of steady-state imaging techniques. In 1986, Haase described one such steady-state imaging technique termed fast low-angle shot (FLASH) [56] which was applied to cardiac imaging a year later [57]. By 1991, the entire cardiac cycle could be imaged in a single breath-hold [58].

Cine acquisitions can be performed using prospective or retrospective gating. Prospective gating refers to imaging synchronized with the ECG signal. An example of a retrospectively gated cine is shown in Figure 1.5. Acquisition of a given segment is repeated for a time spanning at least one full heartbeat. Each repetition of the segment is then retrospectively assigned a cardiac phase with respect to the ECG signal. Images for each cardiac phase are then reconstructed by combining the appropriate repetition of each segment. Cines are commonly reconstructed to > 20 phases per cardiac cycle; however, the true temporal resolution is defined as VPS $\times$ TR. Both prospective and retrospective cine imaging are used throughout this thesis.

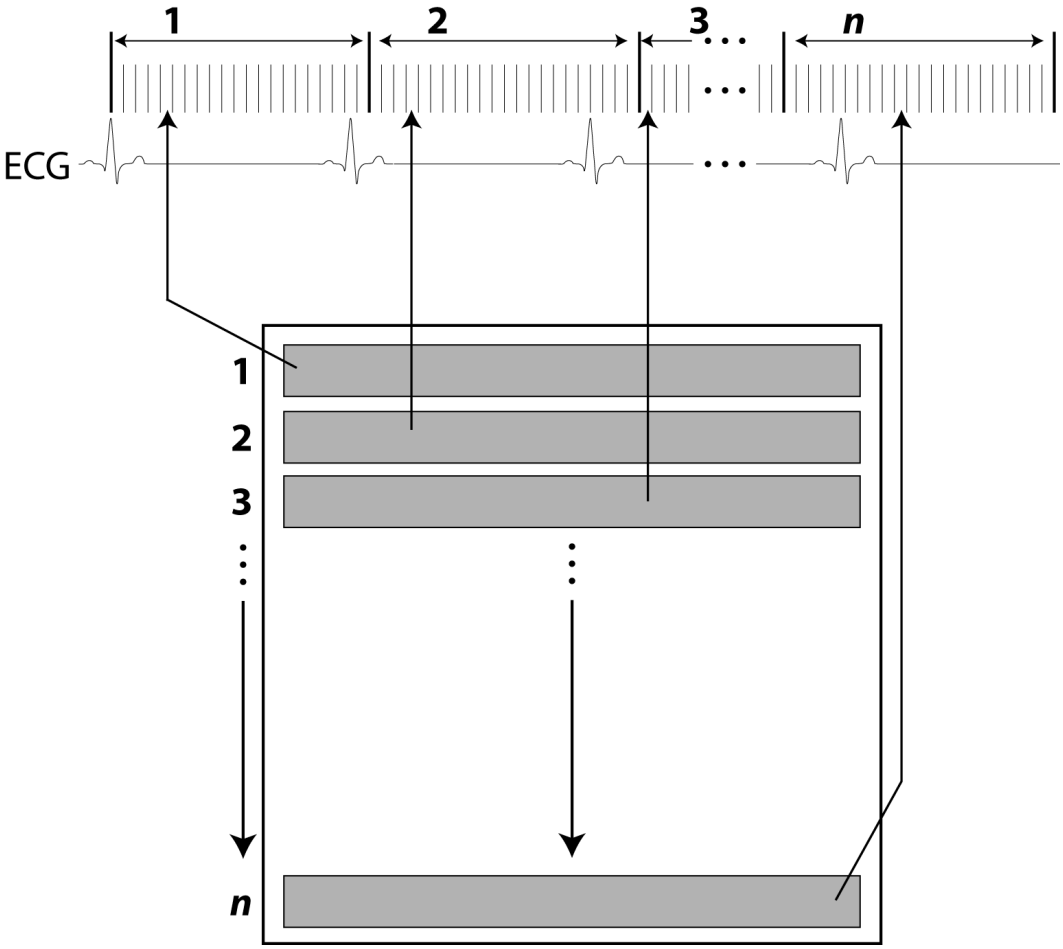

Figure 1.5: Cine imaging with retrospective reconstruction. The reconstruction of 1 image is shown. This procedure is repeated for all other images that compose the cine.

1.3.2 Imaging Morphology

Early cardiac MRI used spoiled gradient-recalled echo sequences (GRE or FLASH) to image heart morphology [56, 58]. A typical example of this sequence is shown in Figure 1.6. A low flip angle is applied at each TR and gradients are used to generate an echo. The transverse magnetization is spoiled at the end of each TR.

More recently, SSFP has replaced GRE as the bread and butter sequence for cardiac MRI. SSFP was first described by Carr in 1958 [59], and was later applied to imaging in 1986 [60]. SSFP imaging relies on all the mag-

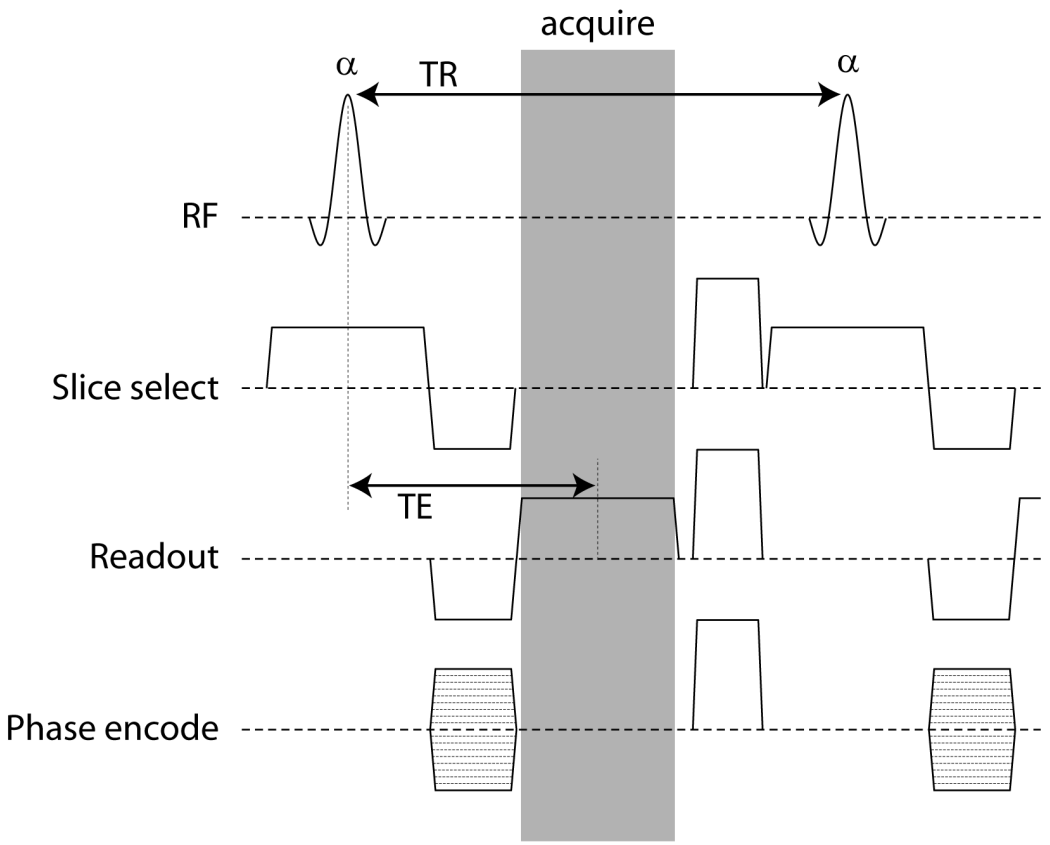

Figure 1.6: Spoiled gradient-recalled echo pulse sequence.

netization being refocused, as opposed to being spoiled, at the end of each TR and re-used for the next TR. Figure 1.7 shows a general example of an SSFP sequence and Figure 1.8 shows the specific implementation of this sequence by Siemens Healthcare (Erlangen, Germany). For this reason, magnetic field inhomogeneities are problematic for SSFP imaging and long TR times can result in an accumulation of errors and incomplete refocusing. As a result, SSFP did not gain widespread use in the cardiac field until the early 2000s following improvements in main magnetic field homogeneity and gradient switching speeds. Around this time, several papers demonstrated the superiority of SSFP over GRE techniques [61–64].

The SSFP pulse sequence offers 2 major advantages over spoiled GRE for cardiac applications. Since all of the signal is refocused and reused with

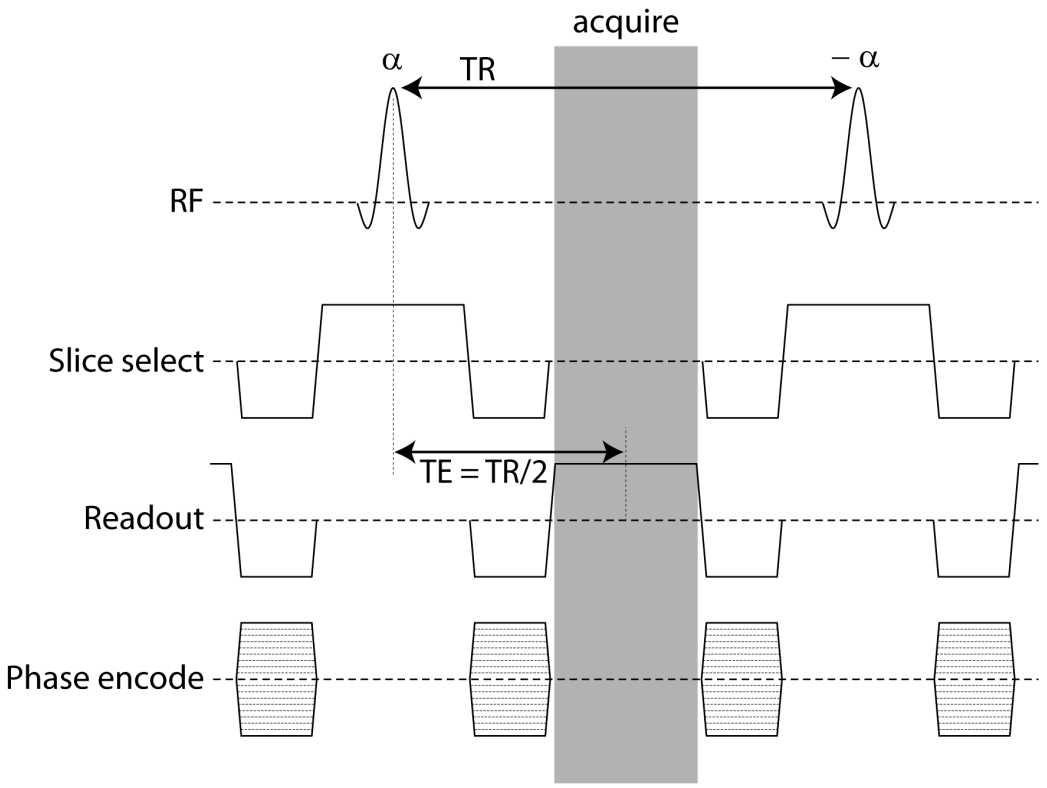

Figure 1.7: Steady-state free precession pulse sequence.

each TR, signal to noise (SNR) is not affected by faster imaging. This allows for improved temporal resolution, an important consideration for cardiac imaging. This is in contrast to spoiled gradient echo imaging, where a shortened TR reduces the time for T_1 recovery and thus the amount of signal available for imaging.

The second advantage is the superior contrast to noise (CNR) offered by SSFP. Spoiled GRE is T_1 weighted and does not offer good contrast between blood and myocardium which have similar T_1 values, approximately 1500 ms for blood and 1200 ms for myocardium at 1.5 T [65]. When applied to cardiac imaging, blood-myocardium contrast in these sequences relies mainly on inflow effects as opposed to inherent differences in T_1 relaxation properties. Blood flowing into the slice of interest has fully relaxed longitudinal magnetization resulting in a short effective T_1 compared to myocardium. This results in bright

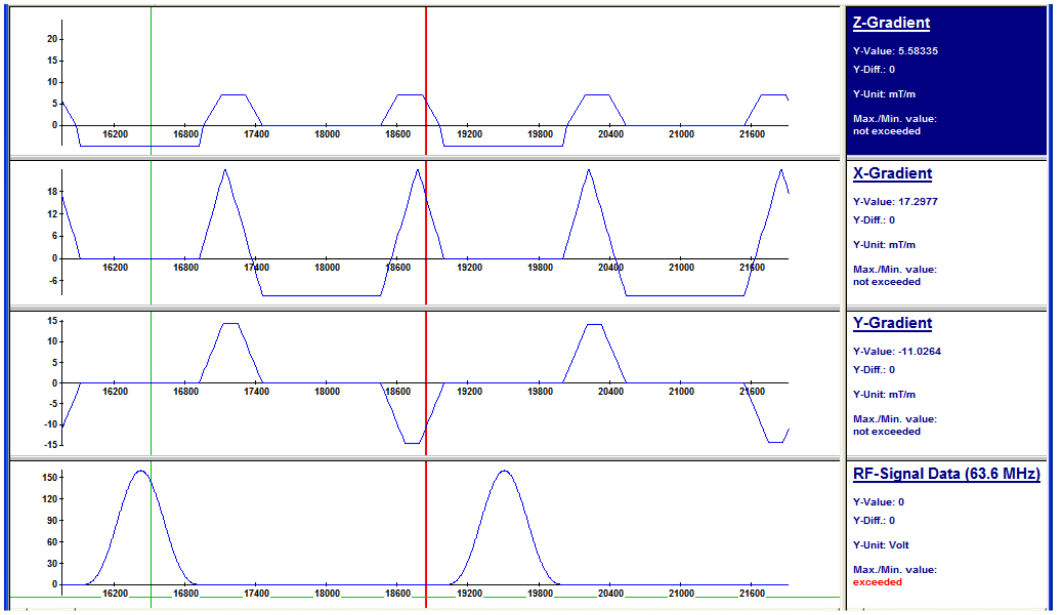

Figure 1.8: Siemens steady-state free precession pulse sequence.

blood and is refered to as inflow enhancement. This phenomenon however, depends on blood flow, which may be reduced in certain patient populations. It is also dependent on slice prescription, where slices parallel to the direction of blood flow and thicker slices will have less inflow enhancement. Shorter TR allows less time for fully relaxed spins to flow into the slice and also results in reduced inflow enhancement.

The SSFP signal on the other hand, is fully refocused prior to each RF pulse in contrast to the spoiled GRE signal. The magnetization spends time in both the longitudinal and transverse planes. As a result, the signal is dependent on both T_1 and T_2 and has T_2/T_1 contrast. This is advantageous for cardiac imaging because while blood and myocardium have similar T_1 values, the T_2 of blood (approximately 240 ms at 1.5 T [66]) is several times larger than the T_2 of myocardium (approximately 50 ms at 1.5 T [67]). Contrast to noise can thus be maintained even when blood flow is stagnant and acquisition parameters are unfavorable for inflow enhancement.

A typical cardiac MRI exam uses SSFP cine imaging to visualize my-

ocardial deformation and to measure heart chamber volumes and myocardial masses. The heart is typically imaged using a series of standard views. Long-axis views are similar to the orientation shown in Figure 1.1, where the apex and base are both visualized. Long-axis views include the 4-chamber, 2-chamber and 3-chamber. Short-axis views are oriented perpendicular to the long-axis views and offer visulization of the cross-section of the ventricles or atria. A series of parallel short-axis views that form a stack spanning the LV length or the length of the entire heart are commonly obtained. Examples of these standard views are shown in Figure 1.9.

1.3.3 Imaging Blood Flow

Blood velocity imaging using phase contrast MRI was described in 1984 by Bryant et al. and applied to measure blood flow in the carotid arteries and jugular veins as well as in the femoral arteries and veins [68]. In their paper, Bryant et al. described that in the presence of a bipolar, or otherwise balanced gradient (where the gradient area is zero), moving spins experience a phase shift with respect to stationary spins. In Figure 1.10, a typical phase contrast pulse sequence with flow encoding bipolar gradients and a GRE acquisition is shown. The specific implementation of this pulse sequence used throughout this thesis is shown in Figure 1.11.

The phase, ϕ, accumulated by spins in a magnetic field gradient is given by the following equation:

$$\phi = \gamma \int G(t)x(t)dt \tag{1.1}$$

where γ is the gyromagnetic ratio, $G(t)$ is the magnitude of the gradient as a function of time and $x(t)$ is the spatial location of the spins as a function

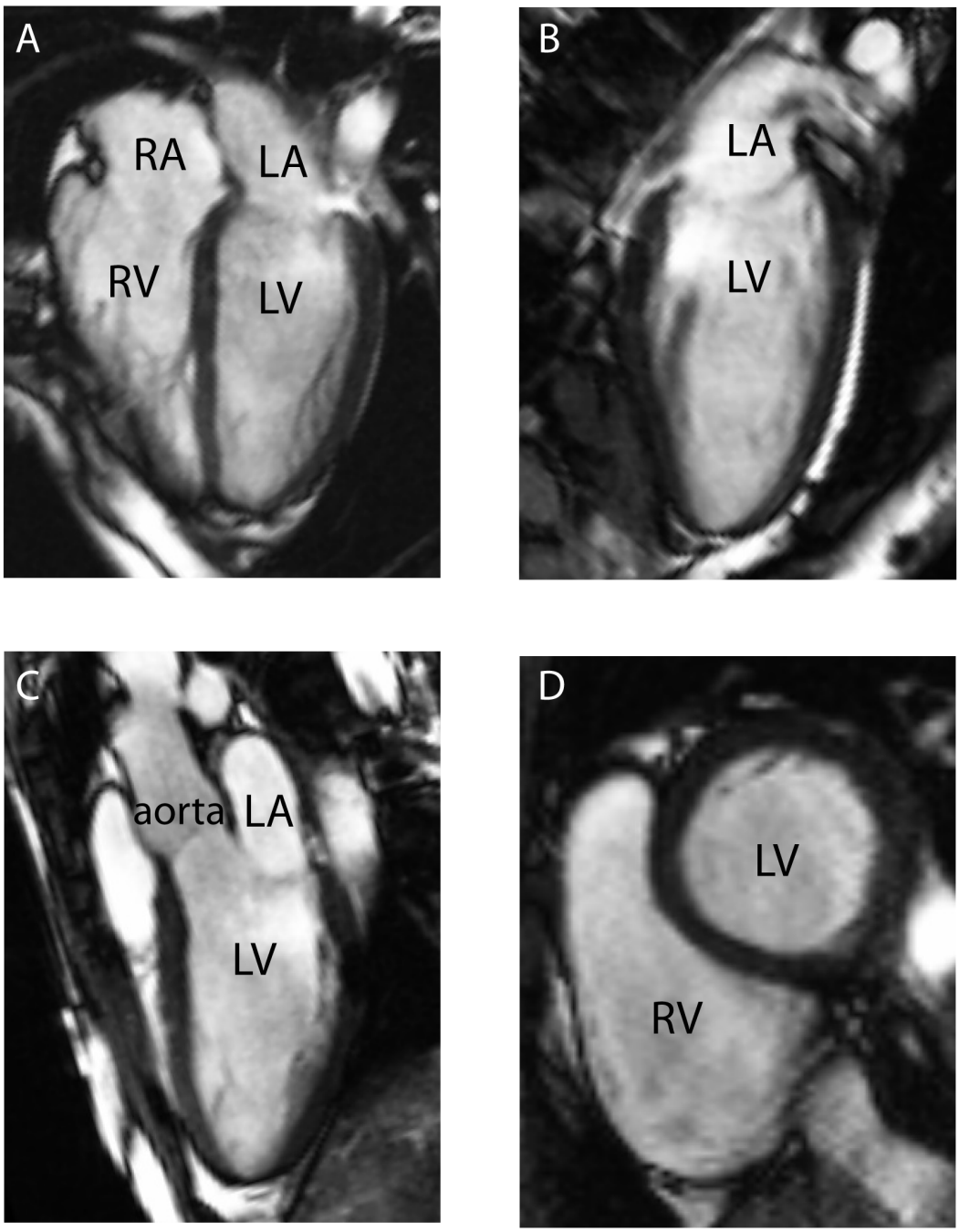

Figure 1.9: Standard views of the heart using SSFP imaging. Examples of (A) 4-chamber, (B) 2-chamber, (C) 3-chamber and (D) short axis views of the heart are shown.

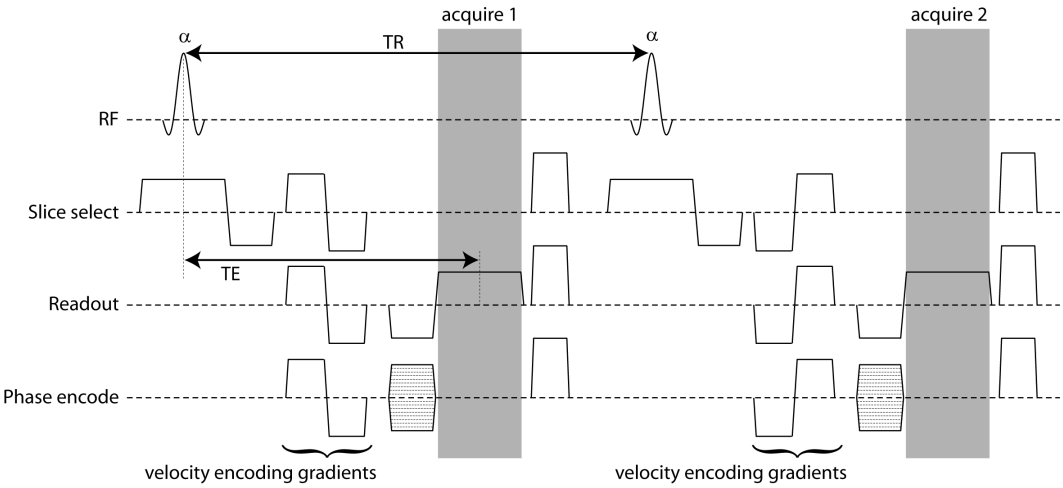

Figure 1.10: Phase contrast pulse sequence.

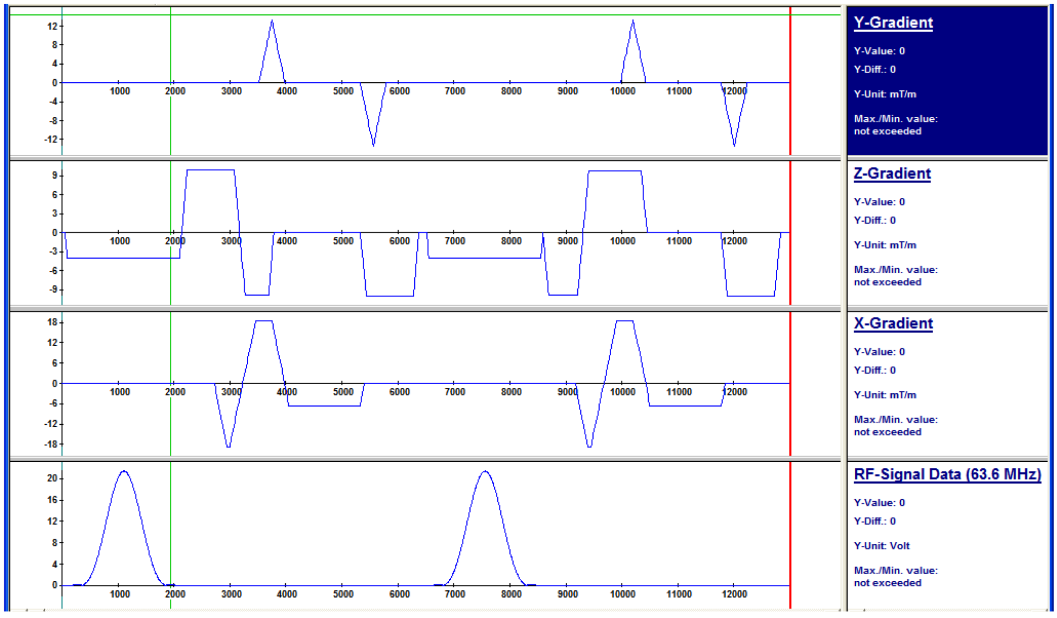

Figure 1.11: Siemens phase contrast pulse sequence.

of time. In the case of stationary spins, $x(t) = x_\circ$, and in the presence of balanced gradients, Equation 1.1 reduces to:

$$\phi = \gamma x_\circ \int G(t)dt = 0$$

However, for spins moving at a constant velocity, v, their position is defined as: $x(t) = x_\circ + vt$, and Equation 1.1 becomes:

$$\phi = \gamma x_\circ \int G(t)dt + \gamma v \int G(t)t\, dt$$

The first half of this equation reduces to 0 in the case of balanced gradients but the second half remains non-zero. For a bipolar gradient with a positive lobe followed by a negative lobe:

$$\phi = \gamma v \left[\int_0^{T_b} G_b t dt + \int_{T_b}^{2T_b} -G_b t dt \right]$$

$$\phi = \gamma v \left[\frac{1}{2}t^2 \Big|_0^{T_b} - \frac{1}{2}t^2 \Big|_{T_b}^{2T_b} \right]$$

$$\phi = \gamma v \left[\frac{1}{2}{T_b}^2 - 0 - 2{T_b}^2 + \frac{1}{2}{T_b}^2 \right]$$

$$\phi = -\gamma G_b {T_b}^2 v \tag{1.2}$$

where G_b is the gradient amplitude and T_b is the time-duration of one of the lobes. This relationship is useful because the resulting phase is directly proportional to velocity. Similarly, for a bipolar gradient with a negative lobe followed by a positive lobe:

$$\phi = \gamma G_b {T_b}^2 v \tag{1.3}$$

In practice however, this simple relationship is confounded by background phase effects caused by magnetic field inhomogeneities and the phases

of individual coils. The solution to this problem is to acquire 2 images with different flow encoding strengths but with the same background phase. Subtraction of these 2 images then removes the background phase but not the velocity dependent phase. This subtraction is peformed by multiplying one phase encode step by the complex conjugate of the other and the signal from all coils are then averaged in the complex domain before taking the phase. This proceedure avoids problems associated with phase wrapping and weighs the phase from each coil by its magnitude (coil sensitivity). As shown in Figure 1.10, the 2 images are interleaved to minimize time-varying background phase discrepancies. Opposite bipolar gradients yield the maximum signal to noise and the phase is related to velocity as: $\phi = 2\gamma G_b {T_b}^2 v$ (from Equations 1.2 and 1.3). Flow encoding can be performed in any direction specified by the net gradient from slice select, readout and phase encode channels.

In practice, blood velocity versus time curves are often extracted from phase contrast velocity images. Figure 1.12 shows an example of velocity-time curves measured close to the mitral and aortic valves. Through-plane velocity images acquired using phase contrast for a short axis slice are shown in Figure 1.12C and D, positioned as shown in panel A on a 3-chamber view. The position of the measurement locations within the slice corresponding to the extracted velocity-time curves are also shown. Using this method, aortic blood velocity during ejection and mitral blood velocity during diastole can be measured.

1.3.4 Imaging Tissue Deformation

Tissue tagging was introduced in 1989 by Axel and Dougherty using the spatial modulation of magnetization (SPAMM) sequence [39]. SPAMM is a magnetization preparation technique that modulates the longitudinal mag-

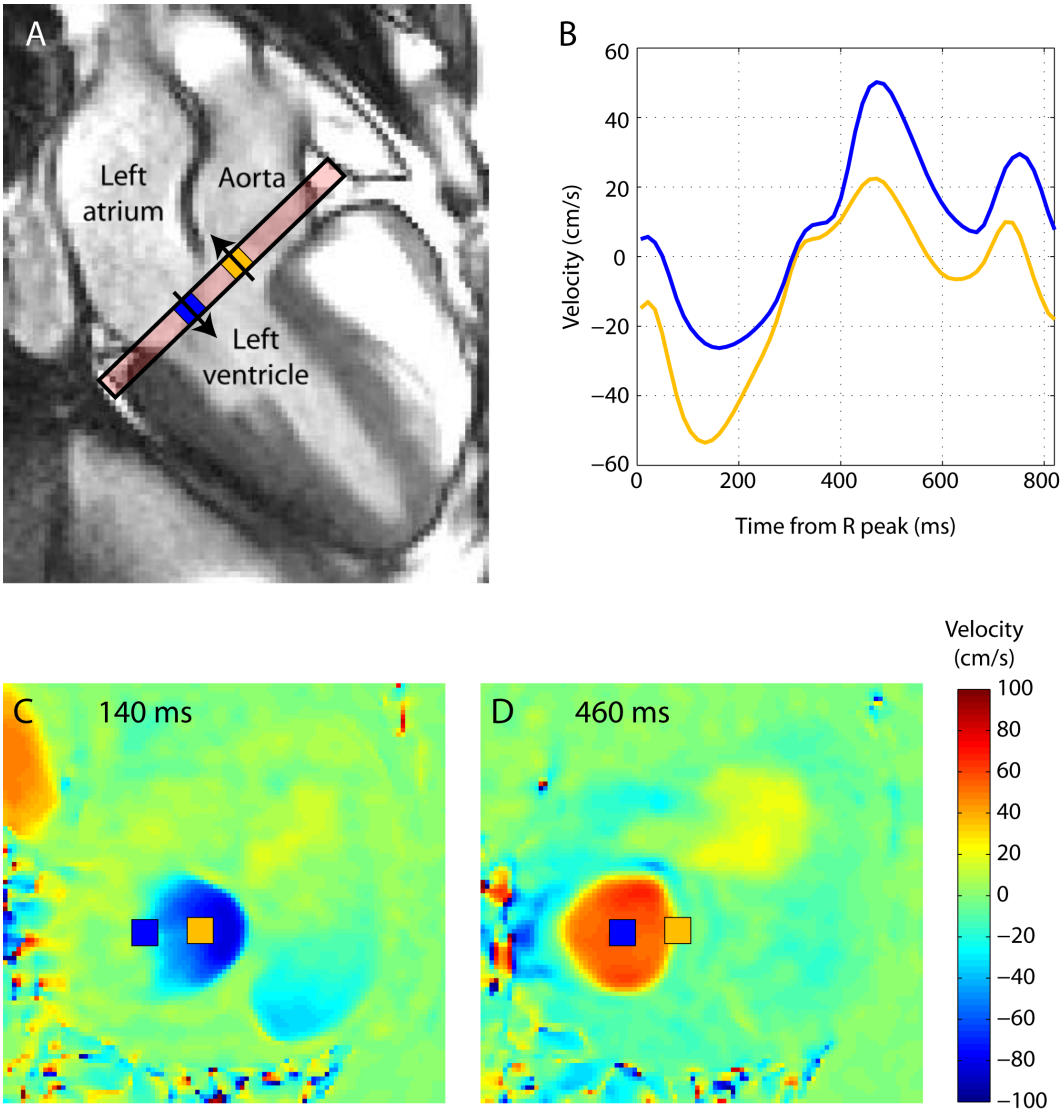

Figure 1.12: Example inflow and outflow velocity curves. Velocity is measured using phase contrast MRI in a short-axis slice orientation with its position shown on a 3 chamber view (A). Resulting velocity-time curves for measurement locations of interest are shown (B). Phase contrast velocity images from which velocity values are extracted are also shown for systolic (C) and diastolic (D) cardiac phases.

netization in a spatially varying pattern. An example of an image acquired with tissue tagging is shown in Figure 1.13.

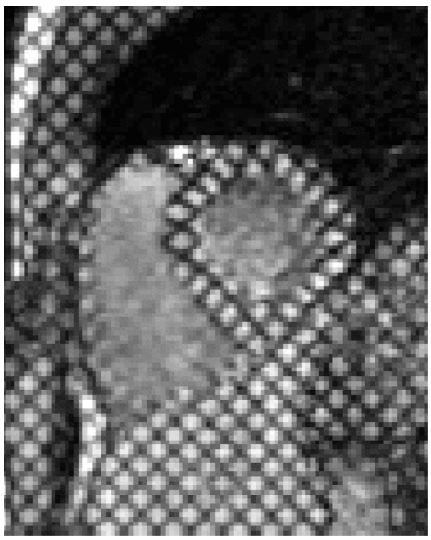

Figure 1.13: A short axis image with tissue tagging.

To generate the magnetization modulation, 4 steps are required as shown in Figure 1.14. First a radiofrequency pulse, α, is applied to tip the magnetization into the transverse plane. Next, a gradient is applied in the readout or phase encode direction, determining the orientation of applied tags. This causes the spins to accumulate phase proportional to their position in space and is represented in Figure 1.14 as a cone. From Equation 1.1, the phase accumulated as a function of space, x, following the modulation gradient is:

$$\phi = xG_mT_m \tag{1.4}$$

where G_m is the magnitude of the modulation gradient and T_m is the time duration of the gradient. For illustrative purposes, 2 magnetization vectors are singled out, $\vec{v_1}$, which experiences $2\pi n$ phase accumulation and $\vec{v_2}$, which experiences $\pi + 2\pi n$ phase accumulation, where n is any integer value. These 2 vectors are shown in Figure 1.14. From Equation 1.4, the magne-

tization resembles $\vec{v_1}$ at $x = \frac{2\pi}{G_m T_m} n$, and the magnetization resembles $\vec{v_2}$ at $x = \frac{\pi}{G_m T_m} + \frac{2\pi}{G_m T_m} n$. Another α pulse is then applied to tip the cone further, tipping $\vec{v_1}$ onto the longitudinal axis and $\vec{v_2}$ 2α from the longitudinal axis. Finally, a spoiler gradient is applied to dephase the magnetization in the transverse plane, leaving $\vec{v_1}$ unaffected and reducing $\vec{v_2}$ to $\vec{v_1} cos(2\alpha)$. Spatially, this corresponds to $x = \frac{2\pi}{G_m T_m} n$ being lines of maximal signal intensities ($\vec{v_1}$) and $x = \frac{\pi}{G_m T_m} + \frac{2\pi}{G_m T_m} n$ being lines of minimum signal intensity ($\vec{v_2}$). The spacing betweens lines is $\frac{2\pi}{G_m T_m}$ and is thus finer for a larger magnitude and duration of the modulation gradient. The magnetization preparation can be applied twice in perpendicular directions to produce a grid.

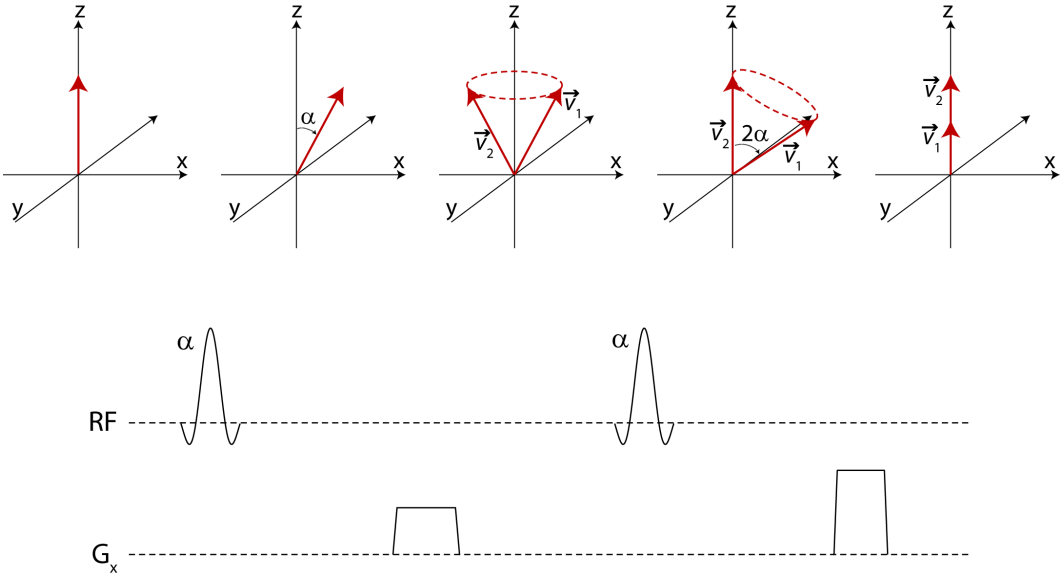

Figure 1.14: Tissue tagging pulse sequence (SPAMM) and magnetization vector diagram. Adapted from Axel and Dougherty [39].

The pulse sequence described above is the simplest application of the SPAMM technique and is referred to as 1-1 SPAMM describing the ratio of the 2 α pulses applied. In this case, the magnetization follows a sinusoidal pattern over space. Other variations use additional radiofrequency pulses in a binomial pattern (1-2-1, 1-3-3-1, 1-4-6-4-1, etc.) to create a more rectangular pattern of magnetization and thus sharpen the tags. In this thesis, 1-3-3-1 SPAMM

is used, where the numbers describe the ratio of applied flip angles and a modulation gradient is applied between each radiofrequency pulse. In cardiac applications, tags are applied at a specified point in the cardiac cycle, typically end-systole, then imaged throughout the remainder of the cardiac cycle as a cine. The deformation of the tissue can then be observed by tracking the motion of the tags. An example of an implementation of a tagging sequence is shown in Figure 1.15.

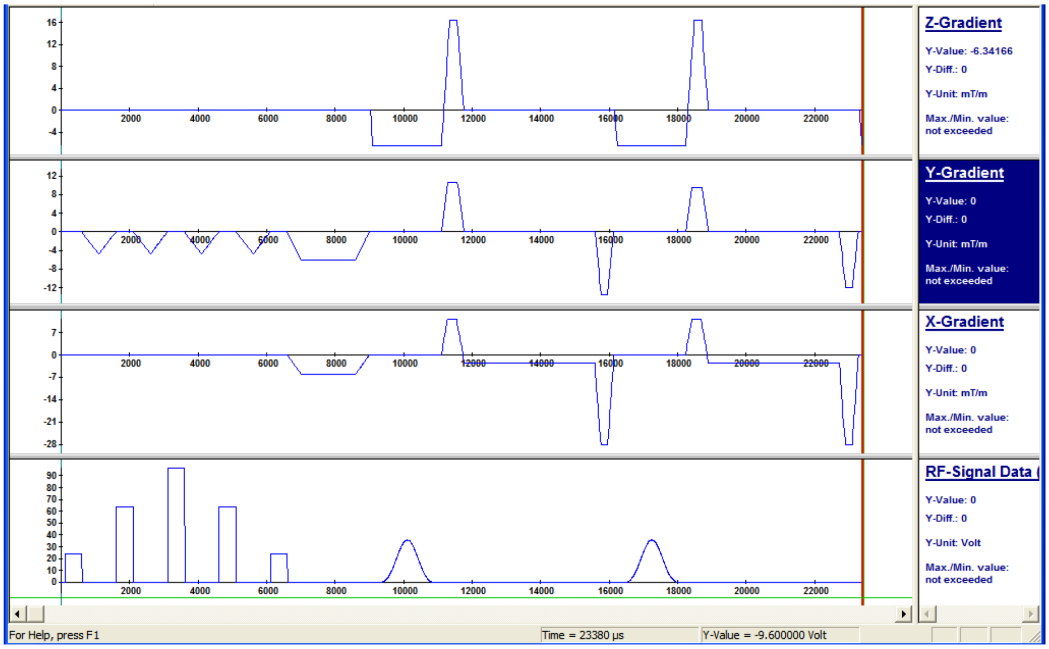

Figure 1.15: Siemens tissue tagging pulse sequence (SPAMM).

1.4 Evaluation of Diastolic Function

1.4.1 Normal Diastolic Function

Diastole refers to the portion of the cardiac cycle when the ventricles are relaxing and filling with blood. Some of the mechanisms that govern diastole are active relaxation [24, 69], elastic recoil [27, 70, 71] and passive stiffness of the LV [24]. Active relaxation refers to the energy consuming process by

which tension in the muscle fibers is released while elastic recoil describes the tendency of the ventricle to return to its natural shape. Passive stiffness refers to the properties of the fully relaxed myocardium. Diastolic dysfunction can refer to any abnormality in these mechanisms, including delayed, slowed or incomplete relaxation, poor systolic function which reduces elastic recoil and increased LV stiffness. Diastolic dysfunction also encompasses impaired atrial function, which provides diastolic preload and supplies additional filling through atrial contraction [29]. Diastolic dysfunction can occur irrespective of normal or abnormal systolic function and may or may not present with symptoms [14].

During the time-course of diastole, the relative importance of the various mechanisms of diastolic function varies. During isovolumic relaxation, active relaxation and elastic recoil determine myocardial deformation. The microscopic lengthening of muscle fibers manifests macroscopically as untwisting of the chamber [72]. The subendocardium consists of right-handed helical fibers while the subepicardium consists of left-handed helical fibers with helical direction changing smoothly from endocardium to epicardium. Right-handed helical fibers encourage clockwise apical and counter-clockwise basal rotation when viewed from apex to base while left-handed helical fibers encourage counter-clockwise apical (clockwise basal) rotation. Opposing directions of rotation between base and apex produce a twisting or wringing motion. During systole, all fibers contract together but the larger radius of subepicardial fibers generates more torque and counter-clockwise apical (clockwise basal) rotation dominates. LV twist has been described as a mechanism of energy storage during ejection which is released when the ventricle untwists as ventricular recoil during the following IVR interval [27, 70, 71]. Because the volume of the LV must remain constant as dictated by closed mitral and aortic

valves, untwisting of the ventricle provides a mechanism for the lengthening of muscle fibers independent of volume changes. Untwisting is largely complete by mitral valve opening [26, 70, 73–75], but relaxation of the LV continues into the early filling portion of the cardiac cycle [24].

Ventricular filling is driven by a pressure difference between the LA and LV, but can be further characterized by the individual contributions to filling provided by each chamber, i.e., ventricular suction versus atrial push [76]. Atrial push is determined by the pressure within the stretched left atrium while ventricular suction is determined by LV relaxation and recoil. During early filling, ventricular suction has been demonstrated in canine models by occlusion of the mitral annulus and the measurement of sub-atmospheric LV pressure during the resulting non-filling beats [76, 77]. Early filling ends when atrio-ventricular pressure differences equalize, referred to as diastasis. During diastasis, the ventricle and atrium are fully relaxed and their volumes are dictated by the geometry and passive properties of the chambers. Diastole ends with atrial contraction, which contributes an additional 20%–30% to the total LV filling volume [29].

Most literature focuses on impaired diastolic function in the context of impaired LV function; however, the left atrium also plays an important role in modulating diastolic function. Left atrial function is often divided into reservoir, conduit and booster pump functions [29, 78]. Reservoir function refers to the role of the LA in collecting venous return from the lungs during ventricular systole and subsequent emptying during early filling and is represented by LA volume changes. LA reservoir function starts with a rapid filling phase analogous to early filling in the LV [79]. LA relaxation causes a decrease in LA pressure which allows for blood flow from the pulmonary circulation to pool in the left atrial chamber. This is further promoted by the descent of the

LV base due to ventricular contraction and is modulated later in the reservoir stage by LA chamber stiffness. The conduit function refers to blood flow from pulmonary veins to the LV during early filling and diastasis with no associated change in LA volume and is estimated to account for approximately 35% of blood flow through the atrium [80]. The booster pump function refers to blood flow due to atrial contraction.

Critical to proper diastolic function is the maintenance of low filling pressures. During diastole, the ventricle, atrium, pulmonary veins and lungs form one connected chamber. Elevated LV pressures thus transfer to elevated pulmonary pressures, and if severe enough, can result in the classic symptoms of heart failure such as shortness of breath and pulmonary edema [14]. Normal diastolic function occurs at low filling pressures (< 12 mmHg) achieved using a combination of mechanisms. During systole, left atrial relaxation and compliance are important for maintaining low pressures while accepting pulmonary venous return. In order to maintain low pressures during ventricular filling, LV elastic recoil and ventricular suction draw blood into the LV, allowing LA and pulmonary venous pressures to remain low. Following LV relaxation, LV compliance allows for continued filling towards the end of early filling. It also allows for additional filling with minimal increases in pressure during atrial contraction. A disruption in any of these mechanisms ultimately results in increased filling pressures. For diastolic function to be truly normal, these conditions must be maintained during rest and during exercise.

1.4.2 Invasive Evaluation of Diastolic Function

Left Ventricular Relaxation

Gold standard measures of diastolic function are the characteristic time constant of isovolumic LV pressure decline (τ) and the passive stiffness of the LV. These parameters require invasive catherization to measure LV pressures. Figure 1.16 shows an example of diastolic pressure within the LV (see Figure 1.2 for more context). During IVR, the decline in LV pressure has been shown to be an exponential decay, characterized by the time constant τ and described by the following equation [24, 69]:

$$P(t) = P_{\circ} e^{-t/\tau} \tag{1.5}$$

where P is LV pressure, $P_{\circ}$ is LV pressure at AVC and t is time following AVC. Impaired relaxation, described as the slowed time-course of relaxation, is characterized by an increase in τ. This is shown in Figure 1.16, plotted in red ($\tau = 60$ ms), compared to a normal value of τ, plotted in black ($\tau = 35$ ms). Values of τ plotted represent values measured by Zile et al. in patients meeting diagnostic criteria for diastolic heart failure and controls with no cardiovascular disease [24].

Left Ventricular Stiffness

Left ventricular stiffness is a measure of the mechanical properties of the fully relaxed myocardium and is measured in the latter half of diastole. This is in contrast to τ which is measured early in diastole. The fully relaxed ventricle can normally accommodate large changes in volume with only minimal accompanying changes in pressure in the normal physiologic range [23].

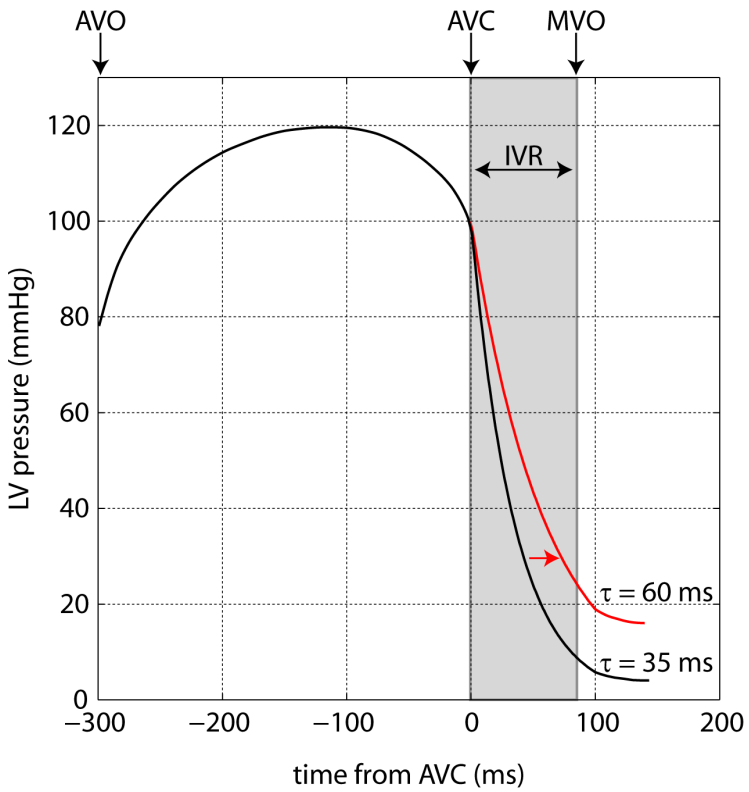

Figure 1.16: Time-course of left ventricular pressure. Normal LV function is shown in black and impaired relaxation in red.

As volume continues to increase however, pressure begins to more rapidly increase. This relationship is shown in Figure 1.17. Stiffness is defined as:

$$\text{stiffness} = \frac{\Delta P}{\Delta V} = \frac{dP}{dV} \tag{1.6}$$

where P is LV pressure and V is LV volume. Stiffness can thus be measured from the slope of the pressure-volume curve. In vivo, a measure of end diastolic stiffness can be obtained by simultaneously measuring pressure and volume during the latter portion of diastole when the LV is assumed to be fully relaxed.

Also shown in Figure 1.17 is an example of the characteristic end diastolic pressure volume relationship of patients with diastolic heart failure [22]. The curve for these patients is shifted upwards, meaning that they are operating at higher pressures for similar volumes and indicate a change in intrinsic

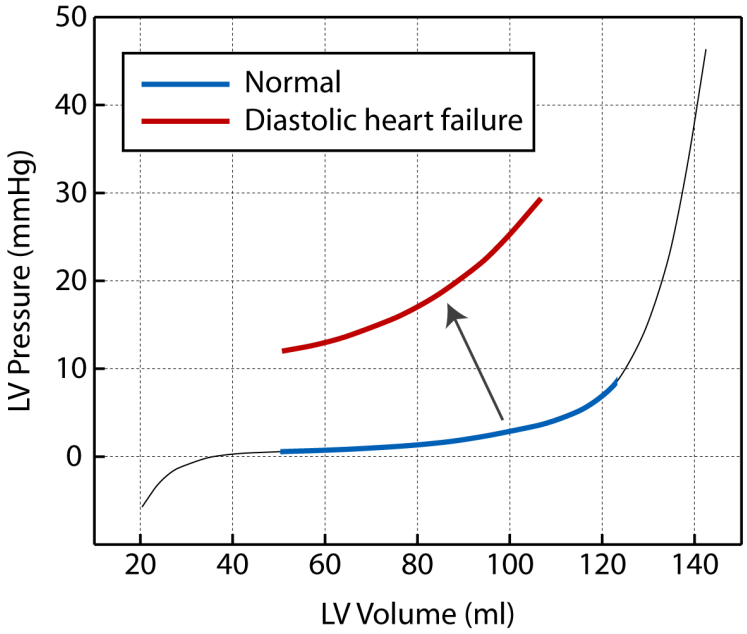

Figure 1.17: Passive left ventricular pressure-volume relationship. The curve for a normal left ventricle is shown in black. The normal operational range of values is shown in blue and the operational range for subjects with diastolic heart failure is shown in red. Figure adapted from Burkhoff et al. [23] and Aurigemma et al. [22]

myocardial properties. The slope of the curve is also steeper, which represents increased stiffness. Increased stiffness can also occur for hearts with normal pressure volume relationships if they are operating at increased volumes.

Left Atrial Function

Left atrial function can be described using relaxation and stiffness values similar to invasive LV diastolic parameters. LA relaxation can be measured from the decline in the time-course of pressure following atrial contraction and stiffness can be measured from the subsequent pressure-volume relationship during late ventricular systole [29, 79]. However, unlike the LV, the LA is not isolated from "upstream" pressures during its relaxation phase. Thus, parameters of LA relaxation are dependent on pulmonary venous pressure.

1.4.3 Non-Invasive Evaluation of Diastolic Function

Non-invasive evaluation of diastolic function using imaging techniques is far more common in research applications than the gold standard invasive techniques and is used exclusively in the clinic. Standard evaluation consists of a number of blood and tissue velocities measured using Doppler echocardiography in combination with LV and LA chamber volumes and LV mass [3]. Other more exploratory measures apply tissue tracking methods such as speckle tracking echocardiography or tissue tagging MRI to measure ventricular untwisting and strain [26–28, 70, 72].

Chamber Volumes and Mass

Remodeling of the LV can occur as hypertrophy, an increase in LV mass, or as an increase in LV volume, or both together [81]. Impaired diastolic function can exist in hearts with normal mass and volume; however, it is almost always present in hearts that have remodeled [3], with the exception of physiologic remodeling [81], making chamber volumes and mass an important indicator of diastolic dysfunction. (Physiologic remodeling is characterized by increases in LV volume and mass with normal relative wall thickness as observed in athletes.) MRI is the gold standard for measurements of chamber volume and mass [82, 83], following which, 3D echocardiography has been shown to be superior to 2D echocardiography [84, 85]. Normal values are shown in Table 1.1. Notice that MRI yields larger values for volume and smaller values for mass than echocardiography.

Left atrial remodeling has also been shown to be an important indicator of diastolic dysfunction. In response to abnormal ventricular diastolic function, left atrial pressures increase to maintain filling. Chronic increases

Table 1.1: Reference values for normal LV volume, LA volume and LV mass

	Echo		MRI	
	Male	Female	Male	Female
LA ESV, ml	18–58	22–52	48–107	42–95
LA ESV indexed, ml/m^2	22 ± 6	22 ± 6	26–53	27–52
LV EDV, ml	67–155	56–104	102–218	83–187
LV EDV indexed, ml/m^2	35–75	35–75	56–108	54–102
LV mass, g	96–200	66–150	81–165	42–150
LV mass, indexed, g/m^2	50–102	44–88	45–81	31–79

ESV = end-systolic volume; EDV = end-diastolic volume. MRI reference values are from Hudsmith et al. for LV volume and mass [86] and Maceira et al. for LA volume [87]. All echocardiography reference values are from Lang et al. [2].

in left atrial pressure cause stretching of the left atrial myocardium [88]. Left atrial enlargement becomes more severe with increasing severity of diastolic dysfunction. Thus, LA size gives an indication of chronicity and severity of diastolic dysfunction. LA volume has also been shown to be predictive of atrial fibrillation, ischemic stroke, heart failure and death [88].

Patterns of Mitral Inflow Velocity

Doppler echocardiography uses the frequency shift experienced by reflected ultrasound waves off of non-stationary objects and is the workhorse of echocardiographic measures of diastolic function. During the 1980s and into the early 1990s, a series of studies examining diastolic blood velocity at the mitral valve began to show characteristic patterns associated with diastolic dysfunction [25, 89–92]. The same patterns were present and consistent in showing worsening diastolic function over a wide range of cardiovascular conditions and also with aging. A study in 1988 by Appleton et al. measured both echocardiographic and invasive measures of diastolic dysfunction,

providing the link between these parameters [25].

Mitral inflow velocity is determined by the trans-mitral pressure gradient. Time-courses of velocity are measured at the mitral valve leaflet tips and are generally classified as normal, impaired relaxation, pseudonormal or restrictive (Figure 1.18) [3, 14, 25, 93]. Pressure decline in the LV during early filling causes a negative trans-mitral pressure gradient resulting in forward blood flow (the E-wave). Atrial contraction at the end of diastole causes an increase in atrial pressure and additional forward blood flow (the A-wave). This pattern is characterized most commonly by 3 diastolic parameters: the E/A ratio, the deceleration time (DT) and the isovolumic relaxation time (IVRT). The E/A ratio and DT are calculated from velocity at the mitral leaflet tips, where E/A is the ratio of peak velocities and DT is the time-duration of the E-wave downslope. IVRT is obtained by placing the sample volume closer to the LV outflow tract to simultaneously measure systolic outflow and diastolic inflow velocity; the interval of no flow is considered IVRT. Guidelines for normal and abnormal values are shown in Table 1.2. Other parameters described below are also included in this table.

Table 1.2: Normal and abnormal Doppler echocardiographic measures of diastolic function

	Normal				
	Young	Adult	Impaired relaxation	Pseudonormal	Restrictive
E/A	> 1	> 1	< 1	1–2	> 2
DT, ms	< 220	< 220	> 220	150–200	< 150
IVRT, ms	< 100	< 100	> 100	60–100	< 60
S/D	< 1	≥ 1	≥ 1	< 1	< 1
Ar, cm/s	< 35	< 35	< 35	≥ 35	≤ 25
V_p, cm/s	> 55	> 45	< 45	< 45	< 45
E', cm/s	> 10	> 8	< 8	< 8	< 8

Values are from Garcia et al. [93].

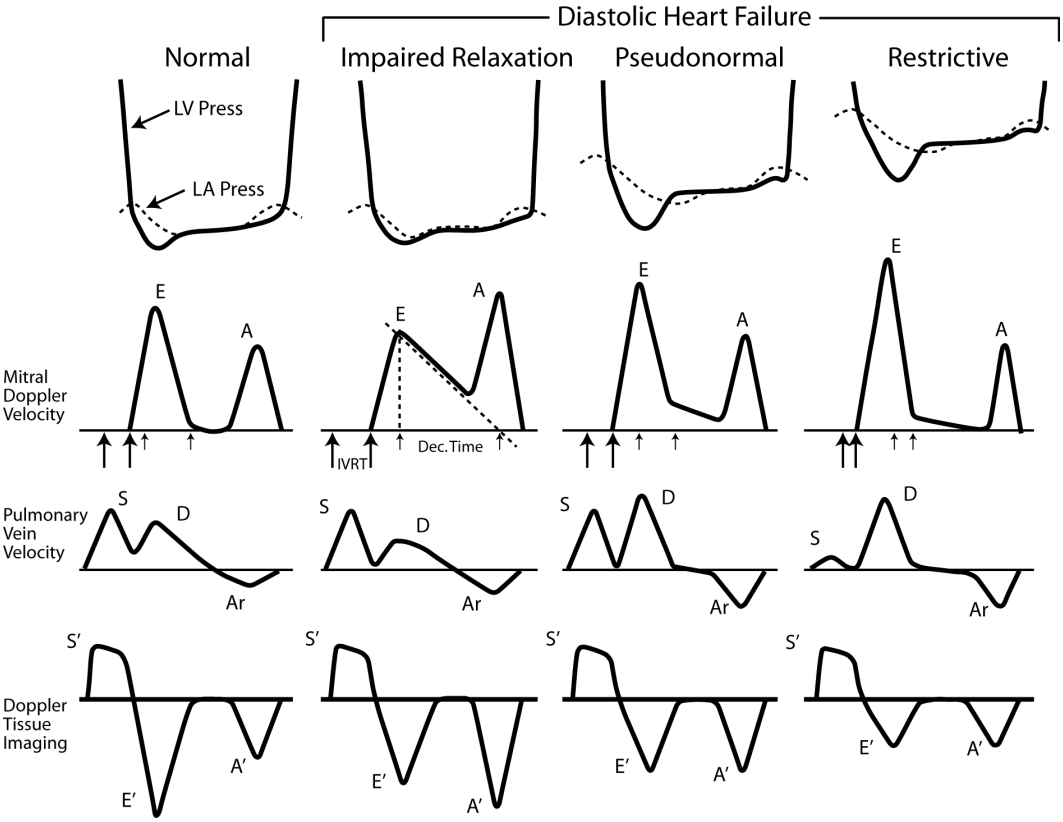

Figure 1.18: Characteristic pressures, blood velocities and tissue velocities in normal and abnormal diastolic function. Figure adapted from Zile et al. [14].

The first stage of diastolic dysfunction is termed impaired relaxation and refers to slowed ventricular relaxation, as characterized by the time-constant τ, without accompanying increases in LA pressure. Because the mitral valve opens only when LV pressure falls below LA pressure, impaired relaxation results in delayed MVO and a longer IVRT. DT is also lengthened because relaxation extends into early filling. The E-wave is depressed and atrial contraction is augmented to maintain filling, resulting in $E/A < 1$.

The next stage of diastolic dysfunction occurs when abnormal ventricular relaxation and increased stiffness result in increased left atrial pressure. During this stage, inflow patterns appear normal as slowed relaxation is compensated for by increased atrial pressure which normalizes the trans-mitral pressure gradient. Increased LA pressure results in earlier mitral valve open-

ing and shorter IVRT despite slowed relaxation, and the E-wave normalizes as a result of increased atrial push despite reduced ventricular suction. As a result, the contribution to stroke volume is shifted back to the E-wave and the A-wave is reduced.

Restrictive filling is associated with a marked increase in ventricular stiffness and increased LA pressure. IVRT is further shortened due to high LA pressures. DT is also shortened as a result of the stiff left ventricle causing a rapid rise in LV pressure during early filling and preventing further filling. High LV pressure during the subsequent atrial contraction resists further filling blood flow and the A-wave becomes small.

Patterns of Pulmonary Venous Velocity

Shortly after mitral inflow velocity was described in the 1980s, pulmonary venous velocities were also described [94]. Using Doppler echocardiography, pulmonary venous velocity, is measured in the left upper pulmonary vein and is used to compliment mitral inflow recordings [3]. Normal and abnormal patterns of pulmonary vein velocity are shown in Figure 1.18. During ventricular systole, blood flow into the LA is represented by the S-wave. The S-wave is modulated by left atrial relaxation, the descent of the LV base during ejection and end-diastolic LA pressure. Young subjects and athletes tend to have small atrial contraction (high E/A ratio) and an associated small atrial relaxation and S-wave. With aging, the A-wave increases and so does the subsequent S-wave [93]. The D-wave represents blood flow into the LA during early filling and tends to mirror the E-wave. Retrograde flow during the A-wave, Ar, is caused by atrial contraction, which pushes blood back into the pulmonary veins. The most commonly reported parameters are the S/D ratio and the peak Ar velocity. Normal values are $S/D = 0.34$–1.62 and $Ar = 5$–37

cm/s (95% confidence intervals for individuals aged 21–60) [3].

During impaired relaxation, the D-wave is depressed and Ar increases, reflecting a lowered E-wave and increased atrial contraction. Greater atrial contraction also increases atrial relaxation and the S-wave. As a result, S/D and Ar are both increased. For pseudonormalized hearts, the D-wave normalizes, again mirroring a normalized E-wave. The S-wave is reduced along with atrial contraction, resulting in a normal S/D ratio. However, Ar increases further due to elevated end-diastolic pressure and increased ventricular stiffness. As the atrium contracts against a stiff ventricle, there is increased retrograde flow as opposed to forward flow. Increased Ar can thus distinguish pseudonormalization from truly normal diastolic function. In restricted filling, the S-wave becomes depressed because high left atrial pressures prevent fast filling of the LA and reduces S/D. Ar is expected to be high as shown in Figure 1.18 [14]. However, atrial mechanical dysfunction is often present in these patients and can result in low values for Ar as quoted in Table 1.2 [25, 93].

Left Ventricular Propagation Velocity

In 1992, Brun et al. applied colour M-mode Doppler to measure LV propagation velocity (V_p). Colour M-mode provides a spatial-temporal map of velocity along a line. It is displayed as a colour coded velocity image with distance along the line on the y-axis and time on the x-axis. An example is shown in Figure 1.19. Propagation velocity is typically measured as a delay in the onset of blood flow at more apical locations within the LV compared to more basal locations using a constant velocity line drawn on the spatial-temporal map, as indicated in Figure 1.19 by the slope of the white arrow. Slowed base to apex velocity propagation is attributed in part to ventricular geometry where a dilated, more spherical, ventricle results in more disordered filling

and slowed propagation [95], and to ventricular suction [96]. V_p is considered abnormal at values <45–50 cm/s [3, 93].

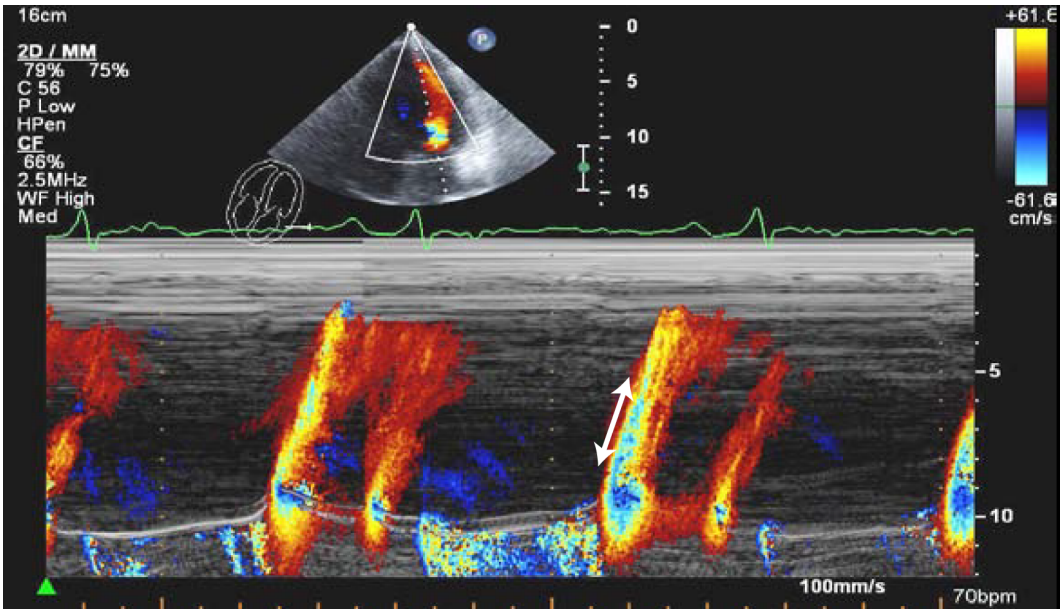

Figure 1.19: Propagation velocity from colour M-mode Dopper echocardiography. A subject with slowed propagation velocity, V_p, indicated by the slope of the white arrow, is shown. Figure from Nagueh et al. [3].

Pressure Gradients and Differences

Blood velocity parameters such as the E-wave and A-wave velocities, DT and IVRT are used to provide insight into the atrial and ventricular pressures that drive filling. Left ventricular relaxation and recoil causes the decline in LV pressure, drawing blood into the LV, and the stretched left atrium exerts pressure on the blood, also promoting filling. These pressures and resulting pressure difference, represent the forces exerted both actively and passively by the heart during diastole. Pressure differences are thus an appealing measure of diastolic function. However, the direct measure of pressure differences requires the placement of catheters within the heart at specific locations of interest. The trans-mitral pressure difference, for instance, is the measured difference in pressure between the centre of the LA and the centre of the LV.

These invasive measurements are impractical and mitral blood velocity parameters (E, A, DT) are instead used to infer the trans-mitral pressure gradient as shown above in Figure 1.18 [3, 30, 97].

Pressure gradients can also be indirectly determined by measuring blood velocity and applying the Euler equations to calculate the associated pressure gradients. The development of velocity imaging methods with improved spatial coverage such as colour M-mode Dopper echocardiography [98] and phase contrast MRI [99] now provide non-invasive methods for determining pressure gradients. Similar to velocity, the pressure gradient is a 3-dimensional vector field that varies both as a function of space and as a function of time. It can be calculated from the velocity field using the Euler equations:

$$\frac{\partial P}{\partial x} = -\rho \left[\frac{\partial v_x}{\partial t}\right] - \rho \left[v_x \cdot \frac{\partial v_x}{\partial x} + v_y \cdot \frac{\partial v_x}{\partial y} + v_z \cdot \frac{\partial v_x}{\partial z}\right] \tag{1.7}$$

$$\frac{\partial P}{\partial y} = -\rho \left[\frac{\partial v_y}{\partial t}\right] - \rho \left[v_x \cdot \frac{\partial v_y}{\partial x} + v_y \cdot \frac{\partial v_y}{\partial y} + v_z \cdot \frac{\partial v_y}{\partial z}\right] \tag{1.8}$$

$$\frac{\partial P}{\partial z} = -\rho \left[\frac{\partial v_z}{\partial t}\right] - \rho \left[v_x \cdot \frac{\partial v_z}{\partial x} + v_y \cdot \frac{\partial v_z}{\partial y} + v_z \cdot \frac{\partial v_z}{\partial z}\right] \tag{1.9}$$

where $\frac{\partial P}{\partial x}\hat{\mathbf{x}} + \frac{\partial P}{\partial y}\hat{\mathbf{y}} + \frac{\partial P}{\partial z}\hat{\mathbf{z}}$ is the net pressure gradient vector, P is pressure, x, y and z are the 3 spatial dimensions, ρ is the density of blood, t is time, v_x, v_y and v_z are velocity in the 3 spatial directions. Pressure gradients calculated using colour M-mode Doppler echocardiography-derived velocity data use a 1-dimensional version of the Euler equations where v_y and v_z are assumed to be 0. MRI is capable of acquiring 3-dimensional velocity data; however, 2-dimensional data is often acquired, in which case v_z is assumed to be 0. One-dimensional and 2-dimensional representations of diastolic pressure gradients have been validated using catheterization for both echocardiography [98, 100] and MRI [99].

Pressure differences can then be calculated from pressure gradient fields. Pressure differences are defined between 2 specified points in space (a, b) and are obtained by integrating the pressure gradient along a path connecting these points:

$$\Delta P = \int_a^b \frac{\partial P}{\partial x} dx + \int_a^b \frac{\partial P}{\partial y} dy + \int_a^b \frac{\partial P}{\partial z} dz \tag{1.10}$$

The pressure difference, ΔP, is a scalar value that varies as a function of time and is equivalent to invasively measured pressure differences. In practice, it is often further simplified by reporting only the early filling peak value, reflecting the maximum force driving filling.

The pressure difference between the LV base and apex is commonly referred to as the intra-ventricular pressure gradient (IVPG), but is more accurately described as the intra-ventricular pressure difference (IVPD). This pressure difference drives the motion of blood within the LV chamber. It was measured by Nikolic et al. using micromanometers placed at the LV apex and base using a dog model [101]. LV filling is driven by both left atrial "push" and left ventricular "suction". The IVPD, since it is measured only in the ventricle, was described as a strategy to isolate the ventricular contribution to filling and as a direct measure of ventricular suction. The IVPD in particular has been studied in the context of diastolic function in many studies including in hypertension [102], in dilated cardiomyopathy [103], as a measure of aerobic capacity in patients with diastolic heart failure [104] and as an index of LV recoil [105].

Mitral Annular Tissue Velocity

Tissue Doppler echocardiography functions on the same principle of frequency shifts as conventional Doppler but is acquired differently by focusing on lower velocities and the higher signal strength of tissue compared to blood.

For the assessment of diastolic function, tissue velocities are measured at the LV base, either on the septum or the lateral wall. The velocity of the base as it moves toward the LA during the 2 diastolic filling waves is shown in Figure 1.18 [3]. The early filling velocity of the LV base is referred to as E'. Its temporal duration is shorter than that of the E-wave and occurs during the upslope of the E-wave. Both E' and the E-wave velocity are associated with LV relaxation and elastic recoil. The E-wave velocity however, is also a function of LA filling pressures. Thus, E' can be used to normalize E and give an estimate of filling pressures [106]. When E/E' is < 8, filling pressures are considered normal. When values exceed 15, filling pressures are elevated. Between these values, other diastolic parameters are necessary estimate filling pressures [3].

Untwisting and Strain

Left ventricular untwisting rate has been used in research applications as a measure of diastolic function, but has thus far not been applied clinically. Myocardial tissue tracking methods must be used to measure untwisting and has been performed using MRI tissue tagging [71, 107] and, more recently, using speckle tracking echocardiography [26, 27]. LV twist is defined as:

$$\text{twist}(t) = \theta_{apex}(t) - \theta_{base}(t) \tag{1.11}$$

where θ refers to rotation about the LV long axis with 0° representing its position at end-diastole and t is time. Torsion is also commonly measured in addition or in lieu of twist and is defined as:

$$\text{torsion}(t) = \frac{\theta_{apex}(t) - \theta_{base}(t)}{a(t)} \tag{1.12}$$

where a is the distance between apex and base. The peak LV untwisting rate has been shown to be correlated with the relaxation time constant, τ, [107] and elastic recoil [26, 71]. Most recently, untwisting rate has also been shown to be related to diastolic filling pressures [27].

Similar to untwisting, LV myocardial strain is also largely a research tool requiring tissue tracking methods. It is calculated as the percentage change in distance between 2 points relative to its end-diastolic distance as follows:

$$\epsilon(t) = \frac{d(t) - d_{ED}}{d_{ED}} \tag{1.13}$$

where ϵ is strain, d is the distance between 2 points and ED is end-diastole. Strain is a 1-dimensional parameter and is usually measured in longitudinal, circumferential and radial (endocardium to epicardium) directions. Mitral annular displacement is directly related to longitudinal strain and mitral annular velocity can be considered a surrogate for LV longitudinal strain rate. Strain can be used to assess regional abnormalities in myocardial deformation for the study of myocardial stunning or viability [108, 109] and global strain rate has also been used to represent relaxation [28].

1.5 Scope of Thesis

The remaining chapters of this thesis describe the research results contributing to field of cardiac MRI for diastolic function. In Chapter 2, SSFP imaging and myocardial tissue tagging were used to quantify LV chamber deformation during isovolumic relaxation (IVR). The phases of diastole can be described sequentially, as isovolumic relaxation, early filling (E-wave), diastasis and atrial contraction (A-wave). IVR refers to the portion of the cardiac cycle following aortic valve closure (AVC) but before mitral valve opening (MVO).

IVR has received special attention from researchers because the left ventricle is relaxing and the closed mitral valve isolates the chamber from left atrial pressure during this time. Because of these conditions, ventricular measurements made during IVR have been interpreted as directly related to LV relaxation and independent of loading conditions, such as hydration and venous return [26–28]. The findings reported in Chapter 2 confirm that isovolumic LV strain is related to LV relaxation but also show that it is related to the material and functional properties of the mitral valve leaflets and left atrial pressure, disputing the assertion that isovolumic LV strain is independent of loading conditions.

Chapters 3, 4 and 5 focus on the ventricular filling portion of diastole. During filling, blood moves into the LV, passing first though the left atrium (LA). Both the LV and the LA play important roles in modulating ventricular filling. For the LV, its shape, the mechanisms of LV relaxation and its passive stiffness together dictate blood flow into the chamber [25]. For the LA, its relaxation and elastic properties determine diastolic preload and atrial contraction supplies additional filling [29]. Phase contrast MRI was used to study blood flow dynamics during the filling phases with Chapter 3 focusing on blood flow in the LV, Chapter 4 focusing on blood flow in the LA and Chapter 5 using blood velocity to calculate pressure gradients in both the LA and LV.

Mitral blood velocity and blood flow are often considered interchangable, but in Chapter 3, blood flow-derived diastolic parameters are shown to be different from blood velocity-derived parameters. Blood flow in the LA has not received as much attention in the literature as mitral blood flow. In Chapter 4, LA propagation velocity is described as a new measure of diastolic function related to its compliance. It is characterized throughout the cardiac cycle in a

group of normal healthy subjects. Pressure gradients are related to blood velocity because they represent the forces responsible for the movement of blood [3, 30]. In Chapter 5, pressure difference measures were found to provide limited value beyond information provided by assessments of blood velocity.

Diastolic dysfunction can also be considered, in a broader context, by looking at systolic function in the presence of diastolic dysfunction. While systolic and diastolic dysfunction are often present together, diastolic dysfunction may also be present without apparent changes in EF [14]. In these cases systolic function is often interpreted as normal; however, some studies have shown abnormalities in LV systolic strain despite preserved EF [31–37]. Currently, methods to measure myocardial strain using MRI involve specialized acquisition protocols and onerous post-processing [38–44]. Strain is more commonly measured using speckle tracking echocardiography [45, 46] which has the disadvantage of being limited by acoustic window. In Chapter 6, a new technique, called surface strain, was developed to measure whole-heart strain using standard SSFP cine imaging. Surface strains were vaildated against traditional tissue tagging techniques in subjects ranging from healthy to those with systolic heart failure.

The final chapter of this thesis describes the limitations of these tools and provides some direction towards the future. Some of the parameters described in this thesis will benefit from further refinement in terms of data acquisition and analysis, for which suggestions are outlined. Other parameters are ready for application in patient populations. For these, patient populations where these parameters may be of interest are suggested.

1.6 Chapter 1 References

[1] Kilner PJ. Imaging congenital heart disease in adults. *Br J Radiol*, 84:S258–68, 2011.

[2] Lang RM, Bierig M, Devereux RB, Flachskampf FA, Foster E, Pellikka PA, Picard MH, Roman MJ, Seward J, Shanewise JS, Solomon SD, Spencer KT, Sutton MS, Stewart WJ, Chamber Quantification Writing Group, American Society of Echocardiography's Guidelines, Standards Committee, and European Association of Echocardiography. Recommendations for chamber quantification: a report from the American Society of Echocardiography's Guidelines and Standards Committee and the Chamber Quantification Writing Group, developed in conjunction with the European Association of Echocardiography, a branch of the European Society of Cardiology. *J Am Soc Echocardiogr*, 18:1440–63, 2005.

[3] Nagueh SF, Appleton CP, Gillebert TC, Marino PN, Oh JK, Smiseth OA, Waggoner AD, Flachskampf FA, Pellikka PA, and Evangelisa A. Recommendations for the evaluation of left ventricular diastolic function by echocardiography. *Eur J Echocardiogr*, 10:165–93, 2009.

[4] Pakkal M, Raj V, and McCann GP. Non-invasive imaging in coronary artery disease including anatomical and functional evaluation of ischaemia and viability assessment. *Br J Radiol*, 84:S280–95, 2011.

[5] Matsumoto N, Sato Y, Yoda S, Nakano Y, Kunimasa T, Matsuo S, Komatsu S, Saito S, and Hirayama A. Prognostic value of non-obstructive

ct low-dense coronary artery plaques detected by multislice computed tomography. *Circ J*, 71:1898–903, 2007.

[6] Notghi A and Low CS. Myocardial perfusion scintigraphy: past, present and future. *Br J Radiol*, 84:S229–36, 2011.

[7] Germain P, Roul G, Kastler B, Mossard JM, Bareiss P, and Sacrez A. Inter-study variability in left ventricular mass measurement. Comparison between M-mode echography and MRI. *Eur Heart J*, 13:1011–9, 1992.

[8] Hundley WG, Meshack BM, Willett DL, Sayad DE, Lange RA, Willard JE, Landau C, Hillis LD, and Peshock RM. Comparison of quantitation of left ventricular volume, ejection fraction, and cardiac output in patients with atrial fibrillation by cine magnetic resonance imaging versus invasive measurements. *Am J Cardiol*, 78:1119–23, 1996.

[9] Kaandorp TA, Lamb HJ, van der Wall EE, de Roos A, and Bax JJ. Cardiovascular MR to access myocardial viability in chronic ischaemic LV dysfunction. *Heart*, 91:1359–65, 2005.

[10] Kalogeropoulos AP, Georgiopoulou VV, Gheorghiade M, and Butler J. Echocardiographic evaluation of left ventricular structure and function: new modalities and potential applications in clinical trials. *J Card Fail*, 18(2):159–72, 2012.

[11] European Study Group on Diastolic Heart Failure. How to diagnose diastolic heart failure. *Eur Heart J*, 19:990–1003, 1998.

[12] Gandhi SK, Powers JC, Nomeir AM, Fowle K, Kitzman DW, Rankin KM, and Little WC. The pathogenesis of acute pulmonary edema associated with hypertension. *N Engl J Med*, 344:17–22, 2001.

[13] Vasan RS and Levy D. Defining diastolic heart failure: a call for standardized diagnostic criteria. *Circulation*, 101:2118–21, 2000.

[14] Zile MR and Brutsaert DL. New concepts in diastolic dysfunction and diastolic heart failure: part I: diagnosis, prognosis, and measurements of diastolic function. *Circulation*, 105:1387–93, 2002.

[15] Hogg K, Swedberg K, and McMurray J. Heart failure with preserved left ventricular systolic function; epidemiology, clinical characteristics, and prognosis. *J Am Coll Cardiol*, 43:317–27, 2004.

[16] Apstein CS and Grossman W. Opposite initial effects of supply and demand ischemia on left ventricular diastolic compliance: the ischemia-diastolic paradox. *J Mol Cell Cardiol*, 19:119–28, 1987.

[17] Albanna II, Eichelberger SM, Khoury PR, Witt SA, Standiford DA, Dolan LM, Daniels SR, and Kimball TR. Diastolic dysfunction in young patients with insulin-dependent diabetes mellitus as determined by automated border detection. *J Am Soc Echocardiogr*, 11:349–55, 1998.

[18] Zabalgoitia M, Ismaeil MF, Anderson L, and Maklady FA. Prevalence of diastolic dysfunction in normotensive, asymptomatic patients with well-controlled type 2 diabetes mellitus. *Am J Cardiol*, 87:320–3, 2001.

[19] Levy D, Kenchaiah S, Larson MG, Benjamin EJ, Kupka MJ, Ho KK, Murabito JM, and Vasan RS. Long-term trends in the incidence of and survival with heart failure. *N Engl J Med*, 347:1397–402, 2002.

[20] McMurry JJ, Petrie MC, Murdoch DR, and Davie AP. Clinical epidemiology of heart failure: public and private health burden. *Eur Heart J*, 19 Suppl P:P9–16, 1998.

[21] Bui AL, Horwich TB, and Fonarow GC. Epidemiology and risk profile of heart failure. *Nat Rev Cardiol*, 8:30–41, 2011.

[22] Aurigemma GP, Zile MR, and Gaasch WH. Contractile behavior of the left ventricle in diastolic heart failure: with emphasis on regional systolic function. *Circulation*, 113:296–304, 2006.

[23] Burkhoff D, Mirsky I, and Suga H. Assessment of systolic and diastolic ventricular properties via pressure-volume analysis: a guide for clinical, translational, and basic researchers. *Am J Physiol Heart Circ Physiol*, 289:H501–12, 2005.

[24] Zile MR, Baicu CF, and Gaasch WH. Diastolic heart failure–abnormalities in active relaxation and passive stiffness of the left ventricle. *N Engl J Med*, 350:1953–9, 2004.

[25] Appleton CP, Hatle LK, and Popp RL. Relation of transmitral flow velocity patterns to left ventricular diastolic function: new insights from a combined hemodynamic and Doppler echocardiographic study. *J Am Coll Cardiol*, 12:426–40, 1988.

[26] Notomi Y, Martin-Miklovic MG, Oryszak SJ, Shiota T, Deserranno D, Popovic ZB, Garcia MJ, Greenberg NL, and Thomas JD. Enhanced ventricular untwisting during exercise: a mechanistic manifestation of elastic recoil described by Doppler tissue imaging. *Circulation*, 113:2524–4533, 2006.

[27] Opdahl A, Remme EW, Helle-Valle T, Edvardsen T, and Smiseth OA. Myocardial relaxation, restoring forces, and early-diastolic load are independent determinants of left ventricular untwisting rate. *Circulation*, 126:1441–51, 2012.

[28] Wang J, Khoury DS, Thohan V, Torre-Amione G, and Nagueh SF. Global diastolic strain rate for the assessment of left ventricular relaxation and filling pressures. *Circulation*, 115:1376–83, 2007.

[29] Pagel PS, Kehl F, Gare M, Hettrick DA, Kersten JR, and Warltier DC. Mechanical function of the left atrium – New insights based on analysis of pressure-volume relations and Doppler echocardiography. *Anesthesiology*, 98:975–94, 2003.

[30] Oh JK, Seward JB, and Tajik AJ. Assessment of Diastolic Function. In *The Echo Manual*, pages 45–57. Lippincott Williams and Wilkins, Philadelphia, second edition, 1999.

[31] Kosmala W, Plaksej R, Strotmann JM, Weigel C, Herrmann S, Niemann M, Mende H, Stork S, Angermann CE, Wagner JA, and Weidemann F. Progression of left ventricular functional abnormalities in hypertensive patients with heart failure: an ultrasonic two-dimensional speckle tracking study. *J Am Soc Echocardiogr*, 21:1309–17, 2008.

[32] Eleid MF, Caracciolo G, Cho EJ, Scott RL, Steidley DE, Wilansky S, Arabia FA, Khandheria BK, and Sengupta PP. Natural history of left ventricular mechanics in transplanted hearts: relationships with clinical variables and genetic expression profiles of allograft rejection. *JACC Cardiovasc Imaging*, 3:988–1000, 2010.

[33] Ng AC, Delgado V, Bertini M, van der Meer RW, Rijzewijk LJ, Hooi Ewe S, Siebelink HM, Smit JW, Diamant M, Romijn JA, de Roos A, Leung DY, Lamb HJ, and Bax JJ. Myocardial steatosis and biventricular strain and strain rate imaging in patients with type 2 diabetes mellitus. *Circulation*, 122(24):2538–44, 2010.

[34] Smedsrud MK, Pettersen E, Gjesdal O, Svennevig JL, Andersen K, Ihlen H, and Edvardsen T. Detection of left ventricular dysfunction by global longitudinal systolic strain in patients with chronic aortic regurgitation. *J Am Soc Echocardiogr*, 24(11):1253–9, 2011.

[35] Saito M, Okayama H, Yoshii T, Higashi H, Morioka H, Hiasa G, Sumimoto T, Inaba S, Nishimura K, Inoue K, Ogimoto A, Shigematsu Y, Hamada M, and Higaki J. Clinical significance of global two-dimensional strain as a surrogate parameter of myocardial fibrosis and cardiac events in patients with hypertrophic cardiomyopathy. *Eur Heart J Cardiovasc Imaging*, 13(7):617–23, 2011.

[36] Fallah-Rad N, Walker JR, Wassef A, Lytwyn M, Bohonis S, Fang T, Tian G, Kirkpatrick ID, Singal PK, Krahn M, Grenier D, and Jassal DS. The utility of cardiac biomarkers, tissue velocity and strain imaging, and cardiac magnetic resonance imaging in predicting early left ventricular dysfunction in patients with human epidermal growth factor receptor II-positive breast cancer treated with adjuvant trastuzumab therapy. *J Am Coll Cardiol*, 57(22):2263–70, 2011.

[37] Ho E, Brown A, Barrett P, Morgan RB, King G, Kennedy MJ, and Murphy RT. Subclinical anthracycline- and trastuzumab-induced cardiotoxicity in the long-term follow-up of asymptomatic breast cancer survivors: a speckle tracking echocardiographic study. *Heart*, 96(9):701–7, 2010.

[38] Osman NF, Kerwin WS, McVeigh ER, and Prince JL. Cardiac motion tracking using cine harmonic phase (HARP) magnetic resonance imaging. *Magn Reson Med*, 42(6):1048–60, 1999.

[39] Axel L and Dougherty L. MR imaging of motion with spatial modulation of magnetization. *Radiology*, 171:841–5, 1989.

[40] Mosher TJ and Smith MB. A DANTE tagging sequence for the evaluation of translational sample motion. *Magn Reson Med*, 15(2):334–9, 1990.

[41] Fischer SE, McKinnon GC, Maier SE, and Boesiger P. Improved myocardial tagging contrast. *Magn Reson Med*, 30(2):191–200, 1993.

[42] Pelc LR, Sayre J, Yun K, Castro LJ, Herfkens RJ, Miller DC, and Pelc NJ. Evaluation of myocardial motion tracking with cine-phase contrast magnetic resonance imaging. *Invest Radiol*, 29(12):1038–42, 1994.

[43] Aletras AH, Ding S, Balaban RS, and Wen H. DENSE: displacement encoding with stimulated echoes in cardiac functional MRI. *J Magn Reson*, 137(1):247–52, 1999.

[44] Osman NF, Sampath S, Atalar E, and Prince JL. Imaging longitudinal cardiac strain on short-axis images using strain-encoded MRI. *Magn Reson Med*, 46(2):324–34, 2001.

[45] Heimdal A, Stoylen A, Torp H, and Skjaerpe T. Real-time strain rate imaging of the left ventricle by ultrasound. *J Am Soc Echocardiogr*, 11(11):1013–9, 1998.

[46] Amundsen BH, Helle-Valle T, Edvardsen T, Torp H, Crosby J, Lyseggen E, Stylen A, Ihlen H, Lima JA, Smiseth OA, and Slrdahl SA. Noninvasive myocardial strain measurement by speckle tracking echocardiography: validation against sonomicrometry and tagged magnetic resonance imaging. *J Am Coll Cardiol*, 47:789–93, 2006.

[47] Fuster V, Walsh RA, and Harrington RA. *Hurst's The Heart*. McGraw-Hill, thirteenth edition, 2011.

[48] Klein AL and Garcia MJ. *Diastology: Clinical Approach to Diastolic Heart Failure*. Elsevier, 2008.

[49] Mohrman DE and Heller LJ. *Cardiovascular Physiology*. McGraw-Hill, seventh edition, 2010.

[50] Hawkes RC, Holland GN, Moore WS, Roebuck EJ, and Worthington BS. Nuclear magnetic resonance (NMR) tomography of the normal heart. *J Comput Assist Tomogr*, 5:605–12, 1981.

[51] Hinshaw WS, Bottomley PA, and Holland GN. Radiographic thin-section image of the human wrist by nuclear magnetic resonance. *Nature*, 270:722–3, 1977.

[52] Berninger WH, Redington RW, Doherty P, Lipton MJ, and Carlsson E. Gated cardiac scanning: canine studies. *J Comput Assist Tomogr*, 3:155–63, 1979.

[53] Heidelberger E, Petersen SB, and Lauterbur PC. Aspects of cardiac diagnosis using synchronized NMR imaging. *Eur J Radiol*, 3 Suppl 1:281–5, 1983.

[54] van Dijk P. ECG-triggered NMR imaging of the heart. *Diagn Imaging Clin Med*, 53:29–37, 1984.

[55] Lanzer P, Botvinick EH, Schiller NB, Crooks LE, Arakawa M, Kaufman L, Davis PL, Herfkens R, Lipton MJ, and Higgins CB. Cardiac imaging using gated magnetic resonance. *Radiology*, 150:121–7, 1984.

[56] Haase A, Frahm J, Matthaei D, Hanicke W, and Merboldt KD. FLASH imaging: rapid NMR imaging using low flip-angle pulses. *J Magn Reson*, 67:258–66, 1986.

[57] Sechtem U, Pflugfelder PW, White RD, Gould RG, Holt W, Lipton MJ, and Higgins CB. Cine MR imaging: potential for the evaluation of cardiovascular function. *AJR Am J Roentgenol*, 148:239–46, 1987.

[58] Atkinson DJ and Edelman RR. Cineangiography of the heart in a single breath hold with a segmented turboFLASH sequence. *Radiology*, 178:357–60, 1991.

[59] Carr HY. Steady-state free precession in nuclear magnetic resonance. *Phys Rev*, 112:1693–701, 1958.

[60] Oppelt A. FISP. A new fast MRI sequence. *Electromedia*, 3:15–8, 1986.

[61] Carr JC, Simonetti O, Bundy J, Li D, Pereles S, and Finn JP. Cine MR angiography of the heart with segmented true fast imaging with steady-state precession. *Radiology*, 219:828–32, 2001.

[62] Thiele H, Nagel E, Paetsch I, Schnackenburg B, Bornstedt A, Kouwenhoven M, Wahl A, Schuler G, and Fleck E. Functional cardiac mr imaging with steady-state free precession (SSFP) significantly improves endocardial border delineation without contrast agents. *J Magn Reson Imaging*, 14:362–7, 2001.

[63] Barkhausen J, Ruehm SG, Goyen M, Buck T, Laub G, and Debatin JF. MR evaluation of ventricular function: True fast imaging with steady-state precession versus fast low-angle shot cine MR imaging: feasibility study. *Radiology*, 219:264–9, 2001.

[64] Plein S, Bloomer TN, Ridgway JP, Jones TR, Bainbridge GJ, and Sivananthan MU. Steady-state free precession magnetic resonance imaging of the heart: comparison with segmented k-space gradient-echo imaging. *J Magn Reson Imaging*, 4:507–13, 2002.

[65] Wacker CM, Bock M, Hartlep AW, Beck G, van Kaick G, Ertl G, Bauer WR, and Schad LR. Changes in myocardial oxygenation and perfusion under pharmacological stress with dipyridamole: assessment using T*2 and T1 measurements. *Magn Reson Med*, 41:686–95, 1999.

[66] Foltz WD, Al-Kwifi O, Sussman MS, Stainsby JA, and Wright G. Optimized spiral imaging for measurement of myocardial T2 relaxation. *Magn Reson Med*, 49:1089–97, 2003.

[67] Giri S, Chung YC, Merchant A, Mihai G, Rajagopalan S, Raman SV, and Simonetti OP. T2 quantification for improved detection of myocardial edema. *J Cardiovasc Magn Reson*, 11:56, 2009.

[68] Bryant DJ, Payne JA, Firmin DN, and Longmore DB. Measurement of flow with NMR imaging using a gradient pulse and phase difference technique. *J Comput Assist Tomogr*, 8:588–93, 1984.

[69] Weiss JL, Frederiksen JW, and Weisfeldt ML. Hemodynamic determinants of the time-course of fall in canine left ventricular pressure. *J Clin Invest*, 58:751–60, 1976.

[70] Rademakers FE, Buchalter MB, Rogers WJ, Zerhouni EA, Weisfeldt ML, Weiss JL, and Shapiro EP. Dissociation between left ventricular untwisting and filling. Accentuation by catecholamines. *Circulation*, 85:1572–81, 1992.

[71] Thompson RB, Paterson I, Chow K, Cheng-Baron J, Scott JM, Esch BT, Ennis DB, and Haykowsky MJ. Characterization of the relationship between systolic shear strain and early diastolic shear strain rates: insights into torsional recoil. *Am J Physiol Heart Circ Physiol*, 299:H898–907, 2010.

[72] Sengupta PP, Tajik AJ, Chandrasekaran K, and Khandheria BK. Twist mechanics of the left ventricle: principles and application. *JACC Cardiovasc Imaging*, 1:366–76, 2008.

[73] Esch BT, Scott JM, Warburton DE, Thompson R, Taylor D, Cheng Baron J, Paterson I, and Haykowsky MJ. Left ventricular torsion and untwisting during exercise in heart transplant recipients. *J Physiol*, 587:2375–86, 2009.

[74] Notomi Y, Lysyansky P, Setser RM, Shiota T, Popovic ZB, Martin-Miklovic MG, Weaver JA, Oryszak SJ, Greenberg NL, White RD, and Thomas JD. Measurement of ventricular torsion by two-dimensional ultrasound speckle tracking imaging. *J Am Coll Cardiol*, 45:2034–41, 2005.

[75] Cheng-Baron J, Chow K, Khoo NS, Esch BT, Scott JM, Haykowsky MJ, Tyberg JV, and Thompson RB. Measurements of changes in left ventricular volume, strain, and twist during isovolumic relaxation using MRI. *Am J Physiol Heart Circ Physiol*, 298:H1908–18, 2010.

[76] Nikolic S, Yellin EL, Tamura K, Vetter H, Tamura T, Meisner JS, and Frater RW. Passive properties of canine left ventricle: diastolic stiffness and restoring forces. *Circ Res*, 62:1210–22, 1988.

[77] Yellin EL, Hori M, Yoran C, Sonnenblick EH, Gabbay S, and Frater

RW. Left ventricular relaxation in the filling and nonfilling intact canine heart. *Am J Physiol*, 250:H620–9, 1986.

[78] Spencer KT, Mor-Avi V, Gorcsan J 3rd, DeMaria AN, Kimball TR, Monaghan MJ, Perez JE, Weinert L, Bednarz J, Edelman K, Kwan OL, Glascock B, Hancock J, Baumann C, and Lang RM. Effects of aging on left atrial reservoir, conduit, and booster pump function: a multi-institution acoustic quantification study. *Heart*, 85:272–7, 2001.

[79] Barbier P, Solomon SB, Schiller NB, and Glantz SA. Left atrial relaxation and left ventricular systolic function determine left atrial reservoir function. *Circulation*, 100:427–36, 1999.

[80] Hitch DC and Nolan SP. Descriptive analysis of instantaneous left atrial volume with special reference to left atrial function. *J Surg Res*, 30:110–20, 1981.

[81] Gaasch WH and Zile MR. Left ventricular structural remodeling in health and disease: with special emphasis on volume, mass, and geometry. *J Am Coll Cardiol*, 58:1733–40, 2011.

[82] Pennell DJ. Ventricular volume and mass by CMR. *J Cardiovasc Magn Reson*, 4:507–13, 2002.

[83] Bellenger NG, Davies LC, Francis JM, Coats AJ, and Pennell DJ. Reduction in sample size for studies of remodeling in heart failure by the use of cardiovascular magnetic resonance. *Cardiovasc Magn Reson*, 2:271–8, 2000.

[84] Buck T, Hunold P, Wentz KU, Tkalec W, Nesser HJ, and Erbel R. Tomographic three-dimensional echocardiographic determination of chamber size and systolic function in patients with left ventricular aneurysm:

comparison to magnetic resonance imaging, cineventriculography, and two-dimensional echocardiography. *Circulation*, 96:4286–97, 1997.

[85] Gopal AS, Keller AM, Shen Z, Sapin PM, Schroeder KM, King DL Jr, and King DL. Three-dimensional echocardiography: in vitro and in vivo validation of left ventricular mass and comparison with conventional echocardiographic methods. *J Am Coll Cardiol*, 24:504–13, 1994.

[86] Hudsmith LE, Petersen SE, Francis JM, Robson MD, and Neubauer S. Normal human left and right ventricular and left atrial dimensions using steady state free precession magnetic resonance imaging. *J Cardiovasc Magn Reson*, 7:775–82, 2005.

[87] Maceira AM, Cosn-Sales J, Roughton M, Prasad SK, and Pennell DJ. Reference left atrial dimensions and volumes by steady state free precession cardiovascular magnetic resonance. *J Cardiovasc Magn Reson*, 12:65, 2010.

[88] Abhayaratna WP, Seward JB, Appleton CP, Douglas PS, Oh JK, Tajik AJ, and Tsang TS. Left atrial size: physiologic determinants and clinical applications. *J Am Coll Cardiol*, 47:2357–63, 2006.

[89] Gardin JM, Drayer JI, Weber M, Rohan MK, Knoll M, Shu VW, Garcia R, Brewer D, and Henry WL. Doppler echocardiographic assessment of left ventricular systolic and diastolic function in mild hypertension. *Hypertension*, 9:II90–6, 1987.

[90] Kitabatake A, Inoue M, Asao M, Tanouchi J, Masuyama T, Abe H, Morita H, Senda S, and Matsuo H. Transmitral blood flow reflecting diastolic behavior of the left ventricle in health and disease–a study by pulsed Doppler technique. *Jpn Circ J*, 46:92–102, 1982.

[91] Klein AL, Hatle LK, Taliercio CP, Oh JK, Kyle RA, Gertz MA, Bailey KR, Seward JB, and Tajik AJ. Prognostic significance of Doppler measures of diastolic function in cardiac amyloidosis. A Doppler echocardiography study. *Circulation*, 83:808–16, 1991.

[92] Kuo LC, Quinones MA, Rokey R, Sartori M, Abinader EG, and Zoghbi WA. Quantification of atrial contribution to left ventricular filling by pulsed Doppler echocardiography and the effect of age in normal and diseased hearts. *Am J Cardiol*, 59:1174–8, 1987.

[93] Garcia MJ, Thomas JD, and Klein AL. New Doppler echocardiographic applications for the study of diastolic function. *J Am Coll Cardiol*, 32:865–75, 1998.

[94] Klein AL and Tajik AJ. Doppler assessment of pulmonary venous flow in healthy subjects and in patients with heart disease. *J Am Soc Echocardiogr*, 4:379–92, 1991.

[95] Vierendeels JA, Dick E, and Verdonck PR. Hydrodynamics of color M-mode Doppler flow wave propagation velocity V(p): a computer study. *J Am Soc Echocardiogr*, 15:219–24, 2002.

[96] Brun P, Tribouilloy C, Duval AM, Iserin L, Meguira A, Pelle G, and Dubois-Rande JL. Left ventricular flow propagation during early filling is related to wall relaxation: a color M-mode Doppler analysis. *J Am Coll Cardiol*, 20:420–32, 1992.

[97] Appleton CP, Jensen JL, Hatle LK, and Oh JK. Doppler evaluation of left and right ventricular diastolic function: a technical guide for obtaining optimal flow velocity recordings. *J Am Soc Echocardiogr*, 10(3):271–92, 1997.

[98] Greenberg NL, Vandervoort PM, Firstenberg MS, Garcia MJ, and Thomas JD. Estimation of diastolic intraventricular pressure gradients by Doppler M-mode echocardiography. *Am J Physiol Heart Circ Physiol*, 280:H2507–15, 2001.

[99] Thompson RB and McVeigh ER. Fast measurement of intracardiac pressure differences with 2d breath-hold phase-contrast mri. *Magn Reson Med*, 49:1056–66, 2003.

[100] Rovner A, Smith R, Greenberg NL, Tuzcu EM, Smedira N, Lever HM, Thomas JD, and Garcia MJ. Improvement in diastolic intraventricular pressure gradients in patients with hocm after ethanol septal reduction. *Am J Physiol Heart Circ Physiol*, 285:H2492–9, 2003.

[101] Nikolic SD, Feneley MP, Pajaro OE, Rankin JS, and Yellin EL. Origin of regional pressure gradients in the left ventricle during early diastole. *Am J Physiol*, 268:H550–7, 1995.

[102] Rovner A, de las Fuentes L, Waggoner AD, Memon N, Chohan R, and Dvila-Romn VG. Characterization of left ventricular diastolic function in hypertension by use of doppler tissue imaging and color m-mode techniques. *J Am Soc Echocardiogr*, 19:872–9, 2006.

[103] Yotti R, Bermejo J, Antoranz JC, Desco MM, Cortina C, Rojo-Alvarez JL, Allu C, Martn L, Moreno M, Serrano JA, Muoz R, and Garca-Fernndez MA. A noninvasive method for assessing impaired diastolic suction in patients with dilated cardiomyopathy. *Circulation*, 112:2921–9, 2005.

[104] Rovner A, Greenberg NL, Thomas JD, and Garcia MJ. Relationship of diastolic intraventricular pressure gradients and aerobic capacity in

patients with diastolic heart failure. *Am J Physiol Heart Circ Physiol*, 289:H2081–8, 2005.

[105] Firstenberg MS, Greenberg NL, Garcia MJ, and Thomas JD. Relationship between ventricular contractility and early diastolic intraventricular pressure gradients: a diastolic link to systolic function. *J Am Soc Echocardiogr*, 21:501–6, 2008.

[106] Nagueh SF, Middleton KJ, Kopelen HA, Zoghbi WA, and Quiones MA. Doppler tissue imaging: a noninvasive technique for evaluation of left ventricular relaxation and estimation of filling pressures. *J Am Coll Cardiol*, 30:1527–33, 1997.

[107] Dong SJ, Hees PS, Siu CO, Weiss JL, and Shapiro EP. MRI assessment of LV relaxation by untwisting rate: a new isovolumic phase measure of tau. *Am J Physiol Heart Circ Physiol*, 281:H2002–9, 2001.

[108] Park TH, Nagueh SF, Khoury DS, Kopelen HA, Akrivakis S, Nasser K, Ren G, and Frangogiannis NG. Impact of myocardial structure and function postinfarction on diastolic strain measurements: implications for assessment of myocardial viability. *Am J Physiol Heart Circ Physiol*, 209:H724–31, 2006.

[109] Pislaru C, Bruce CJ, Anagnostopoulos PC, Allen JL, Seward JB, Pellikka PA, Ritman EL, and Greenleaf JF. Ultrasound strain imaging of altered myocardial stiffness: stunned versus infarcted reperfused myocardium. *Circulation*, 109:2905–10, 2004.

Chapter 2

Measurements of Changes in Left Ventricular Volume, Strain, and Twist during Isovolumic Relaxation using MRI[1]

2.1 Introduction

Diastole is divided into isovolumic relaxation (IVR) and ventricular filling. During IVR, which is defined by mitral and aortic valves being closed, active relaxation of the left ventricle (LV) results in the rapid decline of LV pressure. While LV volume is commonly assumed to be unchanged during IVR, previous studies have measured changes in LV dimensions during this period. Specifically, increases in LV base-to-apex length have been observed to occur during IVR in dogs [1, 2], and increases in LV circumference or transverse diameter have also been observed during IVR in dogs [3] and sheep [4].

[1] A version of this chapter has been published: Cheng-Baron J, Chow K, Khoo NS, Esch BT, Scott JM, Haykowsky MJ, Tyberg JV, Thompson RB. Measurements of changes in left ventricular volume, strain, and twist during isovolumic relaxation using MRI. *Am J Physiol Heart Circ Physiol*. 2010;298:H1908-18.

In humans, the outward motion of the LV wall has been reported, sometimes with an accompanying, but smaller, inward motion [5, 6]. While these observations were suggestive of volume changes, it is possible that these observations reflected only regional tissue deformation and were not representative of an actual global change in LV volume. Additionally, close examination of published volume-time curves show apparent volume increases during IVR [7–12]. These volume changes have been proposed to be due to errors in measurement techniques, possibly reflecting regional geometric changes of the LV chamber [8]. LV myocardial tissue deformation during IVR has also been measured in terms of circumferential (E_{cc}), longitudinal (E_{ll}), and radial (E_{rr}) tissue strains [13, 14] and LV twist [15–20]. The aim of this study is to use magnetic resonance imaging (MRI) to measure LV volume during IVR and to determine its relationship to myocardial tissue deformation measured in terms of circumferential, longitudinal and radial strains and twist. While true chamber volume is assumed to be constant during IVR, we hypothesize that imaging-derived volumes increase during IVR and represent myocardial expansion resulting from changes in myocardial tissue strain as the LV relaxes.

2.2 Methods

Ten healthy subjects (6 males, 26.9 ± 3.8 yrs) were recruited to participate in this study. The protocol was approved by the University of Alberta Health Research Ethics Board, and all participants provided informed consent prior to participation. The subjects underwent comprehensive cardiac MRI and echocardiography exams. MRI was used to measure time-courses of LV volume, E_{cc}, E_{ll}, E_{rr}, and twist, while echocardiography was used to observe mitral leaflet motion.

2.2.1 Defining LV Volume

While LV volume must be constant during IVR when it is defined by closed mitral and aortic valves, commonly used methods for volume determination use only endocardial borders, as shown in Figure 2.1, and are thus not constrained by the closed heart valves. A plane is used to define the extent of the LV as opposed to the mitral valve itself, and thus deformation of the closed valve towards the LV interior can result in an increase in measured volume. This measurement approach is consistent with the method of disks commonly used with MRI data [11, 21, 22] and various methods of volume determination used with echocardiography [23], all of which exclude the complex geometry of the LV at the leaflets and measure the LV chamber volume as it is defined by the extent of the myocardium.

2.2.2 Data Acquisition

Imaging Modalities

MRI provides a more reproducible measure of LV volume than echocardiography [21], is similar to echocardiography for determination of tissue strains [24, 25], and is similar or superior to echocardiography for the quantification of ventricular rotation or twist [17, 26, 27]. MRI was used to measure the time-course of LV volume because it is important for the purposes of this study that LV volume be reliably measured without using geometric assumptions of LV shape employed by 1-dimensional or 2-dimensional echocardiography (Simpson's biplane or area-length methods). MRI was also used to measure the time-courses of LV tissue strains (circumferential, longitudinal, and radial) and LV twist to allow for a direct comparison of these measures with LV volume; using MRI, strain and twist data were acquired within 10 minutes of

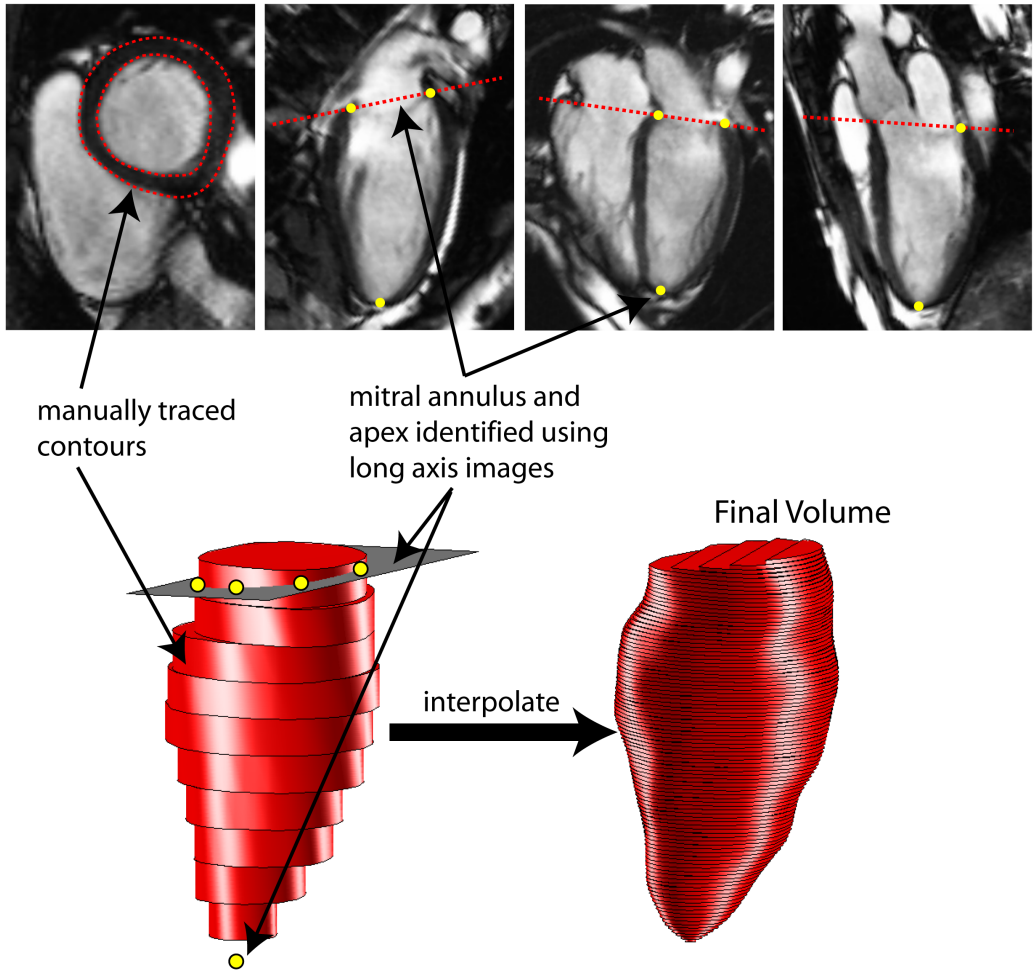

Figure 2.1: LV volume determined using disk summation. Disks are produced from segmentation on a short-axis stack of images. Disk edges are smoothly jointed to adjacent disks and combined with base and apex positions from long-axis images, allowing fractional inclusion or extension of disks.

volume data, without moving the subject, and under identical physiologic conditions. However, MRI does not provide a robust assessment of mitral leaflet geometry or motion, and thus echocardiography was used to measure mitral leaflet motion throughout IVR.

MRI Evaluation

All MRI images were acquired using a 1.5 T scanner (Sonata; Siemens Healthcare, Erlangen, Germany). Image acquisitions were cardiac gated (electrocardiogram) and performed during breath holds at end-expiration. Blood pressure was monitored using an automated blood pressure cuff.

Cardiac cine images of the 2-chamber, 3-chamber, and 4-chamber long-axis views and a short-axis stack spanning the full LV were acquired using a steady state free precession (SSFP) sequence. Typical sequence parameters were as follows: 8 mm slice thickness, 2 mm gap between short-axis slices, 1.5 ms echo time (TE), 3.0 ms repetition time (TR), (94–146) $\times$ 256 matrix, 65° flip angle, (207–288) $\times$ 400 mm field of view (FOV), 238 kHz bandwidth (BW), rate 2 parallel imaging and 12 views per segment (VPS) for an acquired temporal resolution of 39 ms per cardiac phase.

Myocardial tissue tagging was used to measure tissue deformation. In the short-axis orientation, a gradient echo sequence with 8 mm grid tags was used for 5 evenly spaced slices spanning the length of the LV. Tags were applied following a delay of 200 ms from the electrocardiogram R-wave to ensure the persistence of tags throughout diastole. Typical sequence parameters were as follows: 8 mm slice thickness, 8 mm gap between slices, 2.8 ms TE, 4.6 ms TR, 75 $\times$ 192 matrix, 14° flip angle, (200–225) $\times$ 400 mm FOV, 58 kHz BW, and 5 VPS for an acquired temporal resolution of 23 ms per cardiac phase. In the long-axis slice orientations (2-chamber, 3-chamber and 4-chamber), linear

tags were spaced 8 mm apart and perpendicular to the long-axis of the LV with similar sequence parameters.

Phase contrast MRI was used to acquire blood-velocity maps. The through-plane component of velocity was acquired for a short-axis slice located at the mitral valve. Typical sequence parameters were as follows: 8 mm slice thickness, 3.2 ms TE, 4.9 ms TR, 75 × 128 matrix, 30° flip angle, 1.2 m/s velocity encoding strength, (187–275) × 400 mm FOV, 58 kHz BW, rate 2 parallel imaging (GRAPPA), 3 VPS and 2 phase encoding steps for an acquired temporal resolution of 29.5 ms per cardiac phase.

Echocardiography Evaluation

Echocardiography studies were completed within 3 hours of MRI studies for each subject using similar supine subject positioning. For one subject, there was a 2 week delay between MRI and echocardiography studies. Two-dimensional transthoracic ultrasound (Vivid i; GE Healthcare Clinical Systems, Wauwatosa, USA) was used to image the motion of the LV base and mitral valve during IVR using frame rates of 60–90 Hz. Cines in the apical 4-chamber, 3-chamber and parasternal long-axis image orientations were acquired for each subject. Subjects were instructed to hold their breath at end-expiration for all image acquisitions, similar to MRI studies.

2.2.3 Data Analysis

All data were analyzed offline (MATLAB; MathWorks, Natick, USA). Aortic valve closure (AVC) and mitral valve opening (MVO) times were estimated using through-plane phase contrast blood velocity maps of a short-axis slice intersecting or near the mitral and aortic valve planes. Phase contrast images were temporally interpolated to 10 ms per frame using piecewise cubic-

spline interpolation. Blood-velocity data were used to estimate AVC and MVO times by extrapolating the velocity-time curves to their baseline or no-flow condition for the valve, as illustrated in Figure 2.2. The baseline blood-velocity value at the aortic valve was assumed to be zero, reflecting no flow at the time of aortic valve closure, while a small non-zero baseline velocity was routinely indentified at the mitral valve.

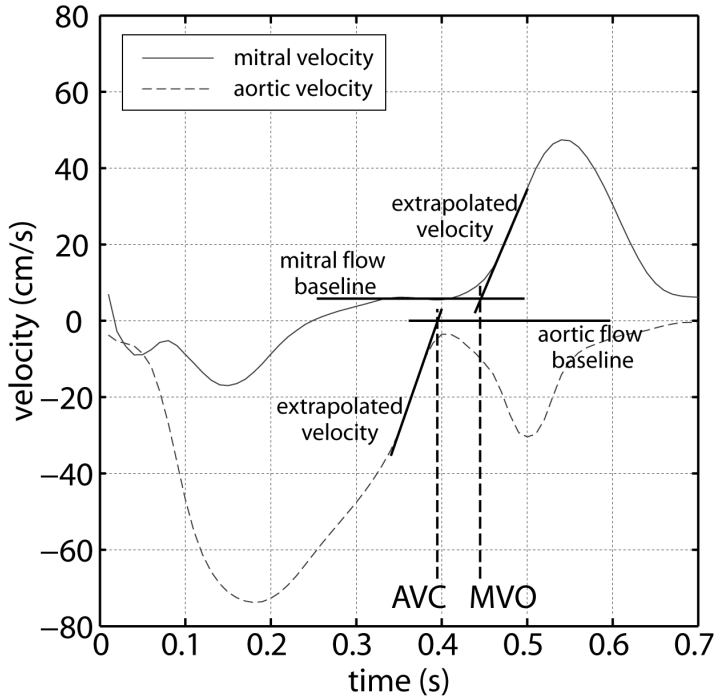

Figure 2.2: Determination of AVC and MVO times. The intersection of extrapolated aortic and mitral flow velocities and their respective baseline (no-flow) values indicate AVC and MVO times, respectively.

LV volume was determined by the method of disks (disk summation) using the short-axis stack of SSFP images according to Simpson's rule [11, 21, 22]. Endocardial and epicardial contours were manually traced on the short-axis stack, and papillary muscles and trabeculae were included as part of the LV lumen as shown in Figure 2.1. The inclusion or exclusion of basal slices has been described as the major source of error in volumes measured using MRI [22]. To address this issue, long-axis images were used to identify the base and

apex of the LV (Figure 2.1), allowing for the fractional inclusion or extension of slices, similar to previously used techniques [28, 29]. An identical method was used in a previous study to determine end-systolic and end-diastolic volumes and yielded inter-observer and intra-observer variabilities based on the coefficient of variation (COV) of 2.6% and 2.1%, respectively [30]. Early diastolic volume-time curves were generated by determining volume for all cardiac phases from AVC to the end of early filling.

Myocardial tissue deformation was assessed by tracking material points on the LV myocardium using tagged cines. An example of tracked points between 2 cardiac phases is shown in Figure 2.3. Long-axis linear tags were manually tracked and used to assess E_{ll}, while short-axis grid tags were tracked using an image-morphing technique and used to assess E_{cc}, E_{rr}, and untwisting. Analysis of short-axis grid tags using image morphing was performed using custom software similar to previously published methods [16, 30, 31]. The spatial positions of each tracked point for both short-axis grid and long-axis linear tags were interpolated in time, using piecewise cubic-spline interpolation, to a uniform temporal resolution of 10 ms (from the true acquired temporal resolution of 23 ms). Inter-observer and intra-observer reproducibility for the study population were measured in terms of the COV for the parameters measured using the image morphing technique, E_{cc}, E_{rr} and untwisting.

Strain as a function of time was calculated using the change in length of a tissue segment at a given time relative to its reference length at diastasis divided by this reference length, in circumferential, longitudinal, and radial directions. Tissue lengths are defined as the distance between adjacent points in the circumferential and longitudinal directions, and as the difference between distances from the LV centroid to adjacent points in the radial direction. For circumferential and longitudinal directions, both global and endocardial strains

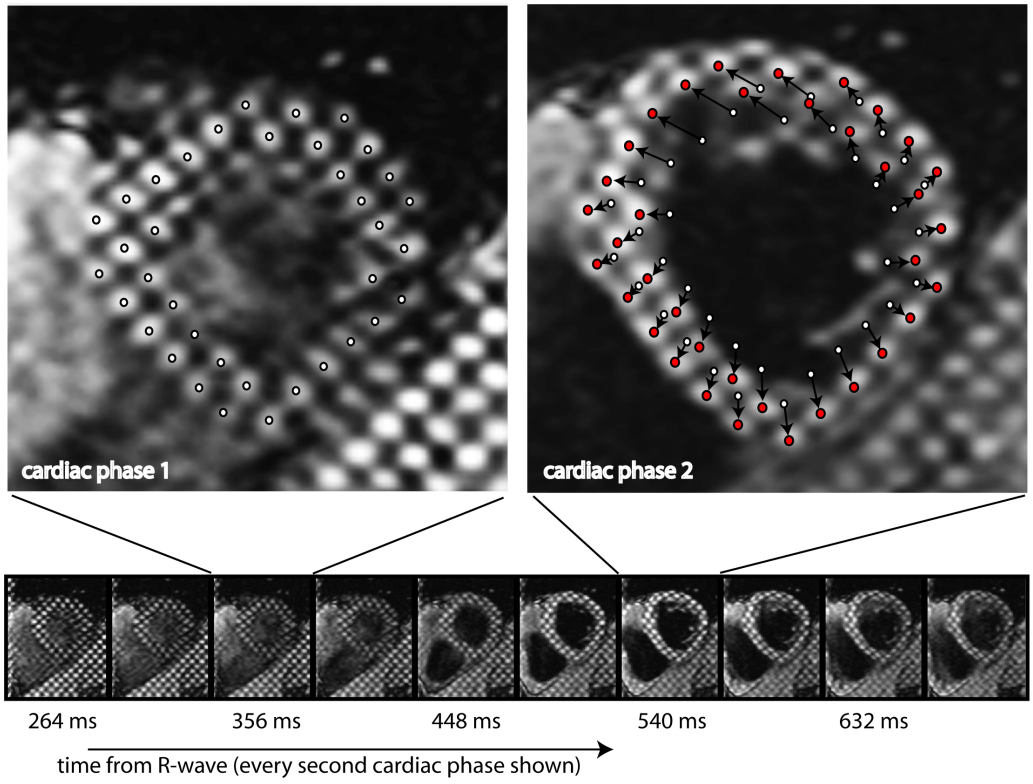

Figure 2.3: Short-axis grid tagging. The images on the bottom show every second acquired image between 264 ms and 654 ms from the ECG R-wave. The two enlarged images (cardiac phase 1 and cardiac phase 2) demonstrate the tracking of points over time. White circles indicate the position of tissue at cardiac phase 1 and red circles indicate the position of the same tissue at cardiac phase 2. Arrows indicate the movement of the tissue calculated using deformation fields from image-morphing.

were measured; for the radial direction, only global strain was measured. Endocardial strains were calculated for the purpose of comparison with changes in LV volumes. The rate of change of strain ($\dot{E}$) was calculated as the discrete time derivative of the strain-time curve.

LV twist was calculated similarly to previous studies as the difference in rotations between the base and apex taking into account the moving centroid of the LV mass at each cardiac phase [17, 20]. A cardiac phase at diastasis was selected as the reference for the calculation of all rotation angles [32]. The rate of untwist was calculated as the negative discrete time derivative of the

twist-time curve.

In order to directly compare measured changes in strain during the isovolumic interval to corresponding changes in LV volume, the LV was modeled as half of an ellipsoid, symmetric about the LV long-axis [23]. The volume of a half ellipsoid is:

$$V_e = \frac{1}{2}\left[\frac{4}{3}\pi a b^2\right] \tag{2.1}$$

where a is the length of the LV long-axis and b is the radius of the LV short-axis at the base. To determine the initial dimensions of the ellipsoid, the end-systolic volume (ESV) and the eccentricity (Γ, the ratio of the LV width to length) of the LV at end-systole were used. ESV was directly measured using disk summation of short-axis images and eccentricity was measured from 4-chamber long-axis images. Next, these values (V_e = ESV and $\Gamma = a/b$) were substituted into Equation 2.1, and a and b were solved for. Subsequent changes in ellipsoid dimensions were estimated from measured endocardial strains, where $E_{cc_{endo}}$ defines changes in the LV short-axis radius, b, and $E_{ll_{endo}}$ defines changes in the LV long-axis length, a. Using Equation 2.1, changes in these dimensions were used to estimate changes in LV volume associated with changes in $E_{cc_{endo}}$ and $E_{ll_{endo}}$. Endocardial strains were used because they correspond to the boundary of the LV cavity.

Long-axis cardiac ultrasound images were used to observe the changes in shape of the mitral valve leaflets during IVR. The deformation was measured in 2 ways using apical 4-chamber, 3-chamber and parasternal long-axis views of the heart. Firstly, the mitral valve leaflet was manually traced at the frame closest to AVC and immediately prior to MVO. Secondly, the shortest distance between the leaflet tips and a line intersecting the hinge points of the valve at AVC and MVO were measured to represent a quantitative measure of leaflet deformation.

2.2.4 Representation of Data and Statistical Analysis

All calculated parameters, including LV volume, twist, rate of untwist, strains and strain rates are represented as continuous time variables. These time-courses are shown as representative curves produced by the average of the 10 subjects with the standard deviation indicated by error bars. The error bars are plotted at regular time intervals for clarity and do not represent actual measurement times. When single values are quoted, they represent either peak-positive values, peak-negative values or changes over specified time intervals. The timings of events were all normalized to AVC and expressed as either % of systolic duration or ms from AVC.

Statistical analysis was performed using Microsoft Office Excel 2007 (Microsoft Corporation, Redmond, USA). Values are stated as mean ± standard deviation and statistical significance was set at $p < 0.05$. Paired Student's t-tests were applied to test for differences in LV volume, strain and twist measured between AVC and MVO times. Pearson's product-moment correlations and partial correlations which control for time were applied to represent the relationships between LV volume and other measured parameters (twist, E_{cc}, E_{ll}, E_{rr}, $E_{cc_{endo}}$ and $E_{ll_{endo}}$) during IVR depending on time and independent of time, respectively. To extract the correlational data, volume-time curves for each subject were referenced to their values at AVC and sampled every 10 ms, starting from 5 ms after AVC up to MVO, resulting in a series of discrete volume data. Corresponding data were also extracted for twist, global strains and endocardial strains and were correlated with volume. Inter-observer and intra-observer reproducibility were calculated using the coefficient of variation.

2.3 Results

Study population characteristics were measured as follows: 55 ± 6 bpm heart rate, 117 ± 9 mmHg systolic blood pressure, 70 ± 6 mmHg diastolic blood pressure, 196 ± 32 ml end-diastolic LV volume, 77 ± 14 ml end-systolic LV volume, 119 ± 20 ml stroke volume, $61 \pm 3\%$ ejection fraction (EF), and 114 ± 21 g LV mass.

Time-courses of LV volume, global strain and twist, and their respective rates of change, are plotted in Figure 2.4. Peak values for all parameters and their timings along with the timings of other significant events are shown in Table 2.1. The observed sequence of events in all subjects was: (1) peak twist and strains (minimum E_{cc} and E_{ll} and maximum E_{rr}) occurred at end-systole, near AVC, (2) MVO occurred at 58 ± 10 ms after AVC ($117 \pm 3\%$ of systole), (3) the peak rate of untwist occurred at 68 ± 25 ms after AVC ($120 \pm 8\%$ of systole), and finally (4) the peak $\dot{E}_{cc}$, $\dot{E}_{ll}$ and $\dot{E}_{rr}$ occurred at 152 ± 21 ms, 159 ± 19 ms, and 138 ± 27 ms after AVC, respectively ($145 \pm 7\%$, $147 \pm 7\%$, and $141 \pm 9\%$ of systole).

Table 2.2 summarizes the changes measured in all parameters during the IVR interval. These IVR changes are also expressed as a percentage of the total change over early filling. LV volume underwent an apparent increase of 5 ± 2 ml and E_{cc}, E_{ll} and E_{rr} changed significantly during IVR, with all changes in strain promoting an increase in volume. The averaged time-courses for volume, twist, and strain rates over the IVR interval are shown in Figure 2.5. The strain-estimated volume change (3 ± 2 ml) using Equation 2.1 was significantly smaller ($p < 0.01$) than the direct assessment of volume change, but the volume changes were significantly correlated ($R = 0.83$, $p < 0.001$), as shown in Figure 2.6F. Similar comparisons were made between changes

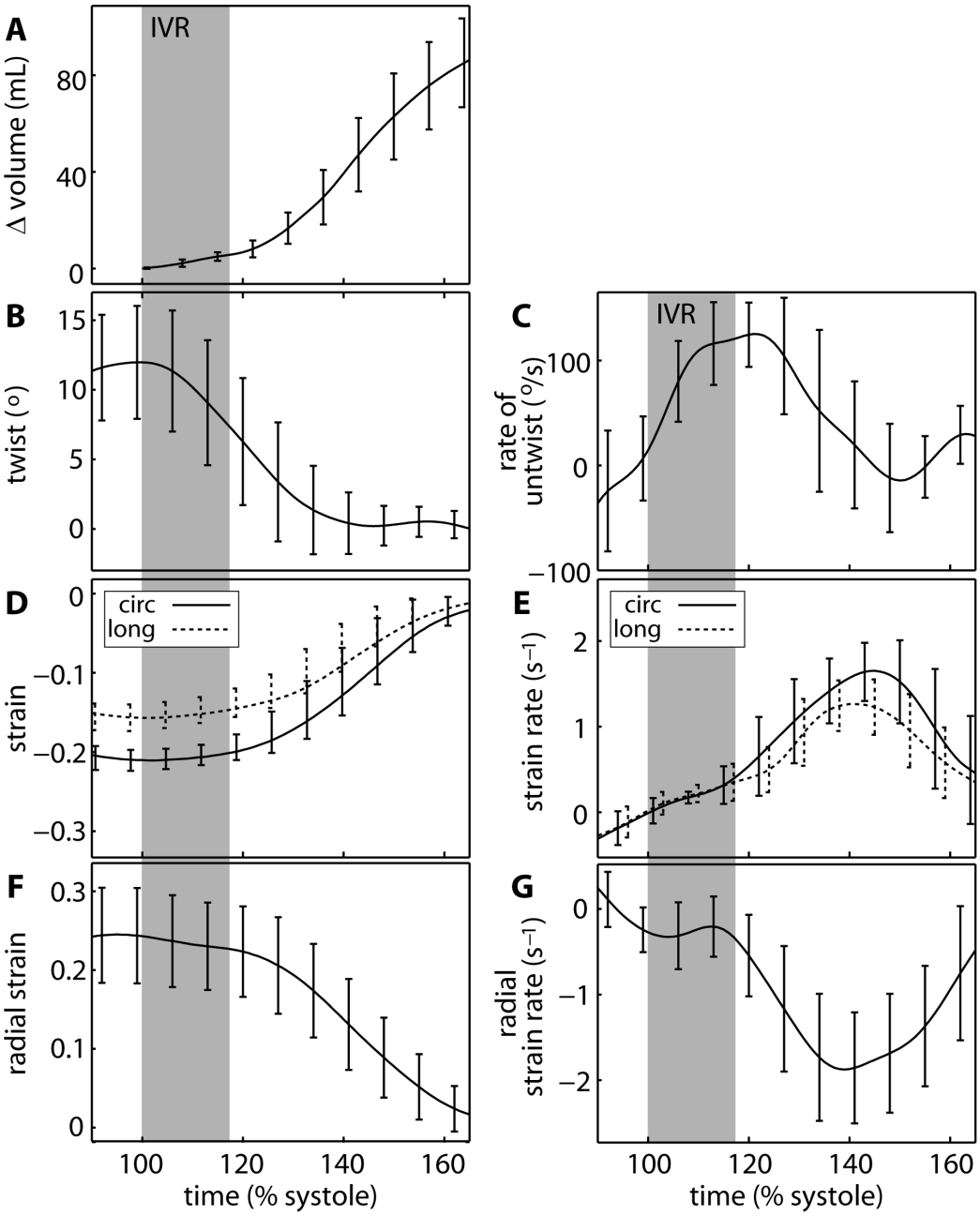

Figure 2.4: Time-courses of volume change, twist, rate of untwist, strain and strain rate.

Table 2.1: Peak values and rates of strain and twist throughout early diastole

		Time	
	Peak value	% systole	ms
AVC	—	100	0
MVO	—	117 ± 3	58 ± 10
E_{cc}			
Peak systolic global, $\times 10^{-2}$	-21 ± 1	100 ± 5	0 ± 18
Peak systolic endocardial, $\times 10^{-2}$	-25 ± 2	100 ± 6	0 ± 20
$\dot{E}_{cc}$			
Peak diastolic global, s^{-1}	1.9 ± 0.2	145 ± 7	152 ± 21
Peak diastolic endocardial, s^{-1}	2.2 ± 0.3	145 ± 7	152 ± 20
E_{ll}			
Peak systolic global, $\times 10^{-2}$	-16 ± 2	100 ± 4	-1 ± 15
Peak systolic endocardial, $\times 10^{-2}$	-17 ± 2	101 ± 6	4 ± 19
$\dot{E}_{ll}$			
Peak diastolic global, s^{-1}	2.9 ± 0.3	147 ± 7	159 ± 19
Peak diastolic endocardial, s^{-1}	1.6 ± 0.2	143 ± 7	143 ± 18
E_{rr}			
Peak systolic global, $\times 10^{-2}$	25 ± 6	98 ± 11	-6 ± 34
$\dot{E}_{rr}$			
Peak diastolic global, s^{-1}	-2.3 ± 0.5	141 ± 9	138 ± 27
Twist			
Peak systolic, $^\circ$	12 ± 4	98 ± 5	-6 ± 18
Untwisting rate			
Peak diastolice, $^\circ/s$	154 ± 35	120 ± 8	68 ± 25

All values are mean ± standard deviation.

in measured LV volume and the changes in all strain components and with untwisting (Figure 2.6). Table 2.3 summarizes the correlations between the apparent volume changes and other parameters, both as direct comparisons and also as partial correlations, controlling for time from AVC to correct for correlations due to similar time-courses of volume and strain changes. The linear correlations between LV volume changes and changes in all other parameters were statistically significant ($p < 0.01$).

Using cardiac ultrasound, the leaflets were observed to deform towards the LV interior prior to their separation in all subjects, as shown in Figure 2.7. The solid lines correspond to the leaflet position at aortic valve closure and the dashed lines to their position prior to mitral valve opening. A typical example for a parasternal long-axis view tracing is also shown in Figure 2.7. The displacement of the mitral leaflet tips during IVR was 6.0 ± 3.3 mm, 5.1 ± 2.4 mm and 2.1 ± 5.0 mm for apical 4-chamber, 3-chamber and parasternal long-axis views, respectively. These displacements were not found to correlate with IVR changes in measured LV volume or components of myocardial strain.

Inter-observer and intra-observer reproducibility in terms of COV for the image morphing technique used to calculate E_{cc}, E_{rr} and untwisting is shown in Table 2.4. Reproducibility is shown for the following key parameters: peak end-systolic E_{cc} and E_{rr}, peak diastolic $\dot{E}_{cc}$ and $\dot{E}_{rr}$, peak end-systolic twist, and peak diastolic untwisting rate. The reproducibility of the timings of these key parameters is also shown.

2.4 Discussion

The major new findings of this study are: (1) MRI-derived measures of LV volume increase significantly during the IVR interval, and (2) changes

Table 2.2: Measured changes during isovolumic relaxation

	AVC	MVO	Δ	p
Volume				
ml	69 ± 13	74 ± 13	5 ± 2	< 0.001
% of early filling	—	—	5 ± 2	< 0.001
Strain-estimated, ml	—	—	3 ± 2	< 0.01
E_{cc} global				
$\times 10^{-3}$	-211 ± 14	-202 ± 16	9 ± 6	< 0.01
% of peak	—	—	4 ± 3	< 0.01
E_{cc} endocaridal				
$\times 10^{-3}$	-247 ± 20	-237 ± 22	10 ± 7	< 0.01
% of peak	—	—	4 ± 3	< 0.01
E_{ll} global				
$\times 10^{-3}$	-157 ± 18	-148 ± 17	9 ± 6	< 0.001
% of peak	—	—	6 ± 3	< 0.001
E_{ll} endocaridal				
$\times 10^{-3}$	-167 ± 20	-158 ± 22	8 ± 8	< 0.01
% of peak	—	—	$5\pm$	< 0.01
E_{rr} global				
$\times 10^{-3}$	243 ± 64	229 ± 57	-15 ± 17	< 0.05
% of peak	—	—	5 ± 8	0.05
Twist				
$^\circ$	12 ± 4	7 ± 5	-5 ± 2	< 0.001
% of peak	—	—	37 ± 18	< 0.001

Δ = change between AVC and MVO. Values are mean $\pm$ standard deviation.

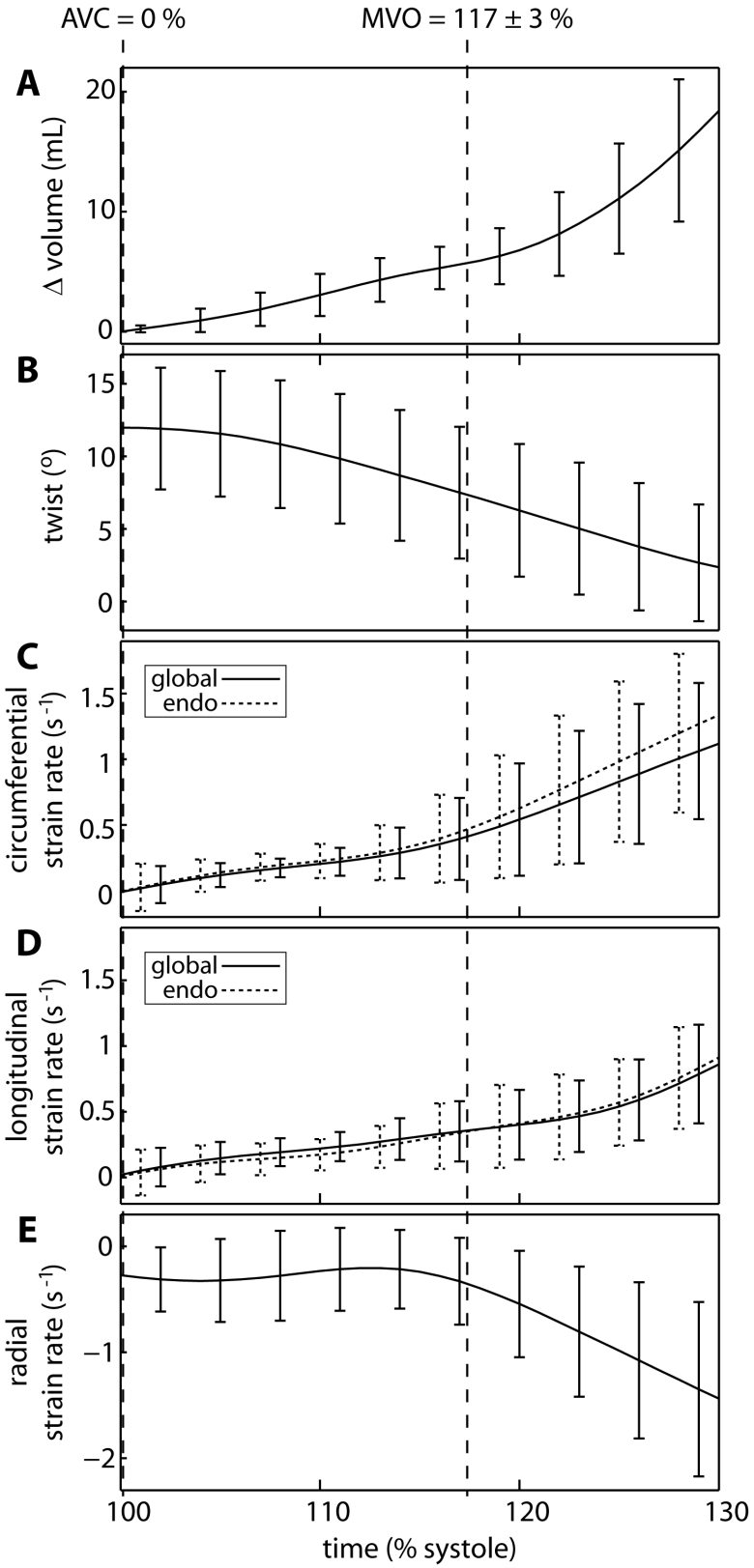

Figure 2.5: Volume change, twist and strain rate during IVR.

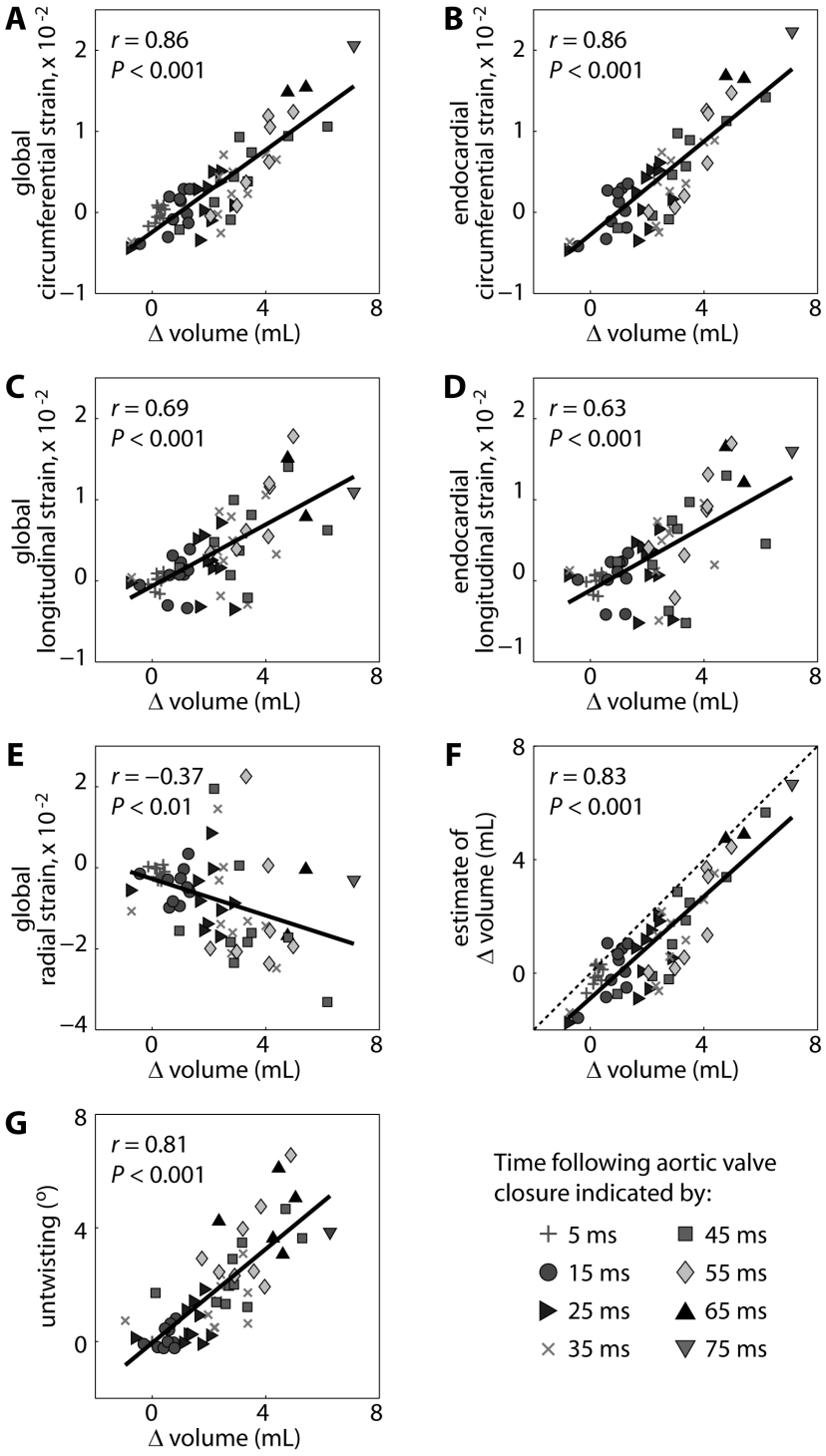

Figure 2.6: Correlations of strain, volume estimated from strain and untwisting with volume change.

Table 2.3: Correlations with LV volume change during IVR

	Correlation		Partial correlation	
	R	p	R	p
E_{cc}				
Global	0.86	< 0.001	0.72	< 0.001
Endocardial	0.86	< 0.001	0.75	< 0.001
E_{ll}				
Global	0.69	< 0.001	0.33	< 0.01
Endocardial	0.63	< 0.001	0.29	< 0.05
E_{rr}				
Global	-0.37	< 0.01	-0.22	0.09
Volume				
Strain-estimated	0.83	< 0.001	0.69	< 0.001
Untwisting	0.81	< 0.001	0.41	< 0.01

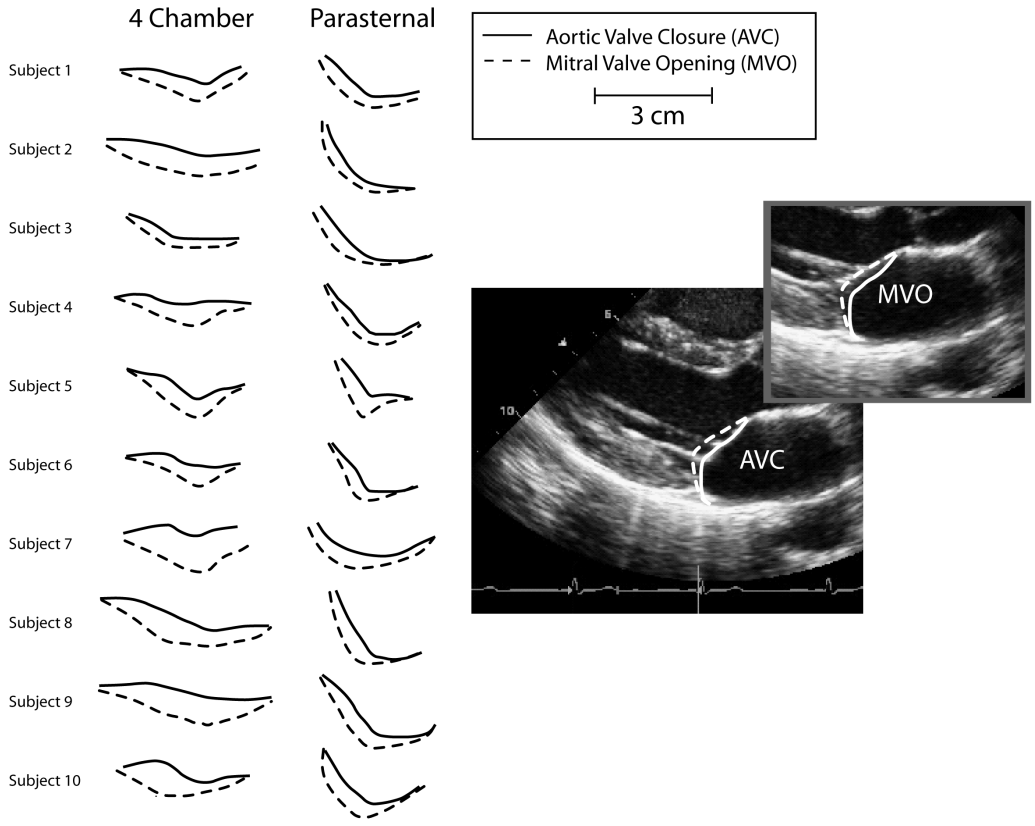

Figure 2.7: Mitral leaflet position at AVC and MVO. The apical four-chamber and parasternal long-axis views for each of the ten subjects were analyzed. An example of the valve tracings is shown on the right for a parasternal view.

Table 2.4: Reproducibility of strain and twist using grid tagging

	Inter-observer		Intra-observer	
	Variability	COV	Variability	COV
E_{cc} global				
Peak systolic, $\times 10^{-2}$	1.2	6.1%	0.5	2.8%
Time of peak, ms	6.7	—	6.9	—
$\dot{E}_{cc}$ global				
Peak diastolic, s^{-1}	0.10	6.1%	0.07	4.5%
Time of peak, ms	4.6	—	2.7	—
E_{rr} global				
Peak systolic, $\times 10^{-2}$	4.4	15.7%	2.0	6.6%
Time of peak, ms	8.7	—	7.2	—
$\dot{E}_{rr}$ global				
Peak diastolic, s^{-1}	0.48	21.1%	0.32	13.1%
Time of peak, ms	33.3	—	17.6	—
Twist				
Peak systolic, $^\circ$	0.9	7.9%	1.1	9.6%
Time of peak, ms	6.3	—	3.5	—
Untwisting rate				
Peak diastolic, $^\circ$/s	12	8.7%	11	8.1%
Time of peak, ms	16.2	—	8.7	—

Variability refers to the standard deviation of the differences between the 2 sets of measurements. COV is the variability normalized to the mean of the 2 sets of measurements and is not reported for the timings of events.

in measured LV volume over the IVR interval are significantly correlated with the changes in circumferential, longitudinal, and radial strain and with the extent of untwisting.

These findings support our hypothesis that imaging-derived volume increases measured during IVR are a consequence of myocardial expansion associated with increased fiber lengths during relaxation. The apparent increase in LV volume results from the measurement method which excludes the complex boundaries defined by the closed mitral and aortic leaflets. Thus, apparent LV volume changes can be viewed as representing regional changes in geometry, reflecting measurements being performed on the myocardium but not the valve leaflets. The measured myocardial expansion is thus likely balanced by the inward bowing of the mitral leaflets during this interval. The stiffness of the leaflets themselves has been shown to be actively modulated and to vary as a function of cardiac phase; stiffness is lower during IVR than during isovolumic contraction [33]. Thus the change in measured volume may be modulated by the material and functional properties of the mitral leaflets in conjunction with the relaxation properties of the LV.

2.4.1 Strain versus Volume During IVR

The measured volume increase during IVR, which neglects the inward deformation of the mitral leaflets, represents the overall expansion of the LV chamber and would be expected to correspond to the overall changes in tissue strains, lengthening in the circumferential and longitudinal directions and thinning in the radial direction. Overall, the changes in E_{cc} and $E_{cc_{endo}}$ were best correlated with the volume changes ($R_{circ_{global}} = 0.86$, $R_{circ_{endo}} = 0.86$, $p < 0.001$). E_{ll} changes were less well correlated with the changes in volume ($R_{long_{global}} = 0.69$, $R_{long_{endo}} = 0.63$, $p < 0.001$) and the change in E_{rr} was

least well correlated ($R_{radial} = -0.37$, $p < 0.01$). The trends in these results are not surprising given their respective relationships with LV chamber volume. As indicated by the ellipsoid model used in this study, volume is linearly proportional to the long-axis length but is dependent on the square of the short-axis radius or, equivalently, the circumference (Equation 2.1). Thus a given change in E_{cc} will give rise to approximately double the change in LV volume (for small changes in strain) as compared to the same change in E_{ll}. The changes in E_{rr}, unlike E_{cc} or E_{ll}, are indirectly related to LV volume changes due to its dependence on both the endocardial and epicardial borders. The volume-strain correlational data in Figure 2.6 illustrate the relative strengths of these correlations. Changes in the amount of untwist were also highly correlated with volume changes ($R_{untwist} = 0.81$, $p < 0.001$). This relationship would not necessarily be expected because LV untwisting alone does not necessitate a volume change. However, when time from AVC was controlled for, this partial correlation coefficient was significantly reduced ($R_{untwist} = 0.41$, $p < 0.01$) while the partial correlation coefficient for circumferential strain was only slightly reduced with the same correction ($R_{circ_{endo}} = 0.75$, $p < 0.001$). Thus, the amount of co-variation between measured changes in LV volume and untwisting may be attributed largely to their correlations with time; conversely, the co-variation between measured changes in LV volume and changes in E_{cc} is largely independent of their correlations with time. Finally, volume changes estimated using the changes in $E_{cc_{endo}}$ and $E_{ll_{endo}}$ using Equation 2.1 yielded significantly lower volumes than direct measurement (3 ± 2 ml versus 5 ± 2 ml, $p < 0.01$) but these were still significantly correlated ($R_{vol.\,est.} = 0.83$, $p < 0.001$). This volume estimate is dominated by the circumferential strain component, as indicated in Equation 2.1, and we would thus propose that global E_{cc} is the most practical surrogate for changes in LV volume represent-

ing the expansion of the myocardium during IVR.

Isovolumic changes in global E_{cc}, E_{ll} and E_{rr} have been measured using speckle tracking echocardiography [13, 14]. Specifically, Wang et al. measured a correlation between global longitudinal strain rate during IVR and the time constant of isovolumic LV pressure decline (τ). In their study, $\dot{E}_{ll}$ was proposed to reflect the expansion of the myocardium associated with relaxation. Our current study confirms this supposition and further suggests that E_{cc} would be most representative of LV volume expansion associated with relaxation. Wang et al. concluded that isovolumic $\dot{E}_{ll}$ reflects LV relaxation because the data is acquired during IVR, while the mitral valve is closed, isolating it from the effects of left atrial pressure. However, the current study illustrates that while the mitral leaflets are closed, they likely change their shape in conjunction with volume and strain changes. Thus the material properties of the leaflets and the atrial pressure would modulate the changes in strain during IVR in addition to LV relaxation.

2.4.2 Mitral Leaflet Motion during IVR

The inward displacement of the leaflets towards the LV cavity was measurable in all subjects (Figure 2.7) in all views and offers a source of blood displacement that can account for changes in tissue strain and apparent LV volume increases during IVR. This observed leaflet deformation is similar to previous studies of mitral valve function in isolated swine hearts [34] and in-vivo ovine hearts [35]. These studies concluded that the mitral leaflets descend into the LV throughout IVR, prior to the separation of the leaflets. However, the displacement of the valve leaflets in our study did not correlate with measured changes in volume. This may be due to the complex shape of the mitral leaflets; in other words, a 1-dimensional measure of leaflet displacement may

not be representative of the 3-dimensional shape deformation. Additionally, it was not possible to quantify the volumetric displacement of the mitral valve leaflets during IVR using 2-dimensional long-axis cardiac ultrasound images. However, a coarse estimation of the volume change can be made using the average displacements and annular radii. The base to apex displacement obtained by averaging the values measured in the different views is 0.43 cm. If a representative annular radius of 1.5 cm is assumed (estimated from Figure 2.7) this results in a mitral valve area of approximately 7 cm^2. When this area is multiplied by the average displacement, a volume of approximately 3 ml is obtained, similar to the volume change of 3 ± 2 ml predicted by the strain assessment. It is possible that 3-dimensional echocardiographic imaging of the mitral leaflets at aortic valve closure and mitral valve opening could be used to provide a direct assessment of the apparent change in LV volume measured during isovolumic relaxation.

2.4.3 Limitations

When interpreting results from this study, it is important to consider the limitations of the imaging modalities used. Conventional cine MRI does not clearly resolve the aortic and mitral leaflets or their motion over time with sufficient resolution to identify aortic valve closure and mitral valve opening times. We approximated these times from blood velocity-time curves measured near the aortic leaflet plane and at the mitral leaflet tips using the method illustrated in Figure 2.2. Using this approach, the timing of key events such as peak twist (at $98 \pm 5\%$ of systole) and strains (minimum E_{cc} and E_{ll} at $100 \pm 5\%$ and $102 \pm 7\%$, respectively, and maximum E_{rr} at $98 \pm 11\%$) were shown to be near the time of aortic valve closure in agreement with numerous other studies [13, 14, 16–20, 30, 36]. Also, the IVR duration (58 ± 10 ms in

the current study), is consistent with echocardiography guidelines for normal hearts in our subjects' age range [37]. The time of peak untwisting rate at $120 \pm 8\%$ of systole is also in agreement with literature value for healthy subjects [18, 30, 36]. Finally, the percentage of untwisting at the time of mitral valve opening was measured to be 36.6%, which is in good agreement with previous echocardiography studies [16, 18, 19]. While all subjects did have a cardiac ultrasound evaluation, it was determined that the valve opening and closure times from these studies would not be accurate for use in analysis of the MRI studies due to potential differences in heart rate and loading conditions. Conversely, MRI evaluation of the valve timings occurred within 10 minutes of all other MRI data acquisition and under identical subject positioning and physiologic conditions.

While MRI has the advantage of being highly reproducible for the quantification of LV volume [21], it has the disadvantage of having lower temporal resolution compared to echocardiography. Thus, a potential explanation for the larger volume changes measured from direct volumetric analysis (5 ± 2 ml), as compared to the strain analysis (3 ± 2 ml), is the lower temporal resolution of the volumetric cine images, which could blur the larger changes in volume during early filling into the isovolumic period and lead to an overestimation of the apparent volume change. Nonetheless, the tissue tagging methods used for strain measures were acquired and analyzed independently of volume measurements with a higher temporal resolution and were significantly correlated with the volume data independently of their temporal correlations. This suggests that the apparent volume changes do represent the expansion of the LV myocardium during the isovolumic interval.

The interpretation of changes in strain, volume or leaflet position over the IVR interval detailed in this study assumes that both aortic and mitral

valves do not leak during this interval, meaning that volume contained between mitral and aortic valves is constant while valves are closed during IVR. Changes in any of the measured metrics with a leak present in either valve during this interval thus cannot be interpreted in the context of LV relaxation or mitral leaflet motion alone.

2.4.4 Conclusions

While closed mitral and aortic valves ensure true isovolumic conditions during IVR, circumferential and longitudinal stretching and radial thinning during this interval contribute to a change in LV shape which can be measured as an increase in apparent LV volume prior to mitral valve opening. Changes in global circumferential strain were the most representative of this apparent volume change. The observed inward motion (towards the apex) of the mitral leaflets allows for the conservation of volume. The leaflet motion and the conformational changes in the LV during isovolumic relaxation likely reflect active relaxation, LV pressure decline, and the material properties of mitral leaflets.

2.5 Chapter 2 References

[1] Bove AA. Radiographic evaluation of dynamic geometry of the left ventricle. *J Appl Physiol*, 31:227–34, 1971.

[2] Hawthorne EW. Instantaneous dimensional changes of the left ventricle in dogs. *Circ Res*, 9:110–9, 1961.

[3] Rushmer RF. Pressure-circumference relations of left ventricle. *Am J Physiol*, 186:115–21, 1956.

[4] Goetz WA, Lansac E, Lim HS, Weber PA, and Duran CM. Left ventricular endocardial longitudinal and transverse changes during isovolumic contraction and relaxation: a challenge. *Am J Physiol Heart Circ Physiol*, 289:H196–201, 2005.

[5] Altieri PI, Wilt SM, and Leighton RF. Left ventricular wall motion during the isovolumic relaxation period. *Circulation*, 48:499–505, 1973.

[6] Ruttley MS, Adams DF, Cohn PF, and Abrams HL. Shape and volume changes during "isovolumetric relaxation" in normal and asynergic ventricles. *Circulation*, 50:306–16, 1974.

[7] Bonow RO, Vitale DF, Bacharach SL, Frederick TM, Kent KM, and Green MV. Asynchronous left ventricular regional function and impaired global diastolic filling in patients with coronary artery disease: reversal after coronary angioplasty. *Circulation*, 71:297–307, 1985.

[8] Bowman AW, Frihauf PA, and Kovcs SJ. Time-varying effective mitral valve area: prediction and validation using cardiac MRI and Doppler

echocardiography in normal subjects. *Am J Physiol Heart Circ Physiol*, 287:H1650–7, 2004.

[9] Cuocolo A, Sax FL, Brush JE, Maron BJ, Bacharach SL, and Bonow RO. Left ventricular hypertrophy and impaired diastolic filling in essential hypertension. Diastolic mechanisms for systolic dysfunction during exercise. *Circulation*, 81:978–86, 1990.

[10] Flewitt JA, Hobson TN, Wang J Jr, Johnston CR, Shrive NG, Belenkie I, Parker KH, and Tyberg JV. Wave intensity analysis of left ventricular filling: application of windkessel theory. *Am J Physiol Heart Circ Physiol*, 292:H2817–23, 2007.

[11] Soldo SJ, Norris SL, Gober JR, Haywood LJ, Colletti PM, and Terk M. MRI-derived ventricular volume curves for the assessment of left ventricular function. *Magn Reson Imaging*, 12:711–7, 1994.

[12] Zeidan Z, Erbel R, Barkhausen J, Hunold P, Bartel T, and Buck T. Analysis of global systolic and diastolic left ventricular performance using volume-time curves by real-time three-dimensional echocardiography. *J Am Soc Echocardiogr*, 16:29–37, 2003.

[13] Nottin S, Doucende G, Schuster-Beck I, Dauzat M, and Obert P. Alteration in left ventricular normal and shear strains evaluated by 2D-strain echocardiography in the athlete's heart. *J Physiol*, 586:4721–33, 2008.

[14] Wang J, Khoury DS, Thohan V, Torre-Amione G, and Nagueh SF. Global diastolic strain rate for the assessment of left ventricular relaxation and filling pressures. *Circulation*, 115:1376–83, 2007.

[15] Dong SJ, Hees PS, Siu CO, Weiss JL, and Shapiro EP. MRI assessment

of LV relaxation by untwisting rate: a new isovolumic phase measure of tau. *Am J Physiol Heart Circ Physiol*, 281:H2002–9, 2001.

[16] Esch BT, Scott JM, Warburton DE, Thompson R, Taylor D, Cheng Baron J, Paterson I, and Haykowsky MJ. Left ventricular torsion and untwisting during exercise in heart transplant recipients. *J Physiol*, 587:2375–86, 2009.

[17] Notomi Y, Lysyansky P, Setser RM, Shiota T, Popovic ZB, Martin-Miklovic MG, Weaver JA, Oryszak SJ, Greenberg NL, White RD, and Thomas JD. Measurement of ventricular torsion by two-dimensional ultrasound speckle tracking imaging. *J Am Coll Cardiol*, 45:2034–41, 2005.

[18] Notomi Y, Martin-Miklovic MG, Oryszak SJ, Shiota T, Deserranno D, Popovic ZB, Garcia MJ, Greenberg NL, and Thomas JD. Enhanced ventricular untwisting during exercise: a mechanistic manifestation of elastic recoil described by Doppler tissue imaging. *Circulation*, 113:2524–4533, 2006.

[19] Rademakers FE, Buchalter MB, Rogers WJ, Zerhouni EA, Weisfeldt ML, Weiss JL, and Shapiro EP. Dissociation between left ventricular untwisting and filling. Accentuation by catecholamines. *Circulation*, 85:1572–81, 1992.

[20] Stuber M, Scheidegger MB, Fischer SE, Nagel E, Steinemann F, Hess OM, and Boesiger P. Alterations in the local myocardial motion pattern in patients suffering from pressure overload due to aortic stenosis. *Circulation*, 100:361–8, 1999.

[21] Bellenger NG, Davies LC, Francis JM, Coats AJ, and Pennell DJ. Reduction in sample size for studies of remodeling in heart failure by the use

of cardiovascular magnetic resonance. *Cardiovasc Magn Reson*, 2:271–8, 2000.

[22] Pennell DJ. Ventricular volume and mass by CMR. *J Cardiovasc Magn Reson*, 4:507–13, 2002.

[23] Parisi AF, Moynihan PF, Feldman CL, and Folland ED. Approaches to determination of left ventricular volume and ejection fraction by real-time two-dimensional echocardiography. *Clin Cardiol*, 2:257–63, 1979.

[24] Amundsen BH, Crosby J, Steen PA, Torp H, Slrdahl SA, and Stylen A. Regional myocardial long-axis strain and strain rate measured by different tissue Doppler and speckle tracking echocardiography methods: a comparison with tagged magnetic resonance imaging. *Eur J Echocardiogr*, 10:229–37, 2009.

[25] Amundsen BH, Helle-Valle T, Edvardsen T, Torp H, Crosby J, Lyseggen E, Stylen A, Ihlen H, Lima JA, Smiseth OA, and Slrdahl SA. Noninvasive myocardial strain measurement by speckle tracking echocardiography: validation against sonomicrometry and tagged magnetic resonance imaging. *J Am Coll Cardiol*, 47:789–93, 2006.

[26] Goffinet C, Chenot F, Robert A, Pouleur AC, le Polain de Waroux JB, Vancrayenest D, Gerard O, Pasquet A, Gerber BL, and Vanoverschelde JL. Assessment of subendocardial vs. subepicardial left ventricular rotation and twist using two-dimensional speckle tracking echocardiography: comparison with tagged cardiac magnetic resonance. *Eur Heart J*, 30:608–17, 2009.

[27] Helle-Valle T, Crosby J, Edvardsen T, Lyseggen E, Amundsen BH, Smith HJ, Rosen BD, Lima JA, Torp H, Ihlen H, and Smiseth OA. New nonin-

vasive method for assessment of left ventricular rotation: speckle tracking echocardiography. *Circulation*, 112:3149–56, 2005.

[28] Kirschbaum SW, Baks T, Gronenschild EH, Aben JP, Weustink AC, Wielopolski PA, Krestin GP, de Feyter PJ, and van Geuns RJ. Addition of the long-axis information to short-axis contours reduces interstudy variability of left-ventricular analysis in cardiac magnetic resonance studies. *Invest Radiol*, 43:1–6, 2008.

[29] Thunberg P, Emilsson K, Rask P, and Khri A. Separating the left cardiac ventricle from the atrium in short axis MR images using the equation of the atrioventricular plane. *Clin Physiol Funct Imaging*, 28:222–8, 2008.

[30] Nelson MD, Haykowsky MJ, Petersen SR, Delorey DS, Cheng-Baron J, and Thompson RB. Increased left ventricular twist, untwisting rates and suction maintain global diastolic function during passive heat stress in humans. *Am J Physiol Heart Circ Physiol*, 298:H930–7, 2010.

[31] Ledesma-Carbayo MJ, Derbyshire JA, Sampath S, Santos A, Desco M, and McVeigh ER. Unsupervised estimation of myocardial displacement from tagged MR sequences using nonrigid registration. *Magn Reson Med*, 59:181–9, 2008.

[32] Dorfman TA, Rosen BD, Perhonen MA, Tillery T, McColl R, Peshock RM, and Levine BD. Diastolic suction is impaired by bed rest: MRI tagging studies of diastolic untwisting. *J Appl Physiol*, 104:1037–44, 2008.

[33] Krishnamurthy G, Itoh A, Swanson JC, Bothe W, Karlsson M, Kuhl E, Craig Miller D, and Ingels NB Jr. Regional stiffening of the mitral valve anterior leaflet in the beating ovine heart. *J Biomech*, 42:2697–701, 2009.

[34] Saito S, Araki Y, Usui A, Akita T, Oshima H, Yokote J, and Ueda Y. Mitral valve motion assessed by high-speed video camera in isolated swine heart. *Eur J Cardiothorac Surg*, 30:584–91, 2006.

[35] Karlsson MO, Glasson JR, Bolger AF, Daughters GT, Komeda M, Foppiano LE, Miller DC, and Ingels NB Jr. Mitral valve opening in the ovine heart. *Am J Physiol*, 274:H552–63, 1998.

[36] Takeuchi M, Nakai H, Kokumai M, Nishikage T, Otani S, and Lang RM. Age-related changes in left ventricular twist assessed by two-dimensional speckle-tracking imaging. *J Am Soc Echocardiogr*, 19:1077–84, 2006.

[37] Nagueh SF, Appleton CP, Gillebert TC, Marino PN, Oh JK, Smiseth OA, Waggoner AD, Flachskampf FA, Pellikka PA, and Evangelisa A. Recommendations for the evaluation of left ventricular diastolic function by echocardiography. *Eur J Echocardiogr*, 10:165–93, 2009.

Chapter 3

Mitral Blood Velocity Compared to Volumetric Blood Flow Assessments of Diastolic Function using Cardiac Magnetic Resonance Imaging[1]

3.1 Introduction

Conventionally, diastolic function is assessed using Doppler echocardiography-derived measures of blood and tissue velocity [1–3]. Recently, cardiac magnetic resonance imaging (MRI) has also been applied in the research setting for the assessment of diastolic function [4–6]. A fundamental component of the diastolic function exam is the measurement of blood velocity at the mitral leaflet tips throughout diastole. The resulting velocity-time curves are used to calculate quantitative parameters such as the deceleration time (DT), defined as

[1]A version of this chapter has been published: Cheng-Baron J, Scott JM, Esch BT, Haykowsky MJ, Tyberg JV, Thompson RB. Relationship between mitral velocity and mitral flow time-profiles during ventricular filling. Proceedings of the International Society for Magnetic Resonance in Medicine, 18th Annual Meeting, Stockholm, Sweden. Abstract 3613, 2010.

the time for blood velocities to decay to zero following the early filling peak velocity, and the E/A wave ratio, which is the ratio of peak velocities during early filling (E-wave) and atrial contraction (A-wave). These parameters are used in conjunction with others, such as tissue Doppler imaging of mitral annular motion (E' and A') and pulmonary venous velocity (S, D and Ar), to classify subjects into groups describing worsening diastolic function. These standard clinical classifications are defined as normal, impaired relaxation, pseudonormalization and restricted filling patterns [1–3].

Mitral inflow with MRI is often measured using flow rate curves over the entire mitral valve area [4, 7–9] as opposed to velocity in a sample region, which has the advantage of representing volumetric heart function, offers increased signal to noise and reduced sensitivity to measurement location. However, while mitral blood flow rate curves resemble mitral blood velocity curves, with the characteristic E-wave and A-wave, the flow rate-derived parameters (E/A_{flow} and DT_{flow}) may not be interchangeable with velocity-derived parameters (E/A_{vel} and DT_{vel}). Specifically, mitral blood flow is not linearly related to mitral velocity due to its dependence on mitral valve area, which is known to vary throughout diastole [10], and on the spatial distribution of blood velocities over the filling orifice. The difference between mitral blood flow and velocity in terms of the E/A ratio and DT has not previously been described. Also, flow rate-derived diastolic parameters have not been reported for the clinical groups that characterize the range of diastolic dysfunction (normal, impaired relaxation, pseudonormalization and restricted filling). The aims of the current study were to compare MRI-derived blood velocity and blood flow time-courses and the derived parameters of diastolic function in younger and older healthy subjects and those with increasing diastolic dysfunction, representing the full range of clinical classifications.

3.2 Methods

3.2.1 Study Population

MRI studies were performed on younger healthy subjects (Group 1), older subjects with no history of heart disease (Group 2), older subjects with impaired relaxation, representing mild diastolic dysfunction (Group 3), and older subjects with pseudonormlized or restricted filling patterns, representing a more progressed form of diastolic dysfunction with suspected increased filling pressures (Group 4) [1–3]. All participants provided written, informed consent and the studies from which patients were included all received approval from the University of Alberta Health Research Ethics Board.

Group 1 subjects were included in the study described in Chapter 2. Group 2, 3 and 4 subjects were selected from participants in an ongoing clinical study of heart failure with preserved ejection fraction (Alberta HEART) which includes patients with heart failure, at risk for heart failure and healthy older controls. Consecutive subjects who fulfilled the inclusion criteria described below were included. Subjects were grouped according to diastolic parameters measured using MRI and clinical diagnosis. Group cutoffs were based on 95% confidence intervals for normal values by age as reported by Nagueh et al. [2]. Cutoffs were defined as follows:

- *Group 1—Normal, younger.* Healthy control subjects with no known cardiac conditions.

- *Group 2—Normal, older.* Healthy control subjects with maintained E-wave velocity (> 45 cm/s), normal E/A ratio (0.78–1.78 for 41–60 yrs, 0.60–1.32 for > 60 yrs) and normal DT (143–219 ms for 41–60 yrs, 142–258 ms for > 60 yrs).

- *Group 3—Impaired Relaxation.* Subjects at risk for or diagnosed with heart failure with depressed E-wave velocity < 45 cm/s, $E/A < 1$ and lengthened DT (> 219 ms for 41–60 yrs, > 258 for > 60 yrs).

- *Group 4—Pseudonormalized to Restricted Filling.* Subjects at risk for or diagnosed with heart failure with maintained E-wave velocity > 45 cm/s, $E/A > 1$ and shortened DT (< 143 ms for 41–60 yrs, < 142 for > 60 yrs) or with DT in the lower end of normal (< 170 ms) in combination with high indexed left atrial volume (> 60 ml/m^2).

3.2.2 Data Acquisition

MRI examinations were performed on a 1.5 T scanner (Sonata; Siemens Healthcare, Erlangen, Germany). Image acquisitions were electrocardiogram-gated and performed during breath holds. Steady-state free precession (SSFP) cines were acquired in the 2-, 3- and 4-chamber slice orientations and for a short-axis stack with full coverage of the LV. Typical imaging parameters were: 1.3 ms echo time (TE), 2.6 ms repetition time (TR), 144 $\times$ 256 matrix, 51° flip angle, 300 $\times$ 400 mm field of view (FOV), 8 mm slice thickness, 2 mm gap between short-axis slices, 238 kHz bandwidth (BW), rate 2 parallel imaging (GRAPPA) and 10–14 views per segment (VPS) for an acquired temporal resolution of 29–40 ms, reconstructed to 30 phases over the cardiac cycle. For phase contrast gradient echo cine imaging, both in-plane directional components of velocity were acquired in the 4-chamber slice orientation with each direction in a separate breath-hold. The through-plane directional component of velocity was acquired in a short-axis slice oriented perpendicular to the direction of flow and prescribed at the level of the LV base using long-axis 2-, 3-, and 4-chamber images at end-systole. Typical PC image acquisition parameters used were: 2.6–3.4 ms TE, 5.1–6.3 ms TR, 68 $\times$ 128 matrix, 20°

flip angle, 1.34 m/s velocity encoding strength, 293 × 360 mm FOV, 8 mm slice thickness, 77–114 kHz BW, 2–5 VPS and a temporal resolution of 30–63 ms, reconstructed to 64 cardiac phases.

3.2.3 Data Analysis

All data analysis was performed off-line (Matlab; Mathworks, Natick, MA). LV volumes were determined by manually tracing the LV myocardium in short axis SSFP slices and applying disk summation according to Simpson's rule. 2-, 3- and 4-chamber long axis slices were used to identify the LV apex and base to allow for the fractional inclusion of slices or extension of basal and apical slices. This technique is described in further detail in Section 2.2.3 of Chapter 2. Mitral annular excursion was calculated by identifying the LV apex and base on all long axis SSFP images at end-diastole and end-systole and was calculated as the total change in LV apex to base distance.

Blood velocity time-curves were measured at the mitral leaflet tips using the 4-chamber in-plane phase contrast cines, designed to match the standard sample volume used in Doppler echocardiography. Velocity-time curves were calculated as the velocity along the direction of blood flow averaged over pixels within a 0.5 cm radius of the measurement location center. The following diastolic parameters were measured: E-wave peak value (E_{vel}), time of E-wave peak (T_{Evel}), A-wave peak value (A_{vel}), time of A-wave peak (T_{Avel}), E/A_{vel} ratio, and DT_{vel} as shown in Figure 3.1. For DT_{vel}, a line was fit to the downward slope of the E-wave and extrapolated to zero velocity and was calculated as the time of peak velocity subtracted from the time of the extrapolated zero crossing [1–3].

Mitral flow-time curves were determined using the basal short-axis through-plane phase contrast cines. The mitral valve area was manually traced

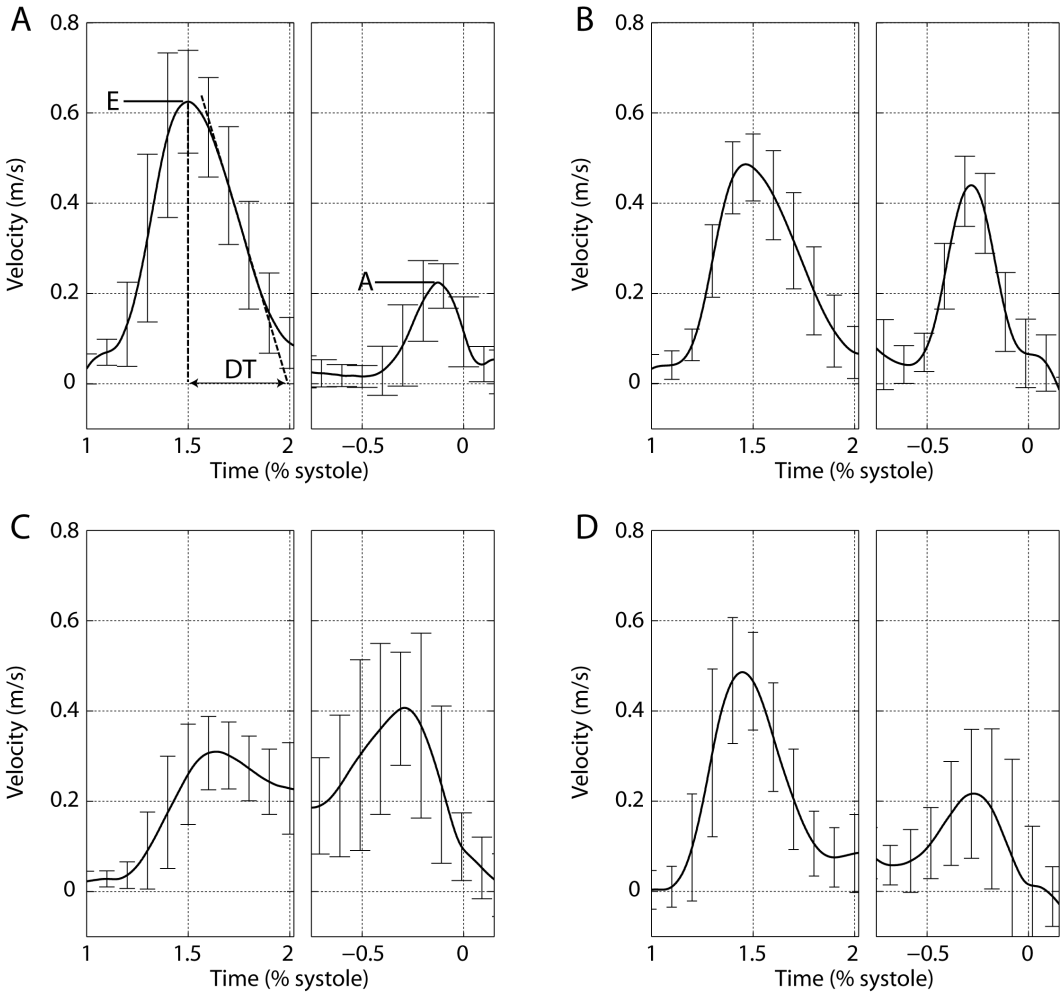

Figure 3.1: Blood velocity versus time for each group. Values averaged for all subjects within each group are shown for the (A) younger control (Group 2), (B) older control (Group 2), (C) impaired relaxation (Group 3), and (D) restricted filling (Group 4) groups. The E-wave is averaged with all curves being aligned at end-systole, and the A-wave is averaged with curves aligned at end-diastole as reflected in the time axis.

for each cardiac phase throughout diastole using both phase contrast magnitude and velocity images as guides. The mean velocity within the lateral wall of the LV basal myocardium was subtracted from the blood velocities to correct for through-plane motion of the base [11]. Within the traced areas, blood velocity was integrated to yield a flow rate (ml per second) and the corresponding flow diastolic parameters (E_{flow}, T_{Eflow}, A_{flow}, T_{Aflow}, E/A_{flow} ratio, DT_{flow}) were calculated for comparison with blood-velocity measures.

3.2.4 Representation of Data and Statistical Analysis

All graphical representations of data show the mean value averaged over all subjects at each time point with error bars indicating the standard deviation of the groups. Error bars are shown at times near the measurement points but with offsets for the clarity of presentation. The temporal duration of events is presented in absolute time (milliseconds), and the timings of events are normalized to aortic valve closure and are expressed as a percentage of systole. The method for determination of aortic valve closure and mitral valve opening is described in Section 2.2.3 of Chapter 2. Parameters reported were extracted from the individual data (as opposed to the averaged time curves) and are presented as mean ± standard deviation.

Statistical analysis was performed using IBM SPSS Statistics 19.0 (IBM Software Group, Somers, NY), and statistical significance was set at $p < 0.05$. Two-factor ANOVA was applied to all diastolic parameters with subject group as a between subject factor and measurement method (blood velocity versus flow) as a within subject factor. For 2-factor ANOVA applied to E-wave and A-wave peak values, velocity and flow are measured in different units and thus, the velocity versus flow main effect was disregarded.

3.3 Results

A total of 42 subjects were included for analysis: 10 in Group 1, 13 in Group 2, 9 in Group 3 and 10 in Group 4. Study population characteristics are shown in Table 3.1.

Table 3.1: Study population characteristics

	Group 1	Group 2	Group 3	Group 4
Sex, m/f	6/4	5/8	6/3	7/3
Age, yrs	28 ± 4	55 ± 5	66 ± 9	66 ± 9
Height, cm	174 ± 6	166 ± 8	170 ± 12	168 ± 11
Weight, kg	71 ± 9	72 ± 15	92 ± 28	84 ± 25
Body surface area, m^2	1.8 ± 0.1	1.8 ± 0.2	2.0 ± 0.4	1.9 ± 0.3
Heart rate, bpm	56 ± 8	63 ± 13	69 ± 10	65 ± 6
LV EF, %	61 ± 3	61 ± 4	49 ± 8	44 ± 16
LV EDV index, ml/m^2	107 ± 14	81 ± 8	80 ± 16	117 ± 50
LV ESV index, ml/m^2	42 ± 7	32 ± 4	41 ± 12	73 ± 51
LV mass index, g/m^2	63 ± 8	54 ± 8	61 ± 7	65 ± 19
LA volume index, ml/m^2	45 ± 9	46 ± 7	33 ± 8	62 ± 21
Mitral annular excursion, cm	1.8 ± 0.3	1.7 ± 0.2	1.2 ± 0.3	1.1 ± 0.6

EF = ejection fraction; EDV = end-diastolic volume; ESV = end-systolic volume.

Velocity-time curves averaged over all subjects within each group are shown in Figure 3.1, and comparisons of blood velocity and blood flow time-courses are shown in Figure 3.2. For all groups, flow-time curves peak earlier in time and decay more quickly than velocity-time curves. The time delays between peak blood velocity and flow are shown in Table 3.2. The comparisons of other diastolic parameters are also shown in Table 3.2 and results from the two-factor ANOVAs are shown in Table 3.3. Notably, E/A did not show differences for measurement method (velocity versus flow) or for an interaction. In contrast, DT was significant for measurement method and for an interac-

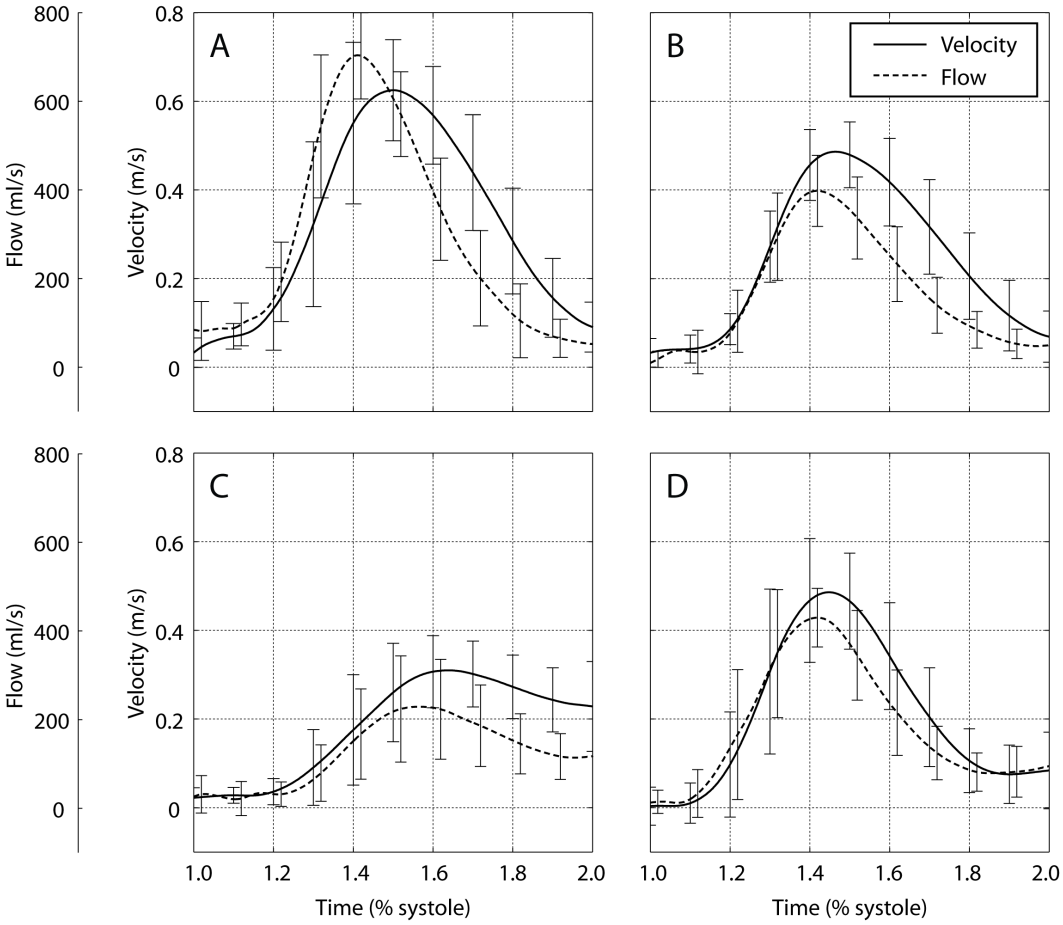

Figure 3.2: Blood velocity versus time compared to blood flow versus time for early filling. Values are averaged for all subjects within each group are shown (A) for the younger control (Group 1), (B) older control (Group 2), (C) impaired relaxation (Group 3), and (D) restricted filling (Group 4) groups.

Table 3.2: Velocity and flow derived diastolic parameters

	Group 1	Group 2	Group 3	Group 4
E				
Velocity, cm/s	66 ± 9	51 ± 7	32 ± 8	53 ± 10
Flow, ml/s	717 ± 117	421 ± 89	239 ± 114	466 ± 99
T_E				
Velocity, % systole	149 ± 8	147 ± 6	162 ± 7	145 ± 7
Flow, % systole	141 ± 3	142 ± 4	158 ± 8	141 ± 6
$\Delta_{Flow-Vel}$, ms	-29 ± 24	-16 ± 15	-14 ± 12	-14 ± 16
A				
Velocity, cm/s	27 ± 5	45 ± 8	53 ± 18	33 ± 16
Flow, ml/s	296 ± 66	335 ± 72	402 ± 133	132 ± 134
T_A				
Velocity, % systole	324 ± 21	263 ± 32	256 ± 33	245 ± 38
Flow, % systole	309 ± 19	259 ± 33	255 ± 34	240 ± 36
$\Delta_{Flow-Vel}$, ms	-53 ± 42	-14 ± 34	-3 ± 13	-14 ± 27
E/A				
Velocity	2.6 ± 0.8	1.1 ± 0.1	0.7 ± 0.2	2.1 ± 1.2
Flow	2.5 ± 0.5	1.2 ± 0.2	0.6 ± 0.2	1.8 ± 1.1
$\Delta_{Flow-Vel}$	-0.09 ± 0.75	0.10 ± 0.14	-0.07 ± 0.13	-0.26 ± 0.32
DT				
Velocity (ms)	164 ± 17	169 ± 27	275 ± 56	126 ± 23
Flow (ms)	139 ± 27	148 ± 23	207 ± 52	126 ± 26
$\Delta_{Flow-Vel}$, ms	-25 ± 24	-21 ± 23	-69 ± 61	0 ± 34

Table 3.3: Two-factor ANOVA for velocity and flow derived diastolic parameters

	Group	Method	Interaction
E	< 0.001	—	< 0.001
T_E	< 0.001	< 0.001	NS
A	NS	—	NS
T_A	< 0.001	< 0.01	< 0.05
E/A	< 0.001	NS	NS
DT	< 0.001	< 0.001	< 0.01

Method refers to the parameter being measured from velocity-time curves versus from flow-time curves. NS = not significant ($p < 0.05$).

tion, indicating not only a difference between DT_{vel} and DT_{flow}, but that the difference between DT_{vel} and DT_{flow} was smaller or larger for some groups compared to others. Figure 3.3 shows velocity-derived E/A and DT compared to flow-derived values for each subject as well as post hoc comparisons between flow-derived and velocity-derived DT for each group.

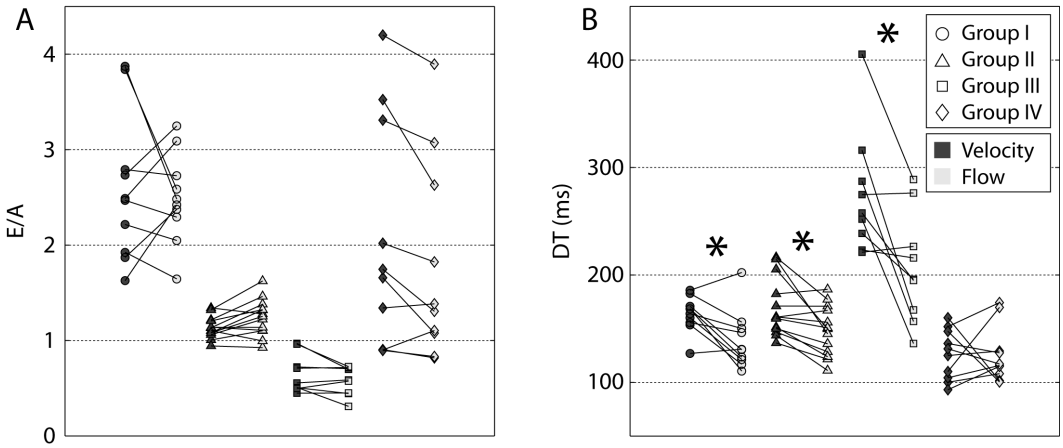

Figure 3.3: Velocity-derived and flow-derived measures of E/A and DT for all subjects. Subjects are arranged by group, with lines connecting parameters from the same subject. *Indicates $p < 0.05$ for comparison between flow-derived and velocity-derived DT.

3.4 Discussion

The major findings of the current study are: (1) Blood velocity and blood flow time-courses have different E-wave and A-waves time-profiles with blood flow-time curves peaking earlier in time and decaying away more quickly than blood velocity-time curves. (2) E/A_{vel} and E/A_{flow} are similar, suggesting that E/A_{flow} may be interchangeable with E/A_{vel}. However, DT_{vel} and DT_{flow} show discrepancies which suggest that DT_{flow} cannot be substituted for DT_{vel}. (3) With increasing severity of diastolic dysfunction, there are reduced differences between flow and velocity time-courses, which may be the result of a less dynamic mitral annulus.

Previous MRI studies assessing diastolic filling parameters have used both velocity measured at the leaflet tips, emulating an echocardiography exam, [4–6] and mitral flow rate, where velocity is integrated over the entire filling orifice [7–9]. The volumetric flow rate approach has the advantages of increased signal to noise and reduced sensitivity to measurement location. Additionally, flow-rates are an appealing measure because they represent the global volumetric function of the heart as opposed to a local velocity. However, the findings presented indicate that current guidelines for the characterization of diastolic function cannot be directly applied to blood flow-derived parameters, particularly for deceleration times. Overall, DT_{flow} was shorter than DT_{vel} (p ANOVA for velocity versus flow < 0.001). For example, if current DT_{vel} cutoffs were applied to DT_{flow} values, 5 out of 9 Group 3 subjects (impaired relaxation) would have DT_{flow} values considered normal (< 200 ms), and 6 out of 10 Group 1 subjects (young healthy) would have DT_{flow} suggestive of a restricted filling pattern (< 140 ms), although 1 of these subjects also has a lower than normal DT_{vel} value (Figure 3.3). Furthermore, discrepancies between DT_{flow} and DT_{vel} were inconsistent between groups (p ANOVA for interaction < 0.01) resulting in more overlap for DT_{flow} amongst groups than for DT_{vel}.

The differences between the velocity-derived and flow-derived parameters are a result of their differing time-courses, as shown in Figure 3.2. It can be observed that when flow rate begins to decrease blood velocity is still increasing and is subsequently maintained for a longer time period. The delay in peak velocity compared to peak flow ranged from 13 ± 12 ms for Group 3 up to 29 ± 24 ms for Group 1. This discrepancy between blood velocity and flow has previously been observed by Flewitt et al. [12] in a dog model using Doppler echocardiography for blood velocity and the rate of change of LV

volume measured using sonomicrometry. The difference in flow and velocity time-courses is likely a consequence of the temporal variation in mitral valve area, described by Bowman et al. [10]. Specifically, the decrease in mitral annular area with the onset of reduced blood flow rate acts to maintain blood velocity, altering the relationship between blood flow and blood velocity. Despite the systematic differences between the flow and velocity time-courses, E/A values were similar for all groups using both approaches.

3.4.1 Mitral Annular Motion and Deformation

E and DT were both statistically significant when tested for an interaction between subject group and measurement method. From Figure 3.4A, it can be observed, that proportionally, when compared to E_{vel}, E_{flow} is higher for the younger control group (Group 1) compared to all older groups (Groups 2–4). A similar trend can be observed for A, although this interaction did not reach statistical significance. From Tables 3.2 and 3.3, DT_{flow} is generally lower than DT_{vel}, but more so for Group 3 and less so for Group 4. Differences between flow and velocity can be attributed to changes in the mitral filling area, both as it moves away from the apex and as it deforms (i.e. expands or contracts). The motion of the mitral valve, as it moves away from the apex, is incorporated in the flow rate by subtracting the mitral annular velocity from velocities measured within the filling orifice, while deformation is incorporated by integrating velocities over the entire mitral valve area as it changes throughout diastole. The displacement of the annulus (often referred to as E' and A') occurs only over a brief time period during the upslope of the filling wave, and thus should not impact measurements of the peak filling value or of DT. The deformation of the mitral annulus however, occurs throughout diastole and is more likely the cause of the differences observed.

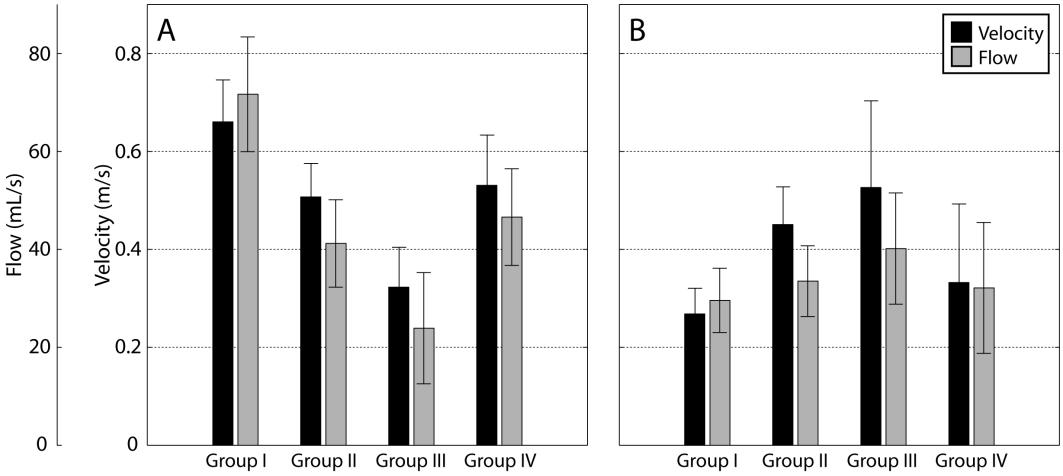

Figure 3.4: Velocity-derived and flow-derived peak filling velocities. (A) Peak E-wave and (B) A-wave values are compared.

As shown in Figure 3.4, Group 1 subjects have proportionally larger flow rates for lower filling velocities compared to older subjects, both with and without diastolic dysfunction. A possible mechanism for this finding is that these subjects may have more dynamic expansion of the mitral annulus or larger mitral valve area. Moreover, when comparing DT_{flow} and DT_{vel}, a smaller discrepancy was observed for Group 4 compared to Groups 1 and 2 (Table 3.2). Again, this may be a result of more dynamic changes in mitral valve area for Groups 1 and 2 in the deceleration phase of early filling. Mitral annular excursion (Table 3.1) was lower for Groups 3 and 4 compared to younger and older controls, further supporting the assertion that, in these groups, the mitral valve is less dynamic, leading to more similarity between velocity and flow.

Only the larger difference between DT_{vel} and DT_{flow} for Group 3 seems to contradict the trend of increasing similarity between velocity and flow with worsening diastolic function; however, this result may reflect an additional factor. For this group, E_{vel} is low (33 ± 7 cm/s) and is thus, closer in value to residual velocities that persist during diastasis. These residual velocities may

lead to longer measured DT_{vel}. Conversely, residual velocities are attenuated in the measurement of flow-time curves due to a reduction in mitral valve during the downward slope of the E-wave, and thus, do not elongate DT_{flow}.

3.4.2 MRI Measurement of Diastolic Function

It has been shown that blood inflow parameters measured using phase contrast MRI generally agree with those measured using echocardiography [6–8, 13–16]. Furthermore, MRI offers the advantage over echocardiography that any component direction of blood velocity can be acquired over a 2-dimensional imaging plane, which allows for the determination of volumetric mitral blood flow. Volumetric blood flow is an appealing measure because in addition to increasing signal to noise, it is directly related to diastolic changes in left ventricular volume. For instance, a large mitral annular area allows for adequate LV filling in the presence of low mitral velocities. Conversely, low filling rates may occur in the presence of high filling velocities. Thus, it is perhaps not surprising that flow-derived parameters cannot be substituted for velocity-derived values. Further studies will be required to determine if parameters such as DT_{flow} provide complimentary information or if blood flow would be best characterized by a different set of quantitative parameters.

3.4.3 Limitations

The current study is limited by the 30–63 ms temporal resolution of the phase contrast MRI sequence, which reduces the accuracy of the timings of events, although significant differences in event timings and durations were shown for several metrics. Velocity offsets due to eddy current induced residual phase are a known source of error for phase-contrast flow quantification [17]. These errors are most problematic for volume calculations because of the

accumulation of errors when integrating over time. The current study avoids this more serious error and is only subject to an overall offset because the peak velocities or flow rates are desired and not integrated volumes. Furthermore, parameters of interest are calculated from the shape of the flow rate-time curve, which is unaffected by an overall offset.

It is now possible to acquire blood velocity images with 3-dimensional spatial coverage and sensitivity to all 3 directional components of velocities. These sequences have been used to incorporate mitral annular motion into more accurate quantification of diastolic mitral blood flow [8]. However, these methods are more time consuming and not widely available, making them potential research tools for studying blood flow, but less ideal for clinical use when compared to simpler velocity encoding MRI techniques, such as the one used in the current study.

3.4.4 Conclusions

Mitral blood velocity and volumetric flow rates measured in younger and older healthy controls and subjects with worsening diastolic function were found to have distinct diastolic time-courses, indicating that flow and velocity time-courses are not generally interchangeable. Flow-derived DT is significantly lower than conventional velocity-derived values and the amount of discrepancy is inconsistent amongst groups. However, velocity-derived and flow-derived E/A were found to be interchangeable in all classification groups.

3.5 Chapter 3 References

[1] Appleton CP, Jensen JL, Hatle LK, and Oh JK. Doppler evaluation of left and right ventricular diastolic function: a technical guide for obtaining optimal flow velocity recordings. *J Am Soc Echocardiogr*, 10(3):271–92, 1997.

[2] Nagueh SF, Appleton CP, Gillebert TC, Marino PN, Oh JK, Smiseth OA, Waggoner AD, Flachskampf FA, Pellikka PA, and Evangelisa A. Recommendations for the evaluation of left ventricular diastolic function by echocardiography. *Eur J Echocardiogr*, 10:165–93, 2009.

[3] Oh JK, Seward JB, and Tajik AJ. Assessment of Diastolic Function. In *The Echo Manual*, pages 45–57. Lippincott Williams and Wilkins, Philadelphia, second edition, 1999.

[4] Duarte R and Fernandez G. Assessment of left ventricular diastolic function by mr: why, how and when. *Insights Imaging*, 1(3):183–92, 2010.

[5] Paelinck BP, Lamb HJ, Bax JJ, van der Wall EE, and de Roos A. MR flow mapping of dobutamine-induced changes in diastolic heart function. *J Magn Reson Imaging*, 19(2):176–81, 2004.

[6] Rathi VK, Doyle M, Yamrozik J, Williams RB, Caruppannan K, Truman C, Vido D, and Biederman RW. Routine evaluation of left ventricular diastolic function by cardiovascular magnetic resonance: a practical approach. *J Cardiovasc Magn Reson*, 10:36, 2008.

[7] Bollache E, Redheuil A, Clement-Guinaudeau S, Defrance C, Perdrix L,

Ladouceur M, Lefort M, De Cesare A, Herment A, Diebold B, Mousseaux E, and Kachenoura N. Automated left ventricular diastolic function evaluation from phase-contrast cardiovascular magnetic resonance and comparison with Doppler echocardiography. *J Cardiovasc Magn Reson*, 12:63, 2010.

[8] Brandts A, Bertini M, van Dijk EJ, Delgado V, Marsan NA, van der Geest RJ, Siebelink HM, de Roos A, Bax JJ, and Westenberg JJ. Left ventricular diastolic function assessment from three-dimensional three-directional velocity-encoded MRI with retrospective valve tracking. *J Magn Reson Imaging*, 33(2):312–9, 2011.

[9] Mendoza DD, Codella NC, Wang Y, Prince MR, Sethi S, Manoushagian SJ, Kawaji K, Min JK, LaBounty TM, Devereux RB, and Weinsaft JW. Impact of diastolic dysfunction severity on global left ventricular volumetric filling - assessment by automated segmentation of routine cine cardiovascular magnetic resonance. *J Cardiovasc Magn Reson*, 12:46, 2010.

[10] Bowman AW, Frihauf PA, and Kovcs SJ. Time-varying effective mitral valve area: prediction and validation using cardiac MRI and Doppler echocardiography in normal subjects. *Am J Physiol Heart Circ Physiol*, 287:H1650–7, 2004.

[11] Kayser HW, Stoel BC, van der Wall EE, van der Geest RJ, and de Roos A. MR velocity mapping of tricuspid flow: correction for through-plane motion. *J Magn Reson Imaging*, 7(4):669–73, 1997.

[12] Flewitt JA, Hobson TN, Wang J Jr, Johnston CR, Shrive NG, Belenkie I, Parker KH, and Tyberg JV. Wave intensity analysis of left ventricular

filling: application of windkessel theory. *Am J Physiol Heart Circ Physiol*, 292:H2817–23, 2007.

[13] Westenberg JJ. Cmr for assessment of diastolic function. *Curr Cardiovasc Imaging Rep*, 4(2):149–158, 2011.

[14] Hartiala JJ, Mostbeck GH, Foster E, Fujita N, Dulce MC, Chazouilleres AF, and Higgins CB. Velocity-encoded cine MRI in the evaluation of left ventricular diastolic function: measurement of mitral valve and pulmonary vein flow velocities and flow volume across the mitral valve. *Am Heart J*, 125(4):1054–66, 1993.

[15] Rubinshtein R, Glockner JF, Feng D, Araoz PA, Kirsch J, Syed IS, and Oh JK. Comparison of magnetic resonance imaging versus Doppler echocardiography for the evaluation of left ventricular diastolic function in patients with cardiac amyloidosis. *Am J Cardiol*, 103(5):718–23, 2009.

[16] Karwatowski SP, Brecker SJ, Yang GZ, Firmin DN, Sutton MS, and Underwood SR. Mitral valve flow measured with cine MR velocity mapping in patients with ischemic heart disease: comparison with Doppler echocardiography. *J Magn Reson Imaging*, 5(1):89–92, 1995.

[17] Rolf MP, Hofman MB, Gatehouse PD, Markenroth-Bloch K, Heymans MW, Ebbers T, Graves MJ, Totman JJ, Werner B, van Rossum AC, Kilner PJ, and Heethaar RM. Sequence optimization to reduce velocity offsets in cardiovascular magnetic resonance volume flow quantification–a multi-vendor study. *J Cardiovasc Magn Reson*, 13:18, 2011.

Chapter 4

Flow Propagation in the Left Atrium[1]

4.1 Introduction

Most imaging-derived parameters for the evaluation of diastolic function focus on mitral and ventricular blood velocities and ventricular tissue velocities, which are used to provide a grading of diastolic dysfunction [1, 2]. The left atrium (LA), in combination with the pericardium, also plays a critical role in normal diastolic function, and parameters of atrial blood velocity and volume offer further insight into diastolic filling pressures. Pulmonary venous blood velocity is used to infer elevated filling pressures [2–4] and increased LA volume is associated with remodeling due to sustained high filling pressures over time [2, 5]. LA functional parameters such as passive and active emptying fractions have been used to evaluate the roles of the LA as reservoir, conduit and pump [5]. Left atrial compliance is directly related to reservoir function and represents the ability of the LA to store and release elastic energy [6–9]. Compliance is also associated with absolute pressures in the chamber, where

[1]A portion of this chapter has been previously published: Cheng-Baron J, Chow K, Pagano JJ, Nelson MD, Paterson DI, Thompson RB. Propagation of blood flow in the left atrium during diastole. Proceeding of the International Magnetic Resonance Angiography Working Group, 23rd Annual Meeting, Banff, Canada. Abstract 3.8, 2011.

compliance is reduced when operating at increased volumes and pressures [5].

In large conduit blood vessels such as the aorta, compliance has been evaluated using pulse wave velocity (PWV) of the forward travelling pressure wave associated with systolic contraction, where an increased PWV is associated with increased vessel stiffness or reduced compliance [10, 11]. Invasively measured wave intensity analysis has previously been used to demonstrate forward propagating compression waves in the aorta [12] as well as a backwards propagating expansion wave, in the direction opposite blood flow, in the left heart during early filling [13, 14]. This suggests the potential for the measurement of PWV-like effects in the atrium.

The phenomenon of wave-like propagation of blood flow has been observed in the left atrium [15–17]; however, these few studies have reported conflicting results and without consideration of all cardiac phases. Palecek et al. measured LA propagation velocity during systole, assumed to reflect reservoir function, of greater than 200 cm/s using Doppler M-mode echocardiography [15]. Measurement with M-mode echocardiography is technically challenging during systole due to vortical flow patterns in the left atrium during this time [18, 19]. Stoddard et al. made similar measurements during both systole and early filling and measured wave speeds around 40 cm/s [16, 17], considerably lower than those measured by Palecek et al. Also, the direction of propagation during early filling was found to be in the filling direction, opposite in direction to the backwards travelling wave observed using wave intensity analysis [13, 14].

The goals of the current study were to determine if patterns of flow propagation are measureable in the healthy left atrium using phase contrast blood velocity imaging during the 3 distinct filling phases: systole (S-wave), early filling (E-wave) and atrial contraction (A-wave). We hypothesized that

left atrial V_p could be measured at each of these cardiac phases (V_{p_S}, V_{p_E}, V_{p_A}), with forward propagating waves in systole and with atrial contraction, backwards propagating waves during early filling, but that V_{p_S} is less well defined due to vortices during this phase.

4.2 Methods

4.2.1 Subject Population

Cardiac MRI exams were performed on a group of 9 healthy individuals (5 male/4 female, 27 ± 4 years). The study protocol was approved by the University of Alberta Health Research Ethics Board and all study participants provided written informed consent.

4.2.2 Data Acquisition

MRI exams were performed on a 1.5 T scanner (Sonata; Siemens Healthcare, Erlangen, Germany). Image acquisitions were electrocardiogram-gated and acquired during breath-holds at end-expiration. Phase-contrast (PC) cine velocity imaging using a gradient echo sequence was acquired for the 2 in-plane components of velocity in a 4-chamber view of the heart. Each directional component of velocity was acquired in a separate breath-hold. Typical imaging parameters were: 3.2 ms echo time (TE), 4.9 ms repetition time (TR), 30° flip angle, 75×128 matrix, $(187–275) \times 400$ mm field of view (FOV), 58 kHz bandwidth (BW), 1.2 m/s velocity encoding strength, 8 mm slice thickness, rate 2 parallel imaging (GRAPPA), 3 views per segment (VPS) and 2 phase encoding steps for an acquired temporal resolution of 29.5 ms and reconstructed to 10 ms per cardiac phase using pixel-wise piecewise cubic spline interpolation.

Steady-state free precession cine imaging was acquired to determine ventricular volumes using a method of disks technique described in Section 2.2.3 of Chapter 2. A short axis stack spanning the LV length and 2-chamber, 3-chamber and 4-chamber long axis views of the heart were acquired. Typical imaging parameters were: 1.5 ms TE, 2.0 ms TR, 65° flip angle, (94–146) × 256 matrix, (207–288) × 400 mm FOV, 8 mm slice thickness, 2 mm gap between slices, 238 kHz BW, rate 2 parallel imaging (GRAPPA) and 12 VPS for an acquired temporal resolution of 39 ms and reconstructed to 64 cardiac phases.

4.2.3 Data Analysis

All data analysis was performed offline (Matlab; Mathworks, Natick, MA) and values are represented as mean ± standard deviation.

Blood flow patterns were visualized using blood velocity streamlines for each subject during 3 cardiac phases corresponding to the time of peak velocity during the S-wave, the E-wave and the A-wave. Only streamlines originating within the LA were visualized (Figure 4.1). The uniformity of blood flow within the LA was graded as follows: 1) no vortical streamlines, 2) mostly unidirectional streamlines with some vortical patterns and 3) approximately half or more of the area occupied by vortical streamlines.

Blood velocity-time curves were measured in the LA. A region of interest within the LA was manually selected (Figure 4.2A), with care to exclude regions of vortical flow as represented by streamlines. Each filling phase was segmented individually to account for changes in LA shape over the cardiac cycle. The direction of blood flow was also estimated using streamlines, and blood velocity curves were determined as a function of location along the indicated direction. The curves were calculated as the directional component of velocity in the selected direction of blood flow averaged within a 5 mm long

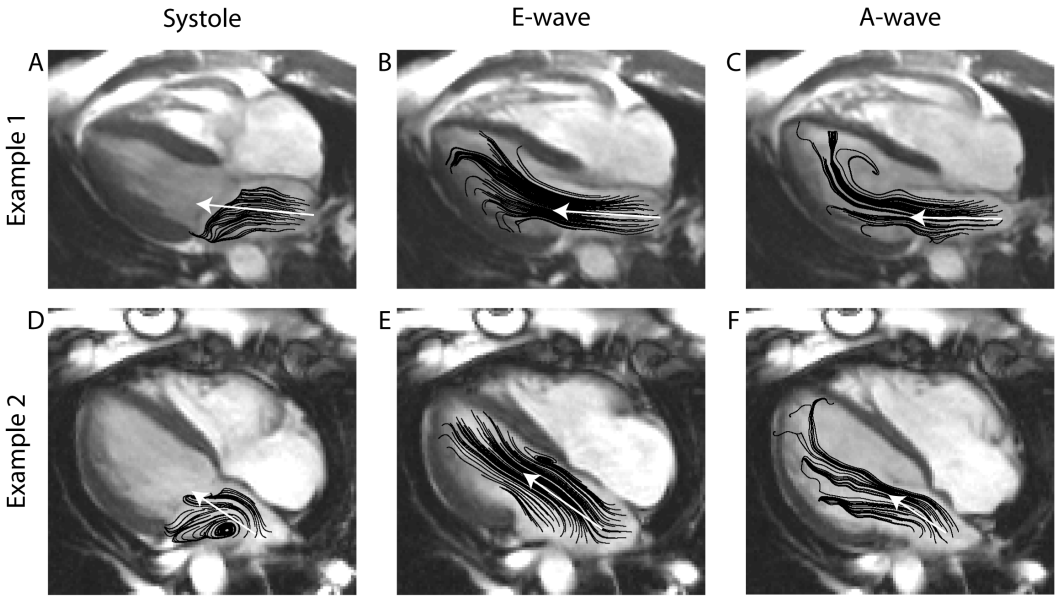

Figure 4.1: Streamlines originating in the left atrium. Streamlines are shown for 2 representative individuals. Cardiac phases shown are at peak velocity within the left atrium during (A and D) the S-wave, (B and E) the E-wave and (C and F) the A-wave. A white arrow indicates the approximate direction of blood flow as identified by the user.

region in the same direction (Figure 4.2A, inset). Velocity-time curves were calculated every 1 mm, resulting in overlapping regions. Example curves are shown in Figure 4.2B for the E-wave.

To determine propagation velocity from velocity-time curves, these curves were displayed as spatial-temporal colourmaps with time on the x-axis and distance along the LA length on the y-axis as shown in Figure 4.3, similar to the colour M-mode display in echocardiography. V_p was calculated from the slope of a manually drawn line approximating the time of peak velocity as a function of spatial location. The peak value for each spatial location was also shown on the same plot as a visual aid in the determination of V_p.

As described above, V_p was determined using delays in the peak velocity. The effect of using temporal delays in peak velocity as opposed to using isocontour lines was studied using synthetic spatial-temporal velocity maps. Velocity-time curves for the synthetic data were defined to have the same shape

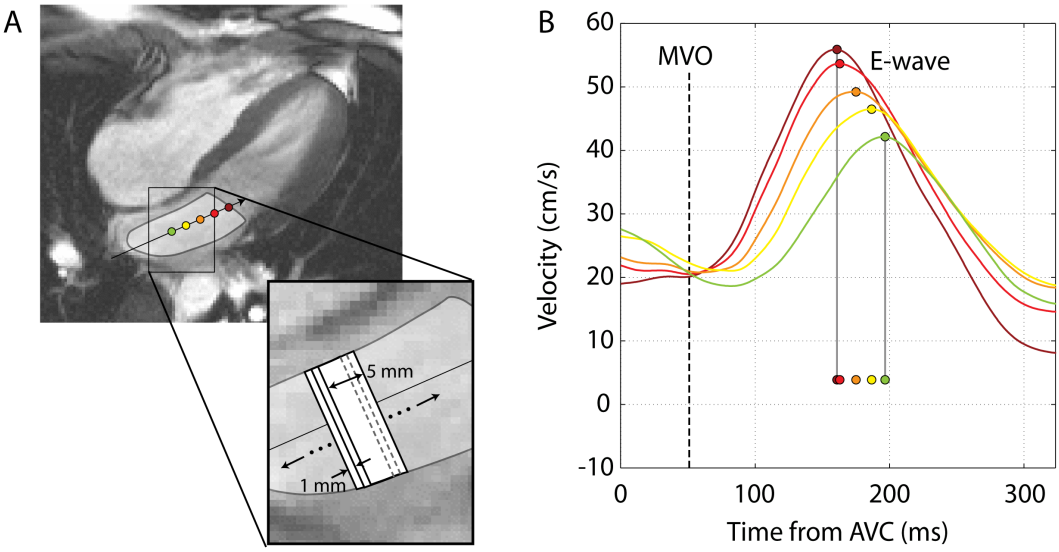

Figure 4.2: Method for calculating left atrial velocity-time curves for the E-wave. (A) The LA is manually traced. (B) Resulting velocity-time curves are shown following aortic valve closure (AVC) with mitral valve opening (MVO) indicated by the dashed line. For clarity, only 5 curves are displayed at arbitrary, but evenly spaced, regions. The timing of peak values are indicated.

at all locations in space, but were scaled in magnitude, being larger nearer to the mitral valve, and smaller towards the top of the LA and a temporal shift in the velocity-time curve was applied to mimic a temporal delay in the filling wave as a function of space.

4.3 Results

Subject population characteristics are shown in Table 4.1.

Representative streamlines for 2 subjects are shown in Figure 4.1 during the S-wave, the E-wave and the A-wave, representing the range of observed S-wave streamline patterns with panel A showing the most unidirectional S-wave and panel D showing the most vortical S-wave. For the S-wave, 2 subjects had no vortical patterns, 4 subjects had some vortical patterns and 3 subjects had approximately half or more of the LA area occupied by vortical patterns. None

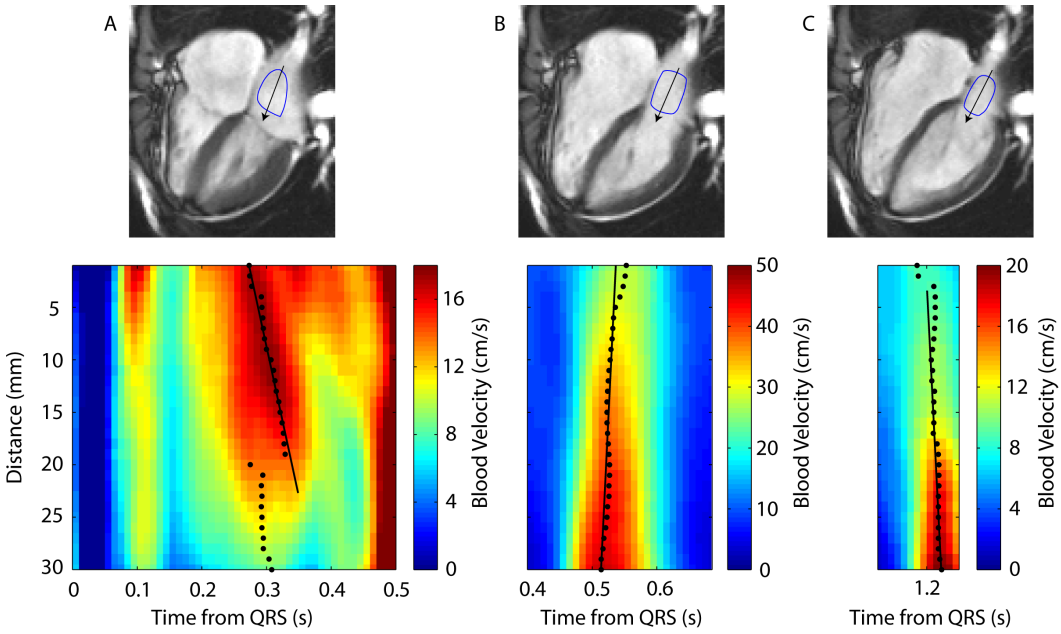

Figure 4.3: Spatial-temporal velocity maps for a representative subject for the (A) S-wave, (B) E-wave and (C) A-wave. The distance axis spans 30 mm within the left atrium, oriented with the top of the atrium represented by smaller values and locations closer to the left ventricle represented by larger values. Spatial and temporal scales are the same for all three panels, but velocity scales differ for clarity. Peak velocity as a function of space is shown by circles. Propagation velocity is shown by a line.

Table 4.1: Subject characteristics

Sex, m/f	5/4
Age, years	27 ± 4
Height, cm	174 ± 6
Weight, kg	70 ± 9
Body surface area, m^2	1.8 ± 0.1
Heart rate, beats per minute	54 ± 6
Systolic blood pressure, mmHg	116 ± 9
Diastolic blood pressure, mmHg	70 ± 6
Ejection fraction, %	61 ± 3

of the subjects had vortical streamlines during the E-wave or A-wave.

An example of spatial-temporal velocity colourmaps are shown in Figure 4.3 with V_p indicated. For all subjects, velocity propagation was toward the LV for the S-wave and A-wave; i.e., a longer delay in peak flow was observed closest to the ventricle. However, velocity propagated in the opposite direction, toward the top of the LA, for the E-wave. Temporal delays in the peak velocity as a function of distance from the mitral annulus for the E-wave and A-wave are shown in Figure 4.4. For all subjects, the propagation of velocity can be observed to occur in opposite directions. V_p for all subjects and filling phases is shown in Figure 4.5. Measured propagation velocities were $V_{p_S} = 72 \pm 68$ cm/s, $V_{p_E} = -118 \pm 45$ cm/s and $V_{p_A} = 105 \pm 29$ cm/s.

Figure 4.6 shows 2 artificial examples of blood velocity over space within the left atrium. Panels A and B show velocity curves with the same shape at all points in space, but scaled in magnitude with higher velocities nearer to the mitral valve. In this case, V_p measured using peak velocity yields no temporal delay and $V_p = \inf$ (solid line in panel A). Isocontour lines result in a measureable delay, which depends on the velocity chosen (dashed lines in panel A). Panels C and D show the same velocity waveforms with variable temporal shifts applied as a function of space, with delays increasing towards the top of the atrium. In this case, V_p measured using peak velocity reflects the delay applied, while isocontour lines yield slower V_p, which also depends on the velocity chosen.

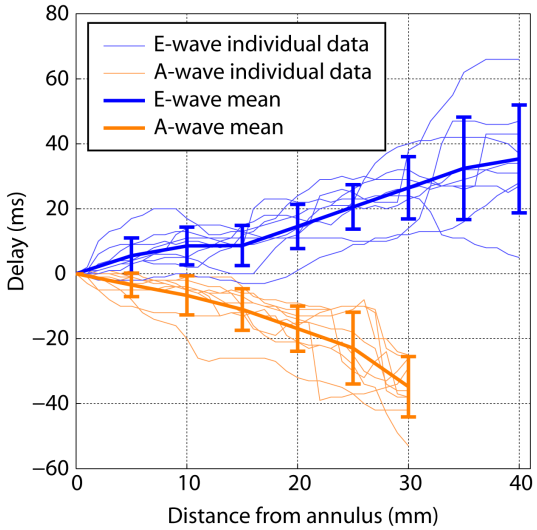

Figure 4.4: Temporal delay in peak E-wave and A-wave velocity as a function of distance from the mitral annulus.

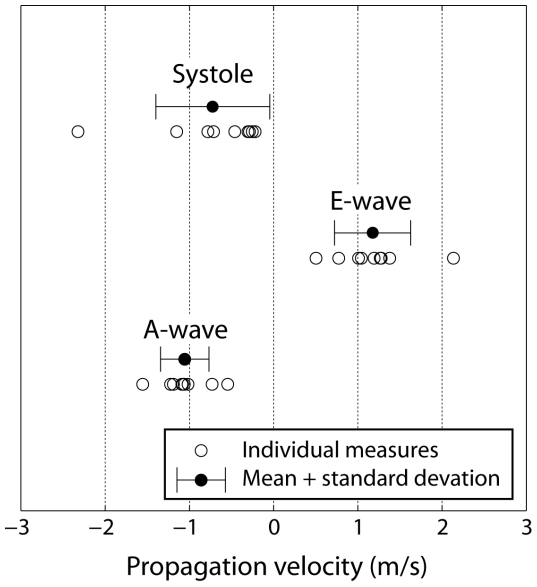

Figure 4.5: Propagation velocity for all subjects and all filling phases. Positive values indicate propagation towards the top of the left atrium. Negative values indicate propagation toward the left ventricle.

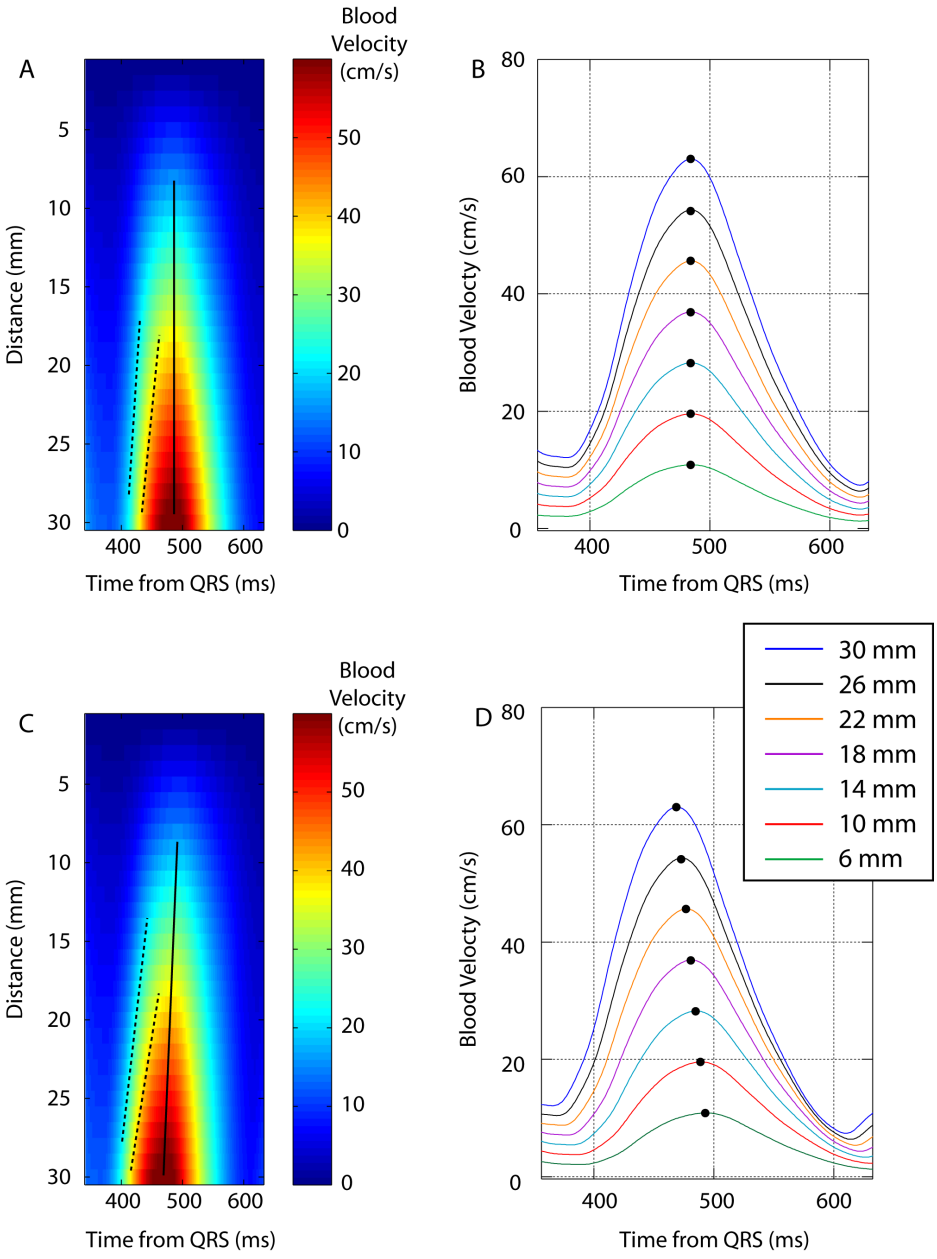

Figure 4.6: Examples of synthetic E-wave velocity data and associated V_p. The top of the atrium is represented by smaller values and locations closer to the left ventricle represented by larger values. Velocity curves with the same time-course scaled linearly over space are shown as (A) a spatial-temporal map and (B) at spatial locations spaced 4 mm apart. Peak values (black dots) occur simultaneously. Velocity curves with the time-courses shifted by 1 ms per 1 mm and scaled linearly over space are shown as (C) a spatial-temporal map and (D) at spatial locations spaced 4 mm apart. Peak values (black dots) are delayed in time as a function of space. Propagation velocity measured using peak values is shown by solid lines. Propagation velocity measured using two different constant velocities are shown by dashed lines.

4.4 Discussion

Blood flow in the LA was observed using streamlines to be unidirectional during both the E-wave and A-wave and to be more variable during systole, with similar patterns to previous 3-dimensional flow studies [18, 19]. Propagation velocity was measurable during all 3 pulsatile phases in the left atrium and was found to be propagating toward the LV during systole and the A-wave, in the same direction as blood flow, consistent with forward compression waves [14]. Conversely, velocity propagated toward the top of the LA during the E-wave, opposite in direction to blood flow, consistent with a backwards expansion wave [13, 14].

4.4.1 Left Atrial V_p during Systole

Right ventricular systole drives left atrial filling and is also the source of the observed LA flow propagation during the S-wave. In the current study, V_{p_S} was measured as propagating from the top of the LA toward the LV base at 72 ± 68 m/s. However, vortices have been described in the LA throughout systole which disappear with the onset of early filling [18, 19]. These vortices depend on individual LA anatomy and have been shown to vary with many parameters including age, gender, blood pressure and LV volume [19]. In the current study, vortical streamlines were observed in 7 out of 9 subjects during the S-wave. As can be observed in Figure 4.1 and Figure 4.3, this results in V_p during systole being less clearly defined than during other filling phases. Other studies using colour M-mode Doppler echocardiography have measured S-wave propagation velocity to be as low as 40 cm/s [16] to as high as 200 cm/s [15]. This discrepancy may be attributed to complex flow patterns and difficulties in visualizing complex flow patterns using 1-dimensional velocity

measurement techniques.

4.4.2 Left Atrial V_p during Early Filling

V_p in the LA during early filling was found to propagate in the direction opposite of blood flow. The observed direction of V_{p_E} contradicts a previous observations of V_{p_E} by Stoddard et al. [16, 17], but agrees with the observation of a backwards expansion wave due to ventricular suction measured using wave intensity analysis [13, 14]. Similar to PWV measured in major blood vessels [10, 11], it is likely that V_{p_E}, if indeed representing a backwards expansion wave, is related to LA compliance, where a more compliant chamber results in a slower V_{p_E} and a stiffer chamber results in a faster V_{p_E}.

Left atrial volume has been used as a measure of diastolic dysfunction where elevated filling pressures over time lead to LA enlargement [20]. However, LA volume is a measure of the chronicity of elevated filling pressure as opposed to a more instantaneous measure of filling pressures. In particular, it cannot detect the early elevation of filling pressures that precede LA remodeling. Futhermore, LA remodeling can also be affected by mechanisms beyond filling pressures such as pericardial constraints. These increased pressures however, reduce the compliance of the LA [21]. Thus, the relationship between compliance and V_{p_E} offers a way to indirectly measure instantaneous filling pressures.

4.4.3 Left Atrial V_p during Atrial Contraction

The direction of V_{p_A} was observed to be the same as V_{p_S} and opposite that of V_{p_E}. This result is consistent with the different mechanisms behind these filling waves, where the S-wave is related to right ventricular contraction, the E-wave is related to ventricular suction and the A-wave results from

atrial contraction. However, the significance of the non-uniform motion observed is less clear for the A-wave because the LA is actively contracting as opposed to being in a passive state as it is during the S-wave and the E-wave. During contraction, the compliance of the chamber is continuously changing. Moreover, electrical activation of the myocytes propagates from the sinoatrial node to the top of the left atrium and down though the Bachmann's bundle [22]. This causes contraction to occur first at the top of the atrium, consistent with the direction of propagation velocity observed. The propagation of electrical activation has been shown to range from 80 cm/s to 131 cm/s in canine hearts [23], approximately equal in magnitude to the propagation of maximum velocity observed in the current study of 105 cm/s. This suggests that electrical propagation and subsequent non-uniform mechanical activation plays a role in the resulting non-uniform blood flow, perhaps in addition to contribution from the continuously changing LA compliance.

4.4.4 Measurement of Left Atrial V_p

PWV in conduit arteries have typically been measured using a time-delay in the onset of blood flow over space, which is typically clearly identifiable due to the near static blood flow patterns prior to the arrival of the pressure wave. In the LA, the onset of blood flow associated with a pressure wave is not as well defined because blood stasis is prevented by vortical flow [18]. Previously, propagation velocities in the filling ventricle and atrium have been measured based on the observation of lines of constant velocity, or isocontour lines, from spatial-temporal velocity maps [15–17]. The isocontour method results in a value of V_p that is influenced not only by delayed onset of blood flow, but also by spatial variations in blood flow. Figure 4.6 illustrates this confounding phenomenon using two synthetic spatial-temporal maps similar

to the E-wave. In the case where the onset of blood flow is uniform over space (V_p = inf) but the magnitude of the velocity-time waveform scales linearly, the measurement of an isocontour still yields a measurable V_p. Furthermore, a slower V_p results when a lower isocontour velocity value is used. V_p determined from the peak value however, results in the proper V_p = inf. When temporal delays are added to mimic non-uniform flow, a constant velocity line yields an artificially slower V_p than when measured from the time of maximum velocity. In other words, V_p measured from isocontour lines represents changes in magnitude over space in addition to non-uniform flow.

4.4.5 Limitations

The current study is limited by the temporal resolution of phase-contrast velocity images. Higher temporal resolution would allow for more accurate determination of timings. Also, temporal delays in velocity-time curves were measured as the difference in timings of the peak velocity, which is influenced by the shape of the curve if it differs in different measurement regions. The current study employed 2-dimensional acquisitions to measure blood velocity. Three-dimensional acquisitions may provide a better representation of the non-uniform flow, however, the better spatial coverage typically comes at the expense of temporal resolution and represents a longer sampling window over which the flow patterns are assumed to be identical. Finally, this study was performed on a small group of healthy volunteers. Further studies with a range of well defined pathology will be required to determine relationships between relaxation, compliance, electrical and mechanical propagation and propagation velocity.

4.4.6 Conclusions

Propagation velocity was measured in the left atrium during systole, early filling and atrial contraction. Vortical streamlines were commonly observed during systole and confounded measurements of propagation velocity during this portion of the cardiac cycle. During atrial contraction, the compliance of the chamber is continuously changing. The significance of the resulting propagation velocity may be related to this changing compliance but may also be related to the non-uniform mechanical activation of the LA myocardium. During early filling, backwards propagation was observed, in agreement with previous observations of a backwards expansion wave using wave intensity analysis (13,14). The left atrium is fully relaxed during this interval and the velocity of this wave is proposed to be related to the compliance of the chamber dictated by LA pressures. Early filling left atrial V_p thus provides a new measure of diastolic function reflecting left atrial compliance and filling pressures.

4.5 Chapter 4 References

[1] Appleton CP, Hatle LK, and Popp RL. Demonstration of restrictive ventricular physiology by Doppler echocardiography. *J Am Coll Cardiol*, 11(4):757–68, 1988.

[2] Nagueh SF, Appleton CP, Gillebert TC, Marino PN, Oh JK, Smiseth OA, Waggoner AD, Flachskampf FA, Pellikka PA, and Evangelisa A. Recommendations for the evaluation of left ventricular diastolic function by echocardiography. *Eur J Echocardiogr*, 10:165–93, 2009.

[3] Garcia MJ, Thomas JD, and Klein AL. New Doppler echocardiographic applications for the study of diastolic function. *J Am Coll Cardiol*, 32:865–75, 1998.

[4] Klein AL and Tajik AJ. Doppler assessment of pulmonary venous flow in healthy subjects and in patients with heart disease. *J Am Soc Echocardiogr*, 4:379–92, 1991.

[5] Abhayaratna WP, Seward JB, Appleton CP, Douglas PS, Oh JK, Tajik AJ, and Tsang TS. Left atrial size: physiologic determinants and clinical applications. *J Am Coll Cardiol*, 47:2357–63, 2006.

[6] Barbier P, Solomon SB, Schiller NB, and Glantz SA. Left atrial relaxation and left ventricular systolic function determine left atrial reservoir function. *Circulation*, 100:427–36, 1999.

[7] Hoit BD and Walsh RA. Regional atrial distensibility. *Am J Physiol*, 262(5 Pt 2):H1356–60, 1992.

[8] Payne RM, Stone HL, and Engelken EJ. Atrial function during volume loading. *J Appl Physiol*, 31(3):326–31, 1971.

[9] Suga H. Importance of atrial compliance in cardiac performance. *Circ Res*, 35(1):39–43, 1974.

[10] Asmar R, Benetos A, Topouchian J, Laurent P, Pannier B, Brisac AM, Target R, and Levy BI. Assessment of arterial distensibility by automatic pulse wave velocity measurement. Validation and clinical application studies. *Hypertension*, 26(3):485–90, 1995.

[11] Lehmann ED, Parker JR, Hopkins KD, Taylor MG, and Gosling RG. Validation and reproducibility of pressure-corrected aortic distensibility measurements using pulse-wave-velocity Doppler ultrasound. *J Biomed Eng*, 15(3):221–8, 1993.

[12] Tyberg JV, Davies JE, Wang Z, Whitelaw WA, Flewitt JA, Shrive NG, Francis DP, Hughes AD, Parker KH, and Wang JJ. Wave intensity analysis and the development of the reservoir-wave approach. *Med Biol Eng Comput*, 47:221–32, 2009.

[13] Flewitt JA, Hobson TN, Wang J Jr, Johnston CR, Shrive NG, Belenkie I, Parker KH, and Tyberg JV. Wave intensity analysis of left ventricular filling: application of windkessel theory. *Am J Physiol Heart Circ Physiol*, 292:H2817–23, 2007.

[14] Wang Z, Jalali F, Sun YH, Wang JJ, Parker KH, and Tyberg JV. Assessment of left ventricular diastolic suction in dogs using wave-intensity analysis. *Am J Physiol Heart Circ Physiol*, 288:H1641–51, 2005.

[15] Palecek T, Lubanda JC, Trckova R, and Linhart A. Left atrial flow

propagation velocity: a new approach for assessment of left atrial reservoir function. *Int J Cardiovasc Imaging*, 27(1):75–82, 2011.

[16] Stoddard MF, Longaker RA, and Calzada N. Left atrial inflow propagation rate: a new transesophageal echocardiographic index of preload. *J Am Soc Echocardiogr*, 15(10 Pt 1):1057–64, 2002.

[17] Stoddard MF, Calzada N, and Longaker RA. Left atrial inflow propagation rate derived by transesophageal color M-mode echocardiography is a promising index of preload. *Clin Cardiol*, 26(4):201–4, 2003.

[18] Fyrenius A, Wigstrom L, Ebbers T, Karlsson M, Engvall J, and Bolger AF. Three dimensional flow in the human left atrium. *Heart*, 86:448–55, 2001.

[19] Foll D, Taeger S, Bode C, Jung B, and Markl M. Age, gender, blood pressure, and ventricular geometry influence normal 3D blood flow characteristics in the left heart. *Eur Heart J Cardiovasc Imaging*, 2012, in press.

[20] Tsang TS, Barnes ME, Gersh BJ, Bailey KR, and Seward JB. Left atrial volume as a morphophysiologic expression of left ventricular diastolic dysfunction and relation to cardiovascular risk burden. *Am J Cardiol*, 90(12):1284–9, 2002.

[21] Nagano T, Arakawa M, Tanaka T, Yamaguchi M, Takaya T, Noda T, Miwa H, Kagawa K, and Hirakawa S. Diastolic compliance of the left atrium in man: a determinant of preload of the left ventricle. *Heart Vessels*, 5(1):25–32, 1989.

[22] De Ponti R, Ho SY, Salerno-Uriarte JA, Tritto M, and Spadacini G.

Electroanatomic analysis of sinus impulse propagation in normal human atria. *J Cardiovasc Electrophysiol*, 13(1):1–10, 2002.

[23] Dolber PC and Spach MS. Structure of canine Bachmann's bundle related to propagation of excitation. *Am J Physiol*, 257(5 Pt 2):H1446–57, 1989.

Chapter 5

Measurement and Interpretation of Left Ventricular and Left Atrial Pressure Gradients and Differences

5.1 Introduction

Non-invasively measured ventricular filling blood velocities, such as the measurement of peak early filling (E-wave) and atrial contraction (A-wave) velocities, are included in every diastolic function exam [1, 2]. Pressure gradients are an appealing alternate measure of diastolic function because they represent the forces responsible for the movement of blood. In particular, the intra-ventricular pressure gradient, perhaps more accurately referred to as the intra-ventricular pressure difference (IVPD), has been studied as a measure of left ventricular (LV) suction [3–7].

The left atrium (LA) also plays a critical role in early filling by releasing elastic energy stored in the stretched LA [8]; however, most studies do not consider pressure gradients or differences in the LA [5, 7, 9–13]. Furthermore, it is not clear that the forces applied by the ventricle or atrium are directly related

to the local pressure gradients within each chamber. The LA and the LV work together during early filling to move blood, which forms a continuous column spanning both chambers, and thus there is no obvious optimal measurement location to measure the filling pressure difference. The full atrio-ventricular pressure difference (AVPD), taking into consideration the full length of the atrium and ventricle, has not previously been characterized in comparison to the IVPD measured in the ventricle only.

It is hypothesized in this study that the exclusion of the LA from representations of filling pressure gradients is not well justified. The aims of this study are (1) to characterize the spatial dependence of early diastolic pressure gradients and resulting pressure differences over the length of the LV and extending into the LA, (2) to measure pressure gradients and differences in subjects ranging from healthy to those with diastolic dysfunction and (3) to evaluate the added value of pressure differences beyond what is already provided by the blood velocity measures from which pressure differences are derived.

5.2 Methods

5.2.1 Study Population

All participants underwent cardiac MRI examinations for the evaluation of basic systolic and diastolic functional parameters and for the evaluation of intra-cardiac pressure gradients and differences. Subjects provided written, informed, consent and approval was received from the University of Alberta Health Research Ethics Board.

The study population included younger subjects (Group 1) with no history of cardiovascular disease ($n = 10$), subjects with impaired relaxation

(Group 2) and those with signs of elevated filling pressures (Group 3). Group 1 subjects are described in Chapter 2.

Group 2 and Group 3 subjects were consecutive participants from an ongoing clinical study of heart failure with preserved ejection fraction (Alberta HEART) and a study of heart transplant recipients. Subjects were included based on diastolic parameters measured using MRI. Impaired relaxation was defined as depressed E-wave velocity < 50 cm/s, E/A ratio < 1 and normal ratio of E-wave peak blood velocity to peak annular tissue velocity (E/E') < 8. Elevated filling pressures (pseudonormal or restricted filling) was defined as normal E-wave velocity > 50 cm/s but with $E/E' > 8$ and LA volume index > 53 ml/m^2. The LA volume index > 53 ml/m^2 cutoff was based on the upper limit of the 95% confidence interval measured by Maceira et al. in 120 healthy subjects using MRI [14].

5.2.2 Data Acquisition

MRI examinations were performed on a 1.5 T scanner (Sonata; Siemens Healthcare, Erlangen, Germany). Image acquisitions were electrocardiogram-gated and performed during breath holds. SSFP cines were acquired in the 2-, 3- and 4-chamber slice orientations and a short-axis stack with full coverage of the LV. Typical imaging parameters were: 1.3 ms echo time (TE), 2.6 ms repetition time (TR), 144×256 matrix, 51° flip angle, 300×400 mm field of view (FOV), 8 mm slice thickness, 2 mm gap between short-axis slices, 238 kHz bandwidth (BW), rate 2 parallel imaging (GRAPPA) and 10–14 views per segment (VPS) for an acquired temporal resolution of 29–40 ms, reconstructed to 30 phases over the cardiac cycle.

Linear tagging, applied perpendicular to the LV long axis, or grid tags were acquired in the 4-chamber slice orientation. The acquisition was prospec-

tively gated and typical imaging parameters were: 2.8 ms TE, 3.6 ms TR, 97×192 matrix, 14° flip angle, 275×400 mm FOV, 8 mm slice thickness, 8 mm spacing between slices, 8 mm spacing between tags, 58 kHz BW, 7 VPS for a temporal resolution of 25 ms per cardiac phase.

Blood velocity time-curves and pressure gradient and differences were determined using phase contrast blood velocity imaging. For phase contrast imaging, both in-plane directional components of velocity were acquired in the 4-chamber slice orientation with each velocity direction acquired separately. Typical image acquisition parameters used were: 2.6–3.4 ms TE, 5.1–6.3 ms TR, 68×128 matrix, 20° flip angle, 1.34 m/s velocity encoding, 293×360 mm FOV, 8 mm slice thickness, 58–114 kHz BW, 2–5 VPS and a temporal resolution of 30–63 ms, reconstructed to 64 cardiac phases.

5.2.3 Data Analysis

All data analysis was performed off-line (Matlab; Mathworks, Natick, USA). LV volumes were determined by manually tracing the LV chamber in short axis SSFP slices and applying disk summation according to Simpson's rule. 2-, 3- and 4-chamber long axis slices were used to identify the LV apex and base to allow for the fractional inclusion of slices. This technique is described in further detail in Section 2.2.3 of Chapter 2. The early diastolic mitral annular velocity was determined from 4-chamber tagging cines by manually tracking myocardial tags at the LV base on the lateral wall for each cardiac phase. The tag position was then differentiated with respect to time to obtain E'. Blood velocity at the mitral valve leaflet tips was determined from phase contrast velocity maps in the 4-chamber view. The direction of blood flow was approximated using a vector blood velocity map as shown in Figure 5.1. Mitral filling velocity was calculated as the velocity along the direction of the

indicated line averaged over pixels within a 0.5 cm radius of the manually selected measurement location (white circle in Figure 5.1).

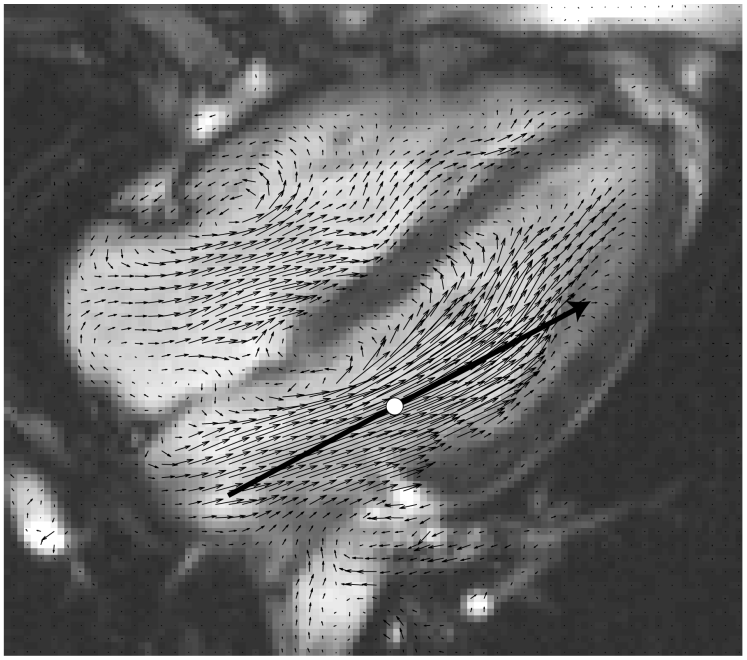

Figure 5.1: Velocity vectors for a 4-chamber image of the heart during an early filling cardiac phase. The large arrow indicated the manually estimated direction of blood flow and the white circle indicates the mitral valve leaflet tips measurement location.

Determination of Pressure Gradients and Differences

The pressure gradient field was calculated in the 4-chamber view from the 2-dimensional velocity map using the Euler equations:

$$\frac{\partial P}{\partial x} = -\rho \left[\frac{\partial v_x}{\partial t}\right] - \rho \left[v_x \cdot \frac{\partial v_x}{\partial x} + v_y \cdot \frac{\partial v_x}{\partial y}\right] \tag{5.1}$$

$$\frac{\partial P}{\partial y} = -\rho \left[\frac{\partial v_y}{\partial t}\right] - \rho \left[v_x \cdot \frac{\partial v_y}{\partial x} + v_y \cdot \frac{\partial v_y}{\partial y}\right] \tag{5.2}$$

where $\frac{\partial P}{\partial x}\hat{\mathbf{x}} + \frac{\partial P}{\partial y}\hat{\mathbf{y}}$ is the pressure gradient, P is pressure, ρ is the density of blood, t is time, x and y are the 2 spatial dimensions, and v_x and v_y are the x and y directional components of velocity [15, 16]. The resulting pressure

gradient at each point in space, (x, y), has an inertial term, related to the change in pressure over time:

$$\left(-\rho\left[\frac{\partial v_x}{\partial t}\right]\right)\hat{\mathbf{x}} + \left(-\rho\left[\frac{\partial v_y}{\partial t}\right]\right)\hat{\mathbf{y}} \tag{5.3}$$

and a convective term, related to the changes in pressure over space:

$$\left(-\rho\left[v_x \cdot \frac{\partial v_x}{\partial x} + v_y \cdot \frac{\partial v_x}{\partial y}\right]\right)\hat{\mathbf{x}} + \left(-\rho\left[v_x \cdot \frac{\partial v_y}{\partial x} + v_y \cdot \frac{\partial v_y}{\partial y}\right]\right)\hat{\mathbf{y}} \tag{5.4}$$

The pressure difference between 2 specified points as a function of time was calculated as the integral of the pressure gradient along a path connecting these 2 points. The intra-ventricular pressure difference was defined as the pressure difference along the LV length, and the atrio-ventricular pressure difference was defined as the pressure difference along the full LA and LV length. The pressure difference can also be divided into inertial and convective contributions.

To characterize the spatial dependence of pressure differences, the pressure difference was determined as a function of a variable path length defined by a stationary endpoint at the LV apex (a, in Figure 5.2A) and a variable endpoint (b, in Figure 5.2A). The variable endpoint location ranged from the LV apex to the top of the LA in the 4-chamber view of the heart. The sensitivity of the early filling peak pressure difference on the longitudinal placement of the variable endpoint was calculated as the percent change in the peak value per unit distance. This sensitivity was used to represent a measure of potential error associated with variations in user-selected spatial locations.

5.2.4 Representation of Data and Statistical Analysis

All graphical representations of data show the mean value averaged over all subjects with error bars indicating the standard deviation of the groups. Error bars are shown at times or spatial locations near the measurement points but with offsets for the clarity of presentation. Values are represented as mean $\pm$ standard deviation. To evaluate the incremental value of pressure gradients, the peak IVDP and AVPD were correlated with peak early filling velocity.

5.3 Results

Blood velocity parameters (E-wave peak velocity, E/A ratio, DT) and E/E' for Group 1 agreed with normal age-matched Dopper-derived measurements [1] and LA volumes were within the normal range of MRI-derived LA volume measurements [14, 17]. Seven of the Group 3 subjects did not have A-waves as a result of heart transplantation. A-wave measurements are thus not reported for this group. Subject population characteristics are summarized in Table 5.1.

Averaged pressure difference-time curves during early filling for Group 1 subjects are shown in Figure 5.2 for sample path lengths from the LV apex to variable endpoint locations spaced 1 cm apart. The variable endpoints for displayed curves were the mitral valve leaflet tips (MV), 1 and 2 cm into the LA ($A1$, $A2$) and 1 and 2 cm into the LV ($V1$, $V2$). Inertial and convective components are shown in panels C and D, respectively. Also shown in the same plots is the average mitral blood velocity-time curve at the leaflet tips to illustrate the temporal relationship between inflow and pressure differences.

The peak value of the pressure difference-time curves and inertial and convective contributions as a function of path length is shown in Figure 5.3.

Table 5.1: Subject characteristics

	Group 1	Group 2	Group 3
Sex, m/f	6/4	12/8	7/3
Age, y	28 ± 4	63 ± 8	55 ± 19
Height, cm	174 ± 6	171 ± 8	171 ± 6
Weight, kg	71 ± 9	89 ± 14	77 ± 9
BSA, m^2	1.8 ± 0.1	2.0 ± 0.2	1.9 ± 0.1
Heart rate, bpm	56 ± 7	59 ± 8	80 ± 18
EF, %	61 ± 3	50 ± 11	36 ± 17
E, cm/s	66 ± 9	36 ± 8	73 ± 18
E/A	2.6 ± 0.8	0.8 ± 0.2	—
DT, ms	164 ± 17	219 ± 72	134 ± 73
E/E'	3 ± 1	6 ± 2	12 ± 3
LA volume, ml	81 ± 22	93 ± 32	222 ± 105
LA volume index, ml/m^2	44 ± 11	46 ± 14	118 ± 55

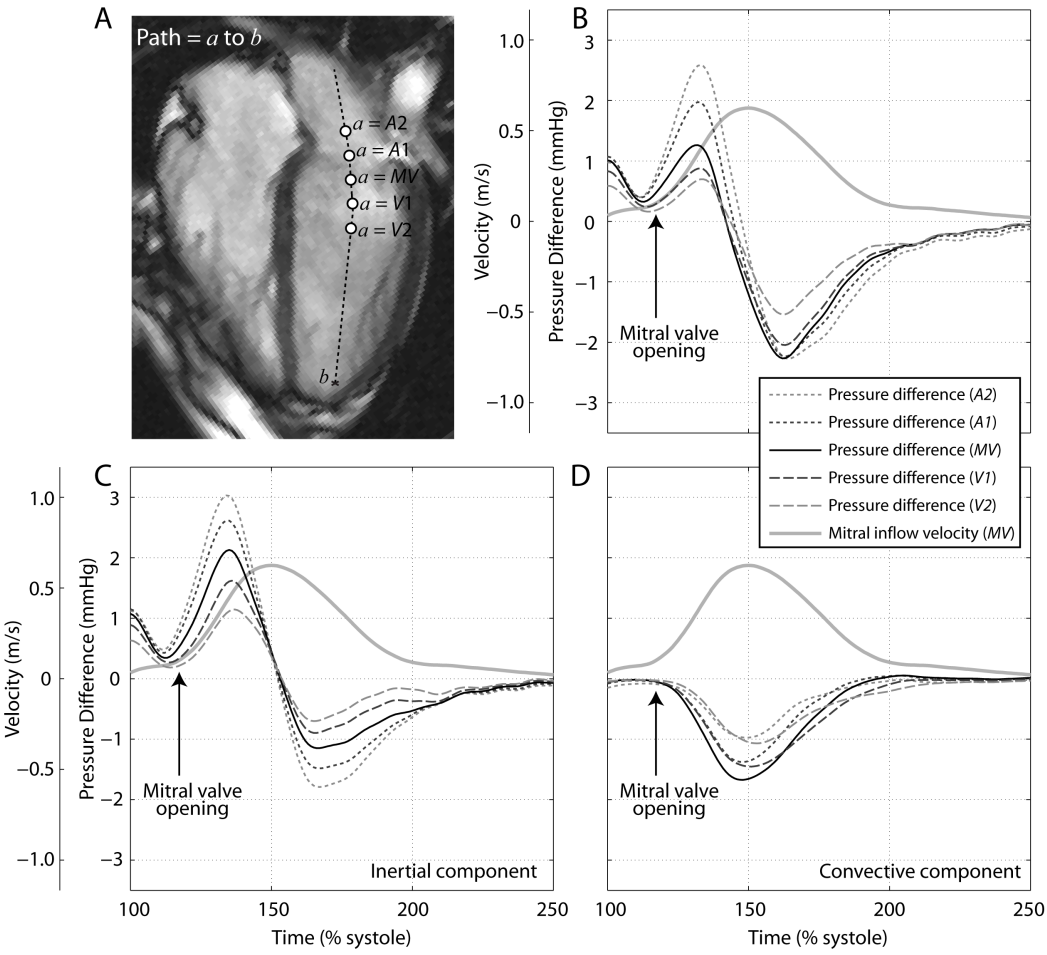

Figure 5.2: Early filling pressure difference time-curves for Group 1. Pressure differences are shown for the LV apex to the mitral valve leaflet tips (MV), 1 and 2 cm into the left atrium ($A1$, $A2$) and 1 and 2 cm into the left ventricle ($V1$, $V2$) for (A) the total pressure difference and (B) the inertial and (C) convective contributions.

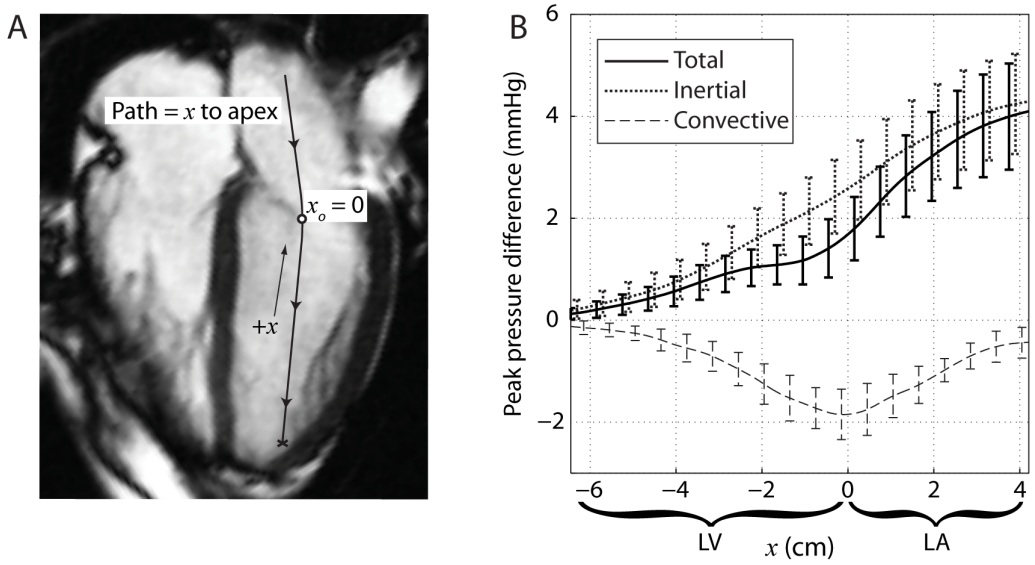

Figure 5.3: Peak early filling pressure difference as a function of path length.

The peak values for the IVPD and for AVPD are shown in Table 5.2 for all groups. The peak value of the convective component for the full path is not included in Table 5.2 because it oscillates close to zero with no well defined peak. Also shown in the table are the sensitivities of these values resulting from longitudinal displacement of the basal endpoint, representing measurement error or variability of path selection.

The relationships of the IVPD and AVPD with peak E-wave velocity is shown in Figure 5.4A. For the intra-ventricular pressure difference, the relationships of inertial and convective contributions with E-wave velocity are shown in panel B. For the atrio-ventricular pressure difference, the convective contribution is minimal and the inertial contribution resembles the total pressure difference.

Table 5.2: Atrio-ventricular and intra-ventricular pressure differences

	Group 1	Group 2	Group 3
Peak			
AVPD, mmHg	4.2 ± 1.1	1.7 ± 0.5	4.6 ± 1.5
IVPD, mmHg	1.7 ± 0.6	1.0 ± 0.3	1.9 ± 0.6
Sensitivity of peak			
AVPD, %/cm	3 ± 4	3 ± 3	3 ± 1
IVPD, %/cm	46 ± 18	36 ± 14	55 ± 22
Peak inertial			
AVPD, mmHg	4.4 ± 1.1	1.7 ± 0.5	4.8 ± 1.4
IVPD, mmHg	2.6 ± 0.8	1.3 ± 0.3	2.8 ± 0.9
Sensitivity of inertial			
AVPD, %/cm	3 ± 2	2 ± 3	2 ± 1
IVPD, %/cm	22 ± 7	14 ± 8	25 ± 10
Peak convective			
AVPD, mmHg	—	—	—
IVPD, mmHg	-1.8 ± 0.6	-0.5 ± 0.3	-1.9 ± 1.1
Sensitivity of convective			
AVPD, %/cm	—	—	—
IVPD, %/cm	-6 ± 12	-12 ± 217	-50 ± 33

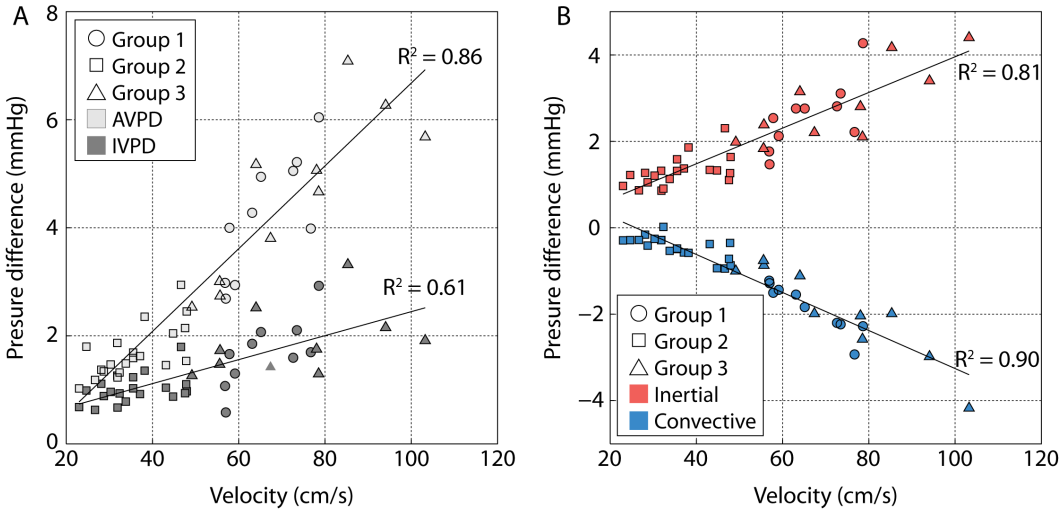

Figure 5.4: The relationship between pressure differences and blood velocity during early filling. Correlations with peak E-wave filling velocity with (A) the IVPD and AVPD and (B) the inertial and convective contribution to the IVPD.

5.4 Discussion

The major findings of the current study are: (1) the intra-ventricular pressure difference is highly sensitive to measurement error based on the choice of LV base and the atrio-ventricular pressure difference is much less sensitive to measurement error, and (2) peak intra-ventricular and atrio-ventricular pressure differences during early filling reflect peak filling velocity values.

5.4.1 Error due to Measurement Location

Previously, early diastolic pressure differences have been measured over the length of the LV by spatially integrating the pressure gradient field from the LV apex to base [5, 7, 9–13]. However, as shown in Figure 5.3, the peak magnitude of the early diastolic IVPD is most sensitive to the selection of the basal LV location. The average slope of the curve at this path length was 0.7 ± 0.2 mmHg/cm, 0.3 ± 0.1 mmHg/cm and 1.0 ± 0.4 mmHg/cm for Group 1, 2 and 3, respectively, at the mitral leaflet tips, which translates to a substantial measurement sensitivity of $46 \pm 18\%$ per cm, $36 \pm 14\%$ per cm and $55 \pm 22\%$ per cm. In contrast, the AVPG, a whole heart assessment of filling pressure differences, had a much lower positional sensitivity (Group 1: $3 \pm 4\%$ per cm, Group 2: $3 \pm 3\%$ per cm, Group 3: $3 \pm 1\%$ per cm). For comparison, a previous study has shown that the magnitude of the IVPD is relatively insensitive to the lateral location (i.e. placement within the mitral orifice) and angulation of the integration path, with a variation of only 0.26 mmHg over the central 1.8 cm region ($< 10\%$/cm) and 0.18 mmHg for angular misalignment of 20°, if only a single velocity direction is acquired, as can be the case in Doppler imaging [11].

5.4.2 Significance of AVPD and IVPD

While it is commonly stated or implied that the IVPD measured within the LV cavity represents the early diastolic ventricular forces [5, 7, 9–13], it is well known that filling velocities within the LV cavity and the IVPD itself is dependent on the LA filling pressure [12]. It is thus more likely that pressure gradients throughout the LA and LV are dependent on both the atrial contribution (push) and ventricular suction mechanisms. The findings of the current study support this hypothesis; LV pressure differences were similar in value between Group 1 and Group 3 subjects despite impaired left ventricular diastolic function (Table 5.2). For Group 3 subjects, the normalization of the pressure difference likely reflects increased LA pressures (as indicated increased E/E', reduced DT) which also result in normalized blood velocity values. In fact, pressure differences and early filling blood velocity were found to be highly correlated (Figure 5.4). In contrast, Group 2 subjects had decreased LV pressure differences (Table 5.2), again reflecting decreased blood velocity values (Figure 5.4).

5.4.3 Convective and Inertial Contributions

Common measures of diastolic function (E/A, DT) are derived from velocity-time curves and few measures consider spatial patterns of blood flow. While the inertial contribution to the pressure difference is related to the change in velocity over time, the convective contribution is related to the change in velocity over space. The convective component thus has the potential to provide a measure of diastolic function that characterizes spatial patterns of blood flow. In this study however, the convective component of the IVPD was found to be closely related to the peak E-wave velocity and was found

to approach 0 for the AVPD, again suggesting limited additional value of the convective IVPG or AVPG.

The calculation of the integrated pressure difference hides spatial patterns in the pressure gradient. A study by Yotti et al. studied the convective contribution to the intra-ventricular pressure gradient along the length of the LV and found that patients with dilated cardiomyopathy had increasing values nearer to the mitral valve compared to controls with more constant values along the length of the LV [7]. Thus it is possible that the convective component of the pressure gradient, and not the pressure difference, may provide insight into diastolic function.

5.4.4 Limitations

The current study is limited by the 30-63 ms temporal resolution of the phase contrast MRI sequence. The lower temporal resolution velocity data has the potential to underestimate the pressure gradients based on the need to differentiate velocity with respect to time for the calculation of the inertial component of the IVPD [16].

A limitation of this study is the age discrepancy between Group 1 subjects and Groups 2 and 3 subjects. Furthermore, Groups 2 and 3 are a heterogeneous population. Notably, E/A could not be determined for heart transplant recipients with no A-wave. The goals of this study however, were not to evaluate cardiac dysfunction in specific patient groups, but were instead to examine the behaviour of the IVPD and AVPD in a broader context. The excellent correlation between peak E-wave velocity and pressure differences suggests that this relationship and the conclusions drawn can be extended to a wide patient population.

5.4.5 Conclusions

Pressure differences were characterized throughout the left ventricle and into the left atrium in healthy controls and in those with impaired relaxation and evidence of elevated filling pressures. Both the IVPD and AVPD were found to be closely correlated with the E-wave peak velocity in all groups. The E-wave is well known to be dependent on diastolic preload and filling pressures. In particular, in the group with elevated filling pressures, the E-wave peak velocity increases in concert with the peak IVPD and peak AVPD. These results imply that both the IVPD and AVPD are dependent on mechanisms of ventricular suction and atrial push.

It was also found that peak pressure difference measures are most sensitive to the selection of the LV base. Given the substantially smaller measurement sensitivity of filling pressure differences on the integration path by including both the LA and LV cavities (approximately 15 times less sensitive), it is preferable that both chambers be included in these measurements.

5.5 Chapter 5 References

[1] Nagueh SF, Appleton CP, Gillebert TC, Marino PN, Oh JK, Smiseth OA, Waggoner AD, Flachskampf FA, Pellikka PA, and Evangelisa A. Recommendations for the evaluation of left ventricular diastolic function by echocardiography. *Eur J Echocardiogr*, 10:165–93, 2009.

[2] Oh JK, Seward JB, and Tajik AJ. Assessment of Diastolic Function. In *The Echo Manual*, pages 45–57. Lippincott Williams and Wilkins, Philadelphia, second edition, 1999.

[3] Nikolic SD, Feneley MP, Pajaro OE, Rankin JS, and Yellin EL. Origin of regional pressure gradients in the left ventricle during early diastole. *Am J Physiol*, 268:H550–7, 1995.

[4] Firstenberg MS, Greenberg NL, Garcia MJ, and Thomas JD. Relationship between ventricular contractility and early diastolic intraventricular pressure gradients: a diastolic link to systolic function. *J Am Soc Echocardiogr*, 21:501–6, 2008.

[5] Rovner A, Greenberg NL, Thomas JD, and Garcia MJ. Relationship of diastolic intraventricular pressure gradients and aerobic capacity in patients with diastolic heart failure. *Am J Physiol Heart Circ Physiol*, 289:H2081–8, 2005.

[6] Rovner A, de las Fuentes L, Waggoner AD, Memon N, Chohan R, and Dvila-Romn VG. Characterization of left ventricular diastolic function

in hypertension by use of doppler tissue imaging and color m-mode techniques. *J Am Soc Echocardiogr*, 19:872–9, 2006.

[7] Yotti R, Bermejo J, Antoranz JC, Desco MM, Cortina C, Rojo-Alvarez JL, Allu C, Martn L, Moreno M, Serrano JA, Muoz R, and Garca-Fernndez MA. A noninvasive method for assessing impaired diastolic suction in patients with dilated cardiomyopathy. *Circulation*, 112:2921–9, 2005.

[8] Suga H. Importance of atrial compliance in cardiac performance. *Circ Res*, 35(1):39–43, 1974.

[9] Asada-Kamiguchi J, Jones M, Greenberg NL, Popovic ZB, Tsujino H, Zetts AD, Qin JX, Garcia MJ, Thomas JD, and Shiota T. Intraventricular pressure gradients in left ventricular aneurysms determined by color M-mode Doppler method: an animal study. *J Am Soc Echocardiogr*, 19:1112–8, 2006.

[10] Firstenberg MS, Smedira NG, Greenberg NL, Prior DL, McCarthy PM, Garcia MJ, and Thomas JD. Relationship between early diastolic intraventricular pressure gradients, an index of elastic recoil, and improvements in systolic and diastolic function. *Circulation*, 104:I330–5, 2001.

[11] Greenberg NL, Vandervoort PM, Firstenberg MS, Garcia MJ, and Thomas JD. Estimation of diastolic intraventricular pressure gradients by Doppler M-mode echocardiography. *Am J Physiol Heart Circ Physiol*, 280:H2507–15, 2001.

[12] Popovic ZB, Prasad A, Garcia MJ, Arbab-Zadeh A, Borowski A, Dijk E, Greenberg NL, Levine BD, and Thomas JD. Relationship among diastolic

intraventricular pressure gradients, relaxation, and preload: impact of age and fitness. *Am J Physiol Heart Circ Physiol*, 290:H1454–9, 2006.

[13] Rovner A, Smith R, Greenberg NL, Tuzcu EM, Smedira N, Lever HM, Thomas JD, and Garcia MJ. Improvement in diastolic intraventricular pressure gradients in patients with hocm after ethanol septal reduction. *Am J Physiol Heart Circ Physiol*, 285:H2492–9, 2003.

[14] Maceira AM, Cosn-Sales J, Roughton M, Prasad SK, and Pennell DJ. Reference left atrial dimensions and volumes by steady state free precession cardiovascular magnetic resonance. *J Cardiovasc Magn Reson*, 12:65, 2010.

[15] Ebbers T, Wigstrom L, Bolger AF, Wranne B, and Karlsson M. Non-invasive measurement of time-varying three-dimensional relative pressure fields within the human heart. *J Biomech Eng*, 124:288–93, 2002.

[16] Thompson RB and McVeigh ER. Fast measurement of intracardiac pressure differences with 2d breath-hold phase-contrast mri. *Magn Reson Med*, 49:1056–66, 2003.

[17] Hudsmith LE, Petersen SE, Francis JM, Robson MD, and Neubauer S. Normal human left and right ventricular and left atrial dimensions using steady state free precession magnetic resonance imaging. *J Cardiovasc Magn Reson*, 7:775–82, 2005.

Chapter 6

MRI Determination of Global Surface Strains Using SSFP Cines: A Comparison with Tissue Tagging[1]

6.1 Introduction

Left ventricular (LV) ejection fraction (EF) is the most commonly reported measure of cardiac performance. However, it is now widely accepted that abnormalities in morphology and function may exist despite preserved LVEF. Specifically, changes in global LV longitudinal strain have been shown to exist without detectable changes in circumferential strain or LVEF, in hypertensive patients with heart failure [1], heart transplant patients [2], type 2 diabetic patients [3], aortic regurgitation [4], hypertrophic cardiomyopathy [5], Fabry disease [6, 7] and cardiotoxicity in patients undergoing anthracycline and trastuzumab breast cancer therapy [8, 9]. Global longitudinal strain has also been shown to be a better predictor than wall motion score index or

[1] A version of this chapter has been submitted for review: Cheng-Baron J, Chow K, Pagano JJ, Paterson DI, Oudit GY, Thompson RB. MRI Determination of Global Surface Strains Using SSFP Cines: A Comparison with Tissue Tagging. *Magn Res Med*. Submitted October 10, 2012.

LVEF for all-cause mortality [10].

Echocardiography is routinely used to measure strain using techniques such as tissue Doppler [11] and speckle tracking [12] due to the rapid data acquisition and post-processing methods, often reporting the average or global strains [1–8, 10]. Strain measurement using MRI tissue tagging [13–16], phase contrast imaging [17], displacement-mapping [18] or direct strain mapping [19] is not routine in clinical MRI due to the necessity for additional data acquisition and potentially onerous post-processing. Recently, feature tracking algorithms have been applied to MRI steady-state free precession (SSFP) cines to obtain myocardial tissue deformation without the acquisition of additional tagged or otherwise encoded images, although specialized software is necessary to perform the tracking [20–22] and inter-study reproducibility based on coefficient of variation (COV) and interclass correlation coefficient (ICC) has been shown to be inadequate to measure small changes in strain (COV/ICC = 20.3%/0.70 circumferentially and 26.4%/0.44 longitudinally) [23].

In this chapter, an alternative method is proposed for the determination of peak global systolic longitudinal, circumferential and radial strains based on traditional LV volume analysis using standard SSFP imaging with minimal additional post-processing and without tissue tracking algorithms. The proposed strains, measured on the endocardial and epicardial surfaces, are compared to a conventional tissue tagging method in a validation group comprising subjects with a wide range of myocardial function. The ability of the surface strain method to detect abnormalities in myocardial strain in the setting of normal LVEF was evaluated in a group of patients with Fabry disease, a condition in which strain abnormalities and preserved ejection fraction have been measured [6, 7].

6.2 Methods

6.2.1 Study Population

All studies from which subjects were included had protocols approved by the University of Alberta Research Ethics Board and all subjects provided written, informed consent.

Surface Strain Validation Group

Subjects included were consecutive participants enrolled in an ongoing clinical study of heart failure (Alberta Heart Failure Etiology and Analysis Research Team; Alberta HEART) comprising healthy individuals and those diagnosed with diabetes, obesity, hypertension, atrial fibrillation, coronary artery disease or heart failure, and in whom tagging data was acquired. The subject population ($n = 48$) was selected to have a wide range of expected myocardial strain in order to study the performance of the proposed surface strain method across a wide range of cardiac function and in a diverse clinical population.

Surface Strain in Fabry Disease versus Matched Healthy Controls

Surface strain analysis was performed on a group of patients with Fabry disease ($n = 11$) with preserved LVEF ($> 55\%$) and in a healthy control group, with no history of cardiovascular disease. The control group ($n = 11$) was selected by matching age, gender and LVEF to the patients with Fabry disease.

6.2.2 Data Acquisition

All subjects underwent cardiac MRI examinations on a 1.5 T scanner (Sonata; Siemens Healthcare, Erlangen, Germany). Image acquisitions were performed during breath-holding at end-inspiration and were electrocardiogram-gated. SSFP cine imaging included a short axis stack spanning the length of the LV and 2-, 3- and 4-chamber long axis slices. Typical imaging parameters were: 1.3 ms echo time (TE), 2.6 ms repetition time (TR), 144×256 matrix, 51° flip angle, 300×400 mm field of view (FOV), 8 mm slice thickness, 2 mm gap between short-axis slices, 238 kHz bandwidth (BW), rate 2 GRAPPA parallel imaging, and 10–14 views per segment (VPS) for an acquired temporal resolution of 29–40 ms, reconstructed to 30 phases over the cardiac cycle.

For tissue tagging analysis, grid tags were applied on 3 short axis slices (base, mid and apex locations) and a 4-chamber long axis slice. Typical imaging parameters were: TE = 2.8 ms, TR = 3.6 ms, 97×192 matrix, 14° flip angle, 275×400 mm FOV, 8 mm slice thickness, 12 mm between slices, 8 mm spacing between tags, 59 kHz BW, 7 VPS for a temporal resolution of 25 ms per cardiac phase.

6.2.3 Surface Strain Analysis

All data analysis was performed off-line (MATLAB; The MathWorks, Natick, USA). LV volumes and masses were measured from SSFP cines using method of disks described in Section 2.2.3 of Chapter 2, similar to other published methods [24, 25]. In brief, contours were traced manually on short axis slices with papillary muscles and trabeculation excluded from the myocardium. The LV base and apex were identified on long axis views to further define the extent of the LV chamber and cubic spline interpolation was applied between

short axis slices to a resolution of 1 mm in the longitudinal direction and 10° in the circumferential direction (Figure 6.1). The resulting three-dimensional casts of the left ventricle at end-diastole and end-systole were used to calculate LV mass and volumes.

Changes in the dimensions of the endocardial and epicardial surfaces from end-diastole to end-systole were used to calculate peak systolic global circumferential strain (E_{cc}), longitudinal strain (E_{ll}), and radial strain (E_{rr}). Breath-hold inconsistencies between short axis slice acquisitions result in an in-plane (lateral) shift. To re-align slices prior to the calculation of surface strains, a moving average filter spanning 5 slices was applied to the coordinates of the centers of mass of the traced myocardium.

Strain is defined as the fractional change in the distance between 2 points referenced to the initial length. In the heart, for end-systolic strain, this can be expressed as:

$$\epsilon = \frac{d(ES) - d(ED)}{d(ED)} \tag{6.1}$$

where ϵ is regional strain, d is the distance between 2 material points, ES is end-systole and ED is end-diastole. Average strain can thus be calculated as:

$$E = \frac{1}{n}\sum_{i=1}^{n}\epsilon_i = \frac{1}{n}\sum_{i=1}^{n}\frac{d_i(ES) - d_i(ED)}{d_i(ED)} \tag{6.2}$$

where n is the number of pairs of fixed points. If evenly spaced points are chosen at end-diastole, $d(ED)$ is the same for all pairs of points and Equation 6.2 reduces to:

$$E = \frac{[\sum_{i=1}^{n} d_i(ES)] - nd(ED)}{nd(ED)} \tag{6.3}$$

Figure 6.2 shows a conceptual example of calculating average strain over

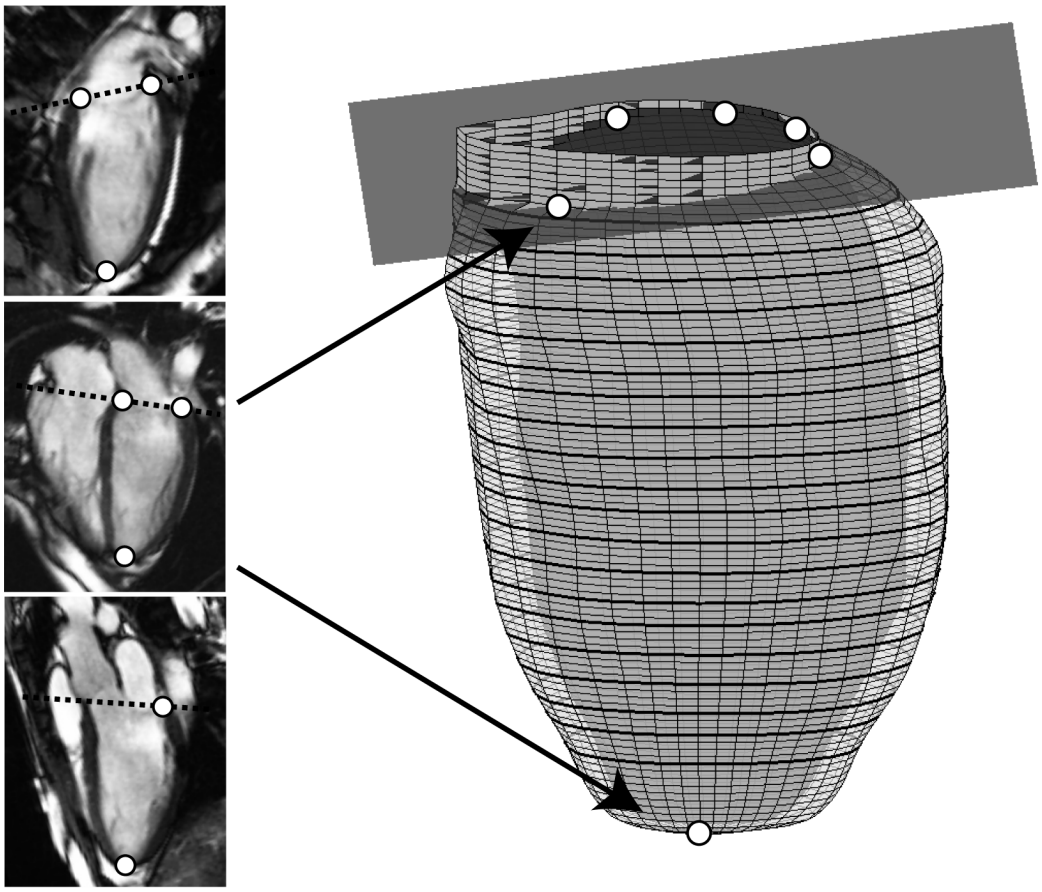

Figure 6.1: Interpolated 3-dimensional representation of the left ventricle at end-diastole. Long axis views of the heart were used to define the LV base as a plane and the LV apex as a point.

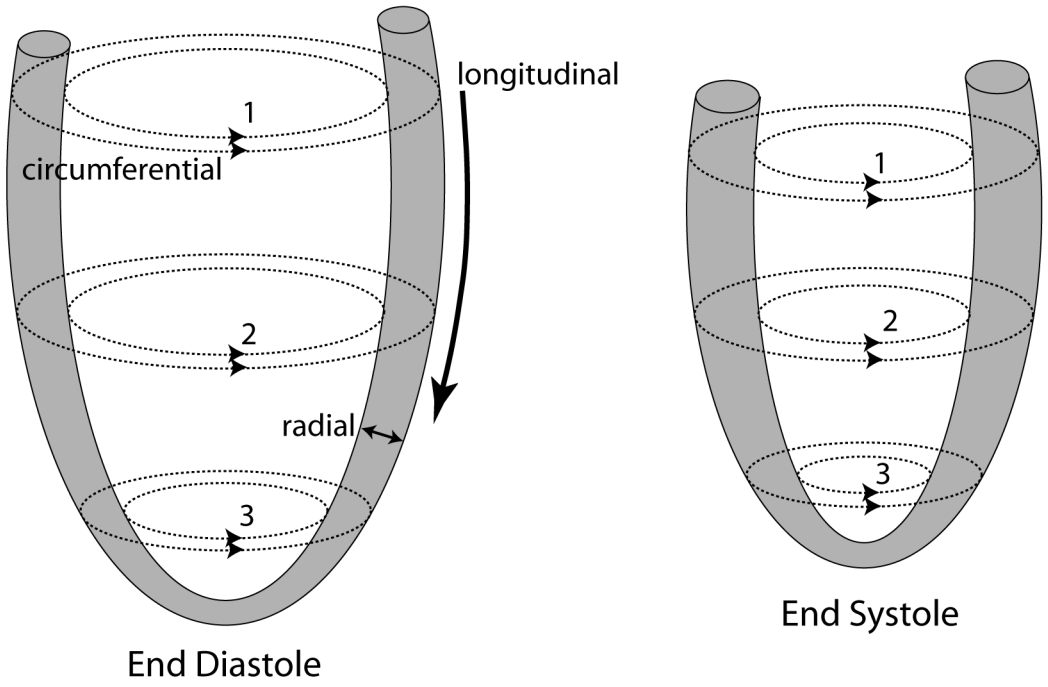

Figure 6.2: Two-dimensional schematic of the left ventricle at end diastole and end systole. Examples of 3 circumferential lengths at end-diastole and the same locations at end-systole are shown. Longitudinal and radial directions are indicated.

3 circumferential lines evenly spaced at end-diastole. The following calculations are preformed independently on both the endocardium and epicardium. In this example, $nd(ED)$ is the sum of the 3 circumferential lengths; more apical paths are weighted less due to their shorter lengths. At end-systole, these lines have moved closer together due to longitudinal shortening as shown in Figure 3, and $\sum_{i=1}^{n} d_i(ES)$ is the sum of the 3 end-systolic circumferential lengths. Under this representation, Equation 6.3 can be expressed as:

$$E = \frac{\sum_{j-1}^{N} L_j(ES) - \sum_{j-1}^{N} L_j(ED)}{\sum_{j=1}^{N} L_j(ED)} \tag{6.4}$$

where L is each of the circumferential lengths and $N = 3$ in our example. The same calculations can be applied in the longitudinal and radial directions. Increasing the number lengths, N, will provide a more accurate estimate of

global whole heart strain.

In this study, global circumferential surface strain was calculated using a total of 20 evenly spaced circumferential lengths on both the endocardium and epicardium at end-diastole (circumferential lines in Figure 6.1). At end-systole, the locations of these lines were approximated to be evenly spaced over the end-systolic LV length. Longitudinal lengths were measured from LV base to apex at 10° intervals ($N = 36$) around the LV (longitudinal lines in Figure 6.1), for both end-systole and end-diastole. Radial lengths were measured from endocardium to epicardium. Endocardial endpoints were the intersection of endocardial circumferential and longitudinal lengths ($N = 20 \times 36 = 72$). For each endocardial point, the radial length was then measured as the shortest distance from this point to the epicardium. Circumferential, longitudinal and radial directions are shown in Figure 6.2. To calculate peak systolic strain from the measured lengths, the following strain equations were applied:

$$E_{ll_s} = \frac{\sum L_{ll_s}(ES) - \sum L_{ll_s}(ED)}{\sum L_{ll_s}(ED)} \tag{6.5}$$

$$E_{cc_s} = \frac{\sum L_{cc_s}(ES) - \sum L_{cc_s}(ED)}{\sum L_{cc_s}(ED)} \tag{6.6}$$

$$E_{rr} = \frac{\sum L_{rr}(ES) - \sum L_{rr}(ED)}{\sum L_{rr}(ED)} \tag{6.7}$$

where s = endocardium, epicardium. Equations 6.5–6.7 result in a total of 5 peak systolic global strain values: $E_{cc_{endo}}$, $E_{cc_{epi}}$, $E_{ll_{endo}}$, $E_{ll_{epi}}$ and E_{rr}. Endocardial and epicardial strains were averaged to represent mean myocardial strain $E_{cc_{avg}}$ and $E_{ll_{avg}}$.

For the purposes of an additional comparison with tagging-derived strains, E_{cc} and E_{ll} were also calculated using a subset of the measured lengths. Tagging-derived strains use only information from the 3 short axis and 1 long

axis slice orientations, and thus, surface strain calculations were modified to match the spatial coverage of tagging data for a second comparison. Using the interpolated volume with 1 mm spacing between circumferential locations, the 3 circumferential lengths closest to the 3 acquired short axis tagging slices were used to calculate E_{cc}. Similarly, for E_{ll}, the 2 longitudinal lengths in the plane closest to the 4-chamber orientation from 10° increments were used.

6.2.4 Tagging-Derived Strain Analysis

Tagged images were analyzed using custom software employing an open source image registration algorithm [26] for comparison with surface strains. Details for the analysis of strain using this method is described in Section 2.2.3 of Chapter 2 and are similar to other published methods [27]. E_{cc} was determined for each of the 3 short axis slices and E_{ll} was determined for the 4-chamber slice within a region from the sub-endocardium to sub-epicardium as defined by the user with care taken to include only myocardium. E_{rr} was not calculated due to insufficient tag resolution in the radial dimension. The average of the 3 short-axis slices ($E_{cc_{avg}}$) along with E_{ll} from the 4-chamber slice were used for comparison with the proposed surface global strains.

6.2.5 Representation of Data and Statistical Analysis

Statistical analysis was performed using SPSS Statistics 19 (IBM Software Group, Somers, NY). All values are represented as mean ± standard deviation. The range of values is also reported for the validation population used for the comparison of surface strain and tagging-derived strain methods. Statistical significance was set at 5%.

Surface Strain Validation Group

Peak global $E_{cc_{avg}}$ and $E_{ll_{avg}}$ between methods were compared using linear regression and Bland-Altman analysis. Inter- and intra-observer reproducibility for the proposed surface strain analysis was determined on a subset of 10 consecutive healthy subjects from the validation group. The data was analyzed independently by 2 observers (JC, RBT) and repeated again approximately 4 months later by one of the observers (JC) with complete retracing of all surfaces (endocardial and epicardial) and apical and basal points. Measurement reproducibility was represented as the standard deviation of the difference between the 2 measurements and as the COV of this difference. The ICC was also calculated based on a 2-way random effects model and absolute agreement for single measurements.

Surface Strain in Fabry Disease versus Matched Healthy Controls

Student's t-test was used to test for differences in general population characteristics and surface strain-derived E_{cc}, E_{ll} and E_{rr} between patients with Fabry disease and controls.

6.3 Results

Study population characteristics are shown in Table 6.1. Surface strain analysis was successful on all study participants; however, 8 subjects for the surface strain versus tagging-derived strain comparison had to be excluded due to poor tagging image quality, assessed visually, on the basis of insufficient tag persistence to end-systole and/or the presence of major artifacts that preclude image registration analysis. The final study populations included 40 subjects for the surface strain versus tagging-derived strain comparison (16 healthy, 16

heart failure, 1 diabetes only, 6 hypertension only, 1 coronary artery disease only) and 22 subjects for the Fabry disease comparison (11 patients with Fabry disease and 11 matched control subjects).

Table 6.1: Subject characteristics

		Fabry Disease Comparison	
	Validation Group	Patients	Controls
Sex, m/f	15/25	7/4	7/4
Age, yrs	64 ± 11 (38–89)	45 ± 12	45 ± 11
Height, m	1.67 ± 0.09 (1.40–1.85)	1.72 ± 0.11	1.73 ± 0.12
Weight, km	78 ± 13 (53–109)	70 ± 9	78 ± 15
BSA, m^2	1.9 ± 0.2 (1.4–2.3)	1.8 ± 0.2	1.9 ± 0.2
Heart rate, bpm	63 ± 9 (49–83)	59 ± 11	64 ± 8
LVEF, %	48 ± 13 (16–66)	63 ± 4	61 ± 2
LV EDV, ml	183 ± 83 93–444	161 ± 36	175 ± 34
LV mass, g	110 ± 41 (59–215)	180 ± 64	107 ± 28*

Values are mean ± standard deviation (range). BSA = body surface area. EDV = end-diastolic volume. * indicates $p < 0.05$ for a comparison between patients with Fabry disease and controls.

6.3.1 Surface Strain Validation

Surface strain and tagging-derived strain values are shown in Table 6.2. Surface strains are compared to tagging-derived strains for all subjects in Figure 6.3. $E_{cc_{avg}}$ showed an R^2 value of 0.86 ($p < 0.0001$) between surface strain and tagging-derived strain (Figure 6.3A). Bland-Altman analysis with linear regression ($R^2 = 0.14$, $p < 0.05$) yielded a bias of ($y = 0.16x + 1.24$)% strain with a 95% confidence interval of ±3.7 % strain (Figure 6.3B). For $E_{ll_{avg}}$, an R^2 value of 0.77 ($p < 0.0001$) was determined for the correlation between surface strain and tagging-derived strain (Figure 6.3C). Bland-Altman analysis with linear regression ($R^2 = 0.11$, $p < 0.05$) yielded a bias of ($y = 0.18x + 1.30$)% strain with a 95% confidence interval of ±4.2% strain (Figure

6.3D).

Surface strains calculated using a sub-set of measured lengths that match the slice locations of the tagging data are also shown in Table 6.2. $E_{cc_{avg}}$ was found to have an R^2 value of 0.80 ($p < 0.0001$) for correlation between the sub-set surface strain-derived and tagging-derived values. Bland-Altman analysis with linear regression ($R^2 = 0.27$, $p < 0.001$) yielded a bias of $(y = 0.28x + 3.10)\%$ strain with a 95% confidence interval of $\pm 4.7\%$ strain. For $E_{ll_{avg}}$, an R^2 value of 0.75 ($p < 0.0001$) was determined for the correlation between the sub-set surface strain-derived and tagging-derived values. Bland-Altman analysis with linear regression ($R^2 = 0.13$, $p < 0.05$) yielded a bias of $(y = 0.21x + 2.04)\%$ strain with a 95% confidence interval of $\pm 4.4\%$ strain.

Inter- and intra-observer reproducibility for the volume analysis and surface strains are shown in Table 6.3. The COV for inter-observer/intra-observer variability was 7.6/6.0% for $E_{cc_{avg}}$, 10.5/5.5% for $E_{ll_{avg}}$ and 13.8/18.2% for E_{rr}.

6.3.2 Surface Strain in Fabry Disease versus Matched Healthy Controls

For patients with Fabry disease and their matched controls, surface strain values are shown in Table 6.4. There was no statistically significant difference in LVEF as expected based on study design, and all were within the normal range [28]. $E_{cc_{endo}}$ and $E_{cc_{avg}}$ were significantly increased in magnitude for patients with Fabry disease compared to controls but $E_{cc_{epi}}$ was reduced. $E_{ll_{endo}}$, $E_{ll_{epi}}$ and $E_{ll_{avg}}$ were all reduced significantly in magnitude for patients with Fabry disease compared to controls. E_{rr} was increased in the patients with Fabry disease compared to controls.

Table 6.2: Measured strains in validation group

	Mean	Range
Circumferential strain		
Average surface strain, %	-16 ± 5	$-(26–4)$
Endocardial surface strain, %	-23 ± 8	$-(34–6)$
Epicardial surface strain, %	-10 ± 3	$-(18–3)$
Average tagging-derived strain, %	-15 ± 5	$-(22–5)$
Longitudinal strain		
Average surface strain, %	-13 ± 5	$-(21–4)$
Endocardial surface strain, %	-14 ± 5	$-(24–3)$
Epicardial surface strain, %	-13 ± 5	$-(21–3)$
4-chamber tagging-derived strain, %	-12 ± 4	$-(18–3)$
Radial strain, %	39 ± 16	(11–67)
Circumferential strain, subset		
Average surface strain, %	-16 ± 6	$-(27–1)$
Endocardial surface strain, %	-22 ± 9	$-(37–2)$
Epicardial surface strain, %	-10 ± 4	$-(21–2)$
Longitudinal strain, subset		
Average surface strain, %	-13 ± 5	$-(22–3)$
Endocardial surface strain, %	-14 ± 5	$-(24–1)$
Epicardial surface strain, %	-12 ± 5	$-(22–2)$

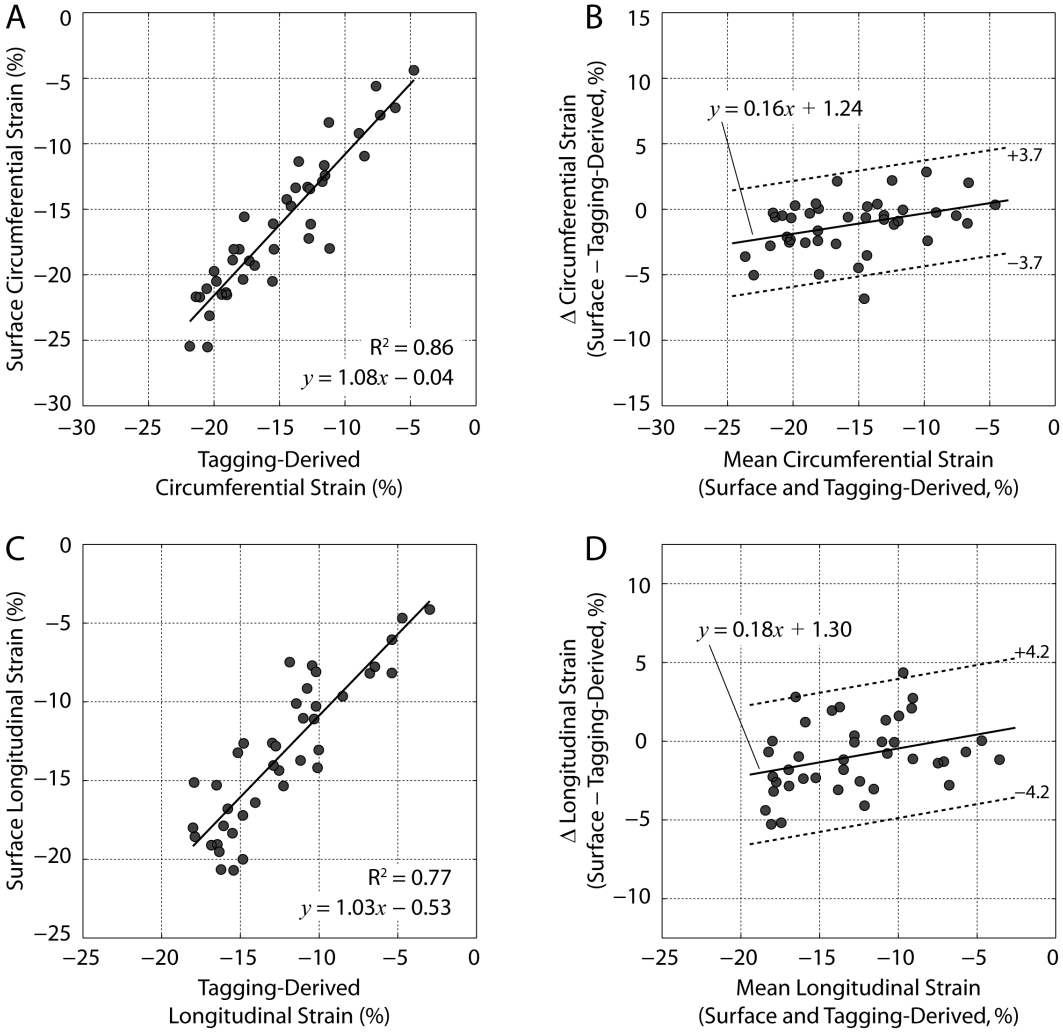

Figure 6.3: Correlations between surface strain and tagging-derived strain. Surface strain versus tagging-derived strain for (A) circumferential strain and (C) longitudinal strain are shown. Bland-Altman analysis is shown for (B) circumferential strain and (D) longitudinal strain.

Table 6.3: Inter-observer and intra-observer reproducibility for volume and surface strain

	SD of difference	COV	Interclass R
End-diastolic volume			
Inter-observer	2.2 ml	1.6%	1.00
Intra-observer	1.9 ml	1.3%	1.00
End-systolic volume			
Inter-observer	2.9 ml	4.7%	0.96
Intra-observer	2.3 ml	3.5%	1.00
Stroke volume			
Inter-observer	3.0 ml	3.8%	0.97
Intra-observer	2.0 ml	2.6%	1.00
Ejection fraction			
Inter-observer	2.5%	4.4%	0.87
Intra-observer	1.5%	2.8%	0.99
LV mass			
Inter-observer	3.1 g	3.6%	0.90
Intra-observer	5.0 g	6.0%	0.96
Circumferential endocardial strain			
Inter-observer	2.1%	7.4%	0.75
Intra-observer	1.2%	4.5%	0.98
Circumferential epicardial strain			
Inter-observer	1.5%	13.7%	0.90
Intra-observer	1.3%	11.6%	0.94
Circumferential average strain			
Inter-observer	1.5%	7.6%	0.84
Intra-observer	1.1%	6.0%	0.97
Longitudinal endocardial strain			
Inter-observer	2.3%	14.1%	0.84
Intra-observer	1.5%	9.0%	0.92
Longitudinal epicardial strain			
Inter-observer	1.8%	12.5%	0.87
Intra-observer	1.4%	9.7%	0.93
Longitudinal average strain			
Inter-observer	1.6%	10.5%	0.90
Intra-observer	0.9%	5.5%	0.97
Radial strain			
Inter-observer	7.2%	13.8%	0.69
Intra-observer	8.9%	18.2%	0.79

Table 6.4: Surface strain in fabry disease and controls

	Patients	Controls
Circumferential strain		
Average, %	-23 ± 2	-21 ± 2*
Endocardial, %	-36 ± 4	-30 ± 3*
Epicardial, %	-10 ± 2	-12 ± 1*
Longitudinal strain		
Average, %	-14 ± 4	-18 ± 2*
Endocardial, %	-15 ± 5	-20 ± 3*
Epicardial, %	-13 ± 4	-17 ± 2*
Radial strain, %	54 ± 8	46 ± 5*

* indicates $p < 0.05$ for a comparison between patients with Fabry disease and controls

6.4 Discussion

We have shown in this study that peak systolic global surface strains can be calculated from SSFP cine imaging with minimal additional post-processing and that average circumferential and longitudinal strains, calculated using the proposed surface strain method, have good agreement with tagging-derived strains. Furthermore, global surface strains were able to detect differences in myocardial function in patients with Fabry disease despite no difference in LVEF compared to controls.

6.4.1 Surface Strains Compared to Tagging-Derived Strains

The surface strains presented in this study have several advantages over tissue tagging methods. No additional data collection is required beyond conventional volumetric cine acquisitions and SSFP imaging provides excellent blood-tissue contrast and independence from factors such as tag persistence throughout cardiac phases of interest. In the current study, 8 out of 48 subjects (17%) in the validation group had inadequate tagging data as a result of poor tag persistence and/or major artifacts, whereas all subjects could be analyzed using the surface strain method. The data analysis is a minor addition to conventional volume analysis and requires only that the user identify the LV base and apex on 2-, 3- and 4-chamber long axis views. Additional automated computational time is negligible. Surface strains are also averaged over the entire heart and are thus less dependent on slice prescription [29]. The surface strain method would be equally applicable with computed tomography which offers similar high-contrast full heart coverage and where endocardial and epicardial borders can be delineated at end-systole and end-diastole.

Surface and tagging-derived strains show good agreement when comparing peak systolic global $E_{cc_{avg}}$ and $E_{ll_{avg}}$. However, some small discrepancies between the two methods remain as characterized by a non-zero bias for the Bland-Altman analysis. Surface strains tend to be slightly higher in magnitude than tagging-derived strains (Figure 6.3), particularly for subjects with larger magnitude strains. This bias was not eliminated when surface strains were re-calculated using measured lengths matching the slice locations of the tagging data, indicating that discrepancies between the two techniques do not reflect potential regional differences based on strain measurements from different slice locations.

Because endocardial strain is larger than strain in more epicardial layers, it is possible that the bias between surface strains and tagging may be due to different trans-mural myocardial regions included in the two techniques. For tagging-derived strains, the blood-tissue interface is not as clearly delineated as SSFP cines and necessitates conservative selection of myocardial regions for tracking. The resulting exclusion of the most endocardial regions would yield systematically smaller values for peak systolic strain for tissue tagging. In contrast, for surface strains, potential accidental inclusion of trabeculae is a possible source of error that may overestimate strain values [30].

Tagging-derived circumferential strain was calculated as the average of 3 short axis slices, consistent with conventional practice where strain from individual regions are directly averaged [31]. As a result, the apical slice is weighted equally with the basal slice despite its shorter length, in contrast to surface strains, where regions are weighted by their spatial extent. This difference provides another potential source of discrepancy between circumferential tagging-derived and surface strains. However, circumferential strain has been shown to be higher at apical locations [32], suggesting the opposite trend from

observations in the current study. Weighing regions by their spatial extent is physiologically meaningful because smaller regions will have a lesser impact on overall global function.

6.4.2 Relationship Between Surface Strain and Ejection Fraction

Strain and ejection fraction are similar from the perspective that strain is a fractional change in 1-dimensional length from end-diastole to end-systole and ejection fraction is the same fractional change in 3-dimensional volume. Given that LV volume is defined by the endocardial border, it follows that ejection fraction is ultimately determined by endocardial strain. To evaluate the relationship between measured strains and ejection fraction, LV volume (V) can be modeled as a general class of shapes with a circular cross-section:

$$V = klc^2 \tag{6.8}$$

where k is a geometric factor, l is the long axis length and c is the circumference. This expression applies to ellipsoids, spheres, cylinders, cones or any combination of these shapes (eg. cylinder connected to a half-sphere) [33]. Thus, changes in volume (LVEF) are related linearly to changes in longitudinal length and quadratically to changes in circumferential length [34], and thus, $E_{cc_{endo}}$ dominates the determination of LVEF. Previous observations of impaired long axis function with preserved LVEF in various cardiovascular pathologies [1, 2, 8–10] can thus be explained by a relatively small increase in $E_{cc_{endo}}$, which would present as an even smaller increase in the more commonly measured mid-wall circumferential strain. Alternatively, a small, less detectable, decline in LVEF may be present with maintained E_{cc}. In these

situations, the associated small absolute changes in LVEF or E_{cc} are more difficult to measure than the relatively larger changes in E_{ll}. This is reflected in the current study, where patients with Fabry disease and normal LVEF were found to have larger reduction in magnitude of $E_{ll_{avg}}$ (approximately 5% absolute change or 28% relative difference) with an associated smaller increase in $E_{cc_{avg}}$ (approximately 2% absolute change or 10% relative difference) compared to controls, which together result in a preserved LVEF.

The mechanisms for reduced longitudinal function and preserved circumferential function have been proposed to be related to endocardial dysfunction since sub-endocardial fibers are predominantly longitudinally oriented while mid-wall fibers are predominantly circumferentially oriented [3]. The mechanism for preserved circumferential function has also been linked to LV wall thickening. Assuming conservation of mass, an increase in distance between the mid-wall and endocardium will result in more circumferential endocardial strain for the same mid-wall strain [34, 35].

6.4.3 Global Strain versus Regional Strain

The proposed surface strain method is limited to measuring global strain, while conventional tissue tracking methods, such as those used for tissue tagging analysis, provide regional strain information. Previously, strain imaging with MRI has been applied largely to study regional wall motion abnormalities in diseases such as myocardial infarction [36, 37] and in the studies of physiologic phenomena such as aging [38]. While the surface strain method is not appropriate for the study of these regional phenomena, more recently several clinical strain imaging studies have also shown the importance of global values of strain in common diseases including heart failure with hypertension [1], type 2 diabetes [3], aortic regurgitation [4], hypertrophic cardiomyopathy

[5] and chemotherapy cardiotoxicity [8, 9], to name a few.

In the current study, a suitable application of surface strains is presented where patients with Fabry disease showed reduced global strain, indicating abnormal contractile function despite normal LVEF, consistent with previous studies [6, 7]. Global strains have also been shown to be sensitive to regional dysfunction and tissue damage, for example, in myocardial infarction where global longitudinal strain has been shown to be an excellent predictor of infarct size [39, 40]. Furthermore, globally measured strains are appealing for the assessment of cardiac function because they are independent of measurement location which improves reproducibility and have increased signal to noise due to the effects of averaging.

The ability to measure surface strains also offers new insight into function not provided by the mid-wall strains most commonly reported. For example, in the subjects with Fabry disease, endocardial circumferential strain was increased, relatively, by 20% but reduced by 14% on the epicardial surface compared to the control group. This provides a distinct pattern of altered strain that may less pronounced or absent with mid-wall strain.

6.4.4 Reproducibility of Surface Strain Analysis

Reproducibility for surface strains, expressed as intra-class correlation coefficients, were found to be similar to values reported using Harmonic Phase (HARP) analysis in a Multi-Center Study of Atherosclerosis (MESA) [41]. In the current study, for peak systolic E_{cc}, the correlation coefficient was 0.84 for inter-observer and 0.97 for intra-observer reproducibility. For comparison, the MESA study reported an intra-class correlation coefficient for peak systolic E_{cc} of 0.74 to 0.89 for inter-observer and 0.79 to 0.84 for intra-observer reproducibility, depending on quality of tag persistence.

6.4.5 Limitations

A limitation of the current study is that surface strains were compared to only one tissue tagging data acquisition and analysis method, and thus cannot be directly interpreted for other commonly used methods such as HARP. Also, surface radial strain could not be compared to tagging-derived strains because of insufficient tag resolution in the radial imaging dimension. Inter-study reproducibility was not measured and thus the ability of surface strains to measure small changes in strain is not yet fully characterized. Finally, tagging data was not available for the patients with Fabry disease, and thus surface strain results in these subjects could not be directly compared to tagging-derived values.

6.4.6 Conclusions

Surface measurements of E_{cc}, E_{ll} and E_{rr} are possible with no specialized acquisition protocols and minimal additional post-processing when applied as an addition to conventional method of disks volume analysis. Peak systolic global circumferential and longitudinal strain values were found to agree well with MRI tissue tagging and with good inter- and intra-observer reproducibility. Global strains were shown to be abnormal in a group of subjects with Fabry disease despite normal LVEF, demonstrating the presence of impaired global function measured with surface strains that cannot be detected using LVEF. This technique can be implemented for any standard volumetric cine study, including retrospective analysis of previously acquired data sets.

6.5 Chapter 6 References

[1] Kosmala W, Plaksej R, Strotmann JM, Weigel C, Herrmann S, Niemann M, Mende H, Stork S, Angermann CE, Wagner JA, and Weidemann F. Progression of left ventricular functional abnormalities in hypertensive patients with heart failure: an ultrasonic two-dimensional speckle tracking study. *J Am Soc Echocardiogr*, 21:1309–17, 2008.

[2] Eleid MF, Caracciolo G, Cho EJ, Scott RL, Steidley DE, Wilansky S, Arabia FA, Khandheria BK, and Sengupta PP. Natural history of left ventricular mechanics in transplanted hearts: relationships with clinical variables and genetic expression profiles of allograft rejection. *JACC Cardiovasc Imaging*, 3:988–1000, 2010.

[3] Ng AC, Delgado V, Bertini M, van der Meer RW, Rijzewijk LJ, Hooi Ewe S, Siebelink HM, Smit JW, Diamant M, Romijn JA, de Roos A, Leung DY, Lamb HJ, and Bax JJ. Myocardial steatosis and biventricular strain and strain rate imaging in patients with type 2 diabetes mellitus. *Circulation*, 122(24):2538–44, 2010.

[4] Smedsrud MK, Pettersen E, Gjesdal O, Svennevig JL, Andersen K, Ihlen H, and Edvardsen T. Detection of left ventricular dysfunction by global longitudinal systolic strain in patients with chronic aortic regurgitation. *J Am Soc Echocardiogr*, 24(11):1253–9, 2011.

[5] Saito M, Okayama H, Yoshii T, Higashi H, Morioka H, Hiasa G, Sumimoto T, Inaba S, Nishimura K, Inoue K, Ogimoto A, Shigematsu Y, Hamada M, and Higaki J. Clinical significance of global two-dimensional strain as a

surrogate parameter of myocardial fibrosis and cardiac events in patients with hypertrophic cardiomyopathy. *Eur Heart J Cardiovasc Imaging*, 13(7):617–23, 2011.

[6] Weidemann F, Breunig F, Beer M, Sandstede J, Stork S, Voelker W, Ertl G, Knoll A, Wanner C, and Strotmann JM. The variation of morphological and functional cardiac manifestation in Fabry disease: potential implications for the time course of the disease. *Eur Heart J*, 26(12):1221–7, 2005.

[7] Weidemann F, Niemann M, Breunig F, Herrmann S, Beer M, Stork S, Voelker W, Ertl G, Wanner C, and Strotmann J. Long-term effects of enzyme replacement therapy on Fabry cardiomyopathy: evidence for a better outcome with early treatment. *Circulation*, 119(4):524–9, 2009.

[8] Fallah-Rad N, Walker JR, Wassef A, Lytwyn M, Bohonis S, Fang T, Tian G, Kirkpatrick ID, Singal PK, Krahn M, Grenier D, and Jassal DS. The utility of cardiac biomarkers, tissue velocity and strain imaging, and cardiac magnetic resonance imaging in predicting early left ventricular dysfunction in patients with human epidermal growth factor receptor II-positive breast cancer treated with adjuvant trastuzumab therapy. *J Am Coll Cardiol*, 57(22):2263–70, 2011.

[9] Ho E, Brown A, Barrett P, Morgan RB, King G, Kennedy MJ, and Murphy RT. Subclinical anthracycline- and trastuzumab-induced cardiotoxicity in the long-term follow-up of asymptomatic breast cancer survivors: a speckle tracking echocardiographic study. *Heart*, 96(9):701–7, 2010.

[10] Stanton T, Leano R, and Marwick TH. Prediction of all-cause mortality

from global longitudinal speckle strain: comparison with ejection fraction and wall motion scoring. *Circ Cardiovasc Imaging*, 2(5):356–64, 2009.

[11] Heimdal A, Stoylen A, Torp H, and Skjaerpe T. Real-time strain rate imaging of the left ventricle by ultrasound. *J Am Soc Echocardiogr*, 11(11):1013–9, 1998.

[12] Amundsen BH, Helle-Valle T, Edvardsen T, Torp H, Crosby J, Lyseggen E, Stylen A, Ihlen H, Lima JA, Smiseth OA, and Slrdahl SA. Noninvasive myocardial strain measurement by speckle tracking echocardiography: validation against sonomicrometry and tagged magnetic resonance imaging. *J Am Coll Cardiol*, 47:789–93, 2006.

[13] Osman NF, Kerwin WS, McVeigh ER, and Prince JL. Cardiac motion tracking using cine harmonic phase (HARP) magnetic resonance imaging. *Magn Reson Med*, 42(6):1048–60, 1999.

[14] Axel L and Dougherty L. MR imaging of motion with spatial modulation of magnetization. *Radiology*, 171:841–5, 1989.

[15] Mosher TJ and Smith MB. A DANTE tagging sequence for the evaluation of translational sample motion. *Magn Reson Med*, 15(2):334–9, 1990.

[16] Fischer SE, McKinnon GC, Maier SE, and Boesiger P. Improved myocardial tagging contrast. *Magn Reson Med*, 30(2):191–200, 1993.

[17] Pelc LR, Sayre J, Yun K, Castro LJ, Herfkens RJ, Miller DC, and Pelc NJ. Evaluation of myocardial motion tracking with cine-phase contrast magnetic resonance imaging. *Invest Radiol*, 29(12):1038–42, 1994.

[18] Aletras AH, Ding S, Balaban RS, and Wen H. DENSE: displacement en-

coding with stimulated echoes in cardiac functional MRI. *J Magn Reson*, 137(1):247–52, 1999.

[19] Osman NF, Sampath S, Atalar E, and Prince JL. Imaging longitudinal cardiac strain on short-axis images using strain-encoded MRI. *Magn Reson Med*, 46(2):324–34, 2001.

[20] Hor KN, Gottliebson WM, Carson C, Wash E, Cnota J, Fleck R, Wansapura J, Klimeczek P, Al-Khalidi HR, Chung ES, Benson DW, and Mazur W. Comparison of magnetic resonance feature tracking for strain calculation with harmonic phase imaging analysis. *JACC Cardiovasc Imaging*, 3(2):144–51, 2010.

[21] Schuster A, Kutty S, Padiyath A, Parish V, Gribben P, Danford DA, Makowski MR, Bigalke B, Beerbaum P, and Nagel E. Cardiovascular magnetic resonance myocardial feature tracking detects quantitative wall motion during dobutamine stress. *J Cardiovasc Magn Reson*, 13(1):58, 2011.

[22] Maret E, Todt T, Brudin L, Nylander E, Swahn E, Ohlsson JL, and Engvall JE. Functional measurements based on feature tracking of cine magnetic resonance images identify left ventricular segments with myocardial scar. *Cardiovasc Ultrasound*, 7:53, 2009.

[23] Morton G, Schuster A, Jogiya R, Kutty S, Beerbaum P, and Nagel E. Inter-study reproducibility of cardiovascular magnetic resonance myocardial feature tracking. *J Cardiovasc Magn Reson*, 14(1):43, 2012.

[24] Kirschbaum SW, Baks T, Gronenschild EH, Aben JP, Weustink AC, Wielopolski PA, Krestin GP, de Feyter PJ, and van Geuns RJ. Addition

of the long-axis information to short-axis contours reduces interstudy variability of left-ventricular analysis in cardiac magnetic resonance studies. *Invest Radiol*, 43:1–6, 2008.

[25] Thunberg P, Emilsson K, Rask P, and Khri A. Separating the left cardiac ventricle from the atrium in short axis MR images using the equation of the atrioventricular plane. *Clin Physiol Funct Imaging*, 28:222–8, 2008.

[26] Klein S, Staring M, Murphy K, Viergever MA, and Pluim JP. elastix: a toolbox for intensity-based medical image registration. *IEEE Trans Med Imaging*, 29(1):196–205, 2010.

[27] Ledesma-Carbayo MJ, Derbyshire JA, Sampath S, Santos A, Desco M, and McVeigh ER. Unsupervised estimation of myocardial displacement from tagged MR sequences using nonrigid registration. *Magn Reson Med*, 59:181–9, 2008.

[28] Hudsmith LE, Petersen SE, Francis JM, Robson MD, and Neubauer S. Normal human left and right ventricular and left atrial dimensions using steady state free precession magnetic resonance imaging. *J Cardiovasc Magn Reson*, 7:775–82, 2005.

[29] Grothues F, Smith GC, Moon JC, Bellenger NG, Collins P, Klein HU, and Pennell DJ. Comparison of interstudy reproducibility of cardiovascular magnetic resonance with two-dimensional echocardiography in normal subjects and in patients with heart failure or left ventricular hypertrophy. *Am J Cardiol*, 90:29–34, 2002.

[30] Peters DC, Ennis DB, and McVeigh ER. High-resolution MRI of cardiac function with projection reconstruction and steady-state free precession. *Magn Reson Med*, 48(1):82–8, 2002.

[31] Kalogeropoulos AP, Georgiopoulou VV, Gheorghiade M, and Butler J. Echocardiographic evaluation of left ventricular structure and function: new modalities and potential applications in clinical trials. *J Card Fail*, 18(2):159–72, 2012.

[32] Moore CC, Lugo-Olivieri CH, McVeigh ER, and Zerhouni EA. Three-dimensional systolic strain patterns in the normal human left ventricle: characterization with tagged MR imaging. *Radiology*, 214(2):453–66, 2000.

[33] Parisi AF, Moynihan PF, Feldman CL, and Folland ED. Approaches to determination of left ventricular volume and ejection fraction by real-time two-dimensional echocardiography. *Clin Cardiol*, 2:257–63, 1979.

[34] MacIver DH. The relative impact of circumferential and longitudinal shortening on left ventricular ejection fraction and stroke volume. *Exp Clin Cardiol*, 17(1):5–11, 2012.

[35] Aurigemma GP, Silver KH, Priest MA, and Gaasch WH. Geometric changes allow normal ejection fraction despite depressed myocardial shortening in hypertensive left ventricular hypertrophy. *J Am Coll Cardiol*, 26(1):195–202, 1995.

[36] Bogaert J, Bosmans H, Maes A, Suetens P, Marchal G, and Rademakers FE. Remote myocardial dysfunction after acute anterior myocardial infarction: impact of left ventricular shape on regional function: a magnetic resonance myocardial tagging study. *J Am Coll Cardiol*, 35(6):1525–34, 2000.

[37] Cupps BP, Bree DR, Wollmuth JR, Howells AC, Voeller RK, Rogers JG, and Pasque MK. Myocardial viability mapping by magnetic

resonance-based multiparametric systolic strain analysis. *Ann Thorac Surg*, 86(5):1546–53, 2008.

[38] Fonseca CG, Oxenham HC, Cowan BR, Occleshaw CJ, and Young AA. Aging alters patterns of regional nonuniformity in LV strain relaxation: a 3-D MR tissue tagging study. *Am J Physiol Heart Circ Physiol*, 285(2):H621–30, 2003.

[39] Gjesdal O, Hopp E, Vartdal T, Lunde K, Helle-Valle T, Aakhus S, Smith HJ, Ihlen H, and Edvardsen T. Global longitudinal strain measured by two-dimensional speckle tracking echocardiography is closely related to myocardial infarct size in chronic ischaemic heart disease. *Clin Sci (Lond)*, 113(6):287–96, 2007.

[40] Vartdal T, Brunvand H, Pettersen E, Smith HJ, Lyseggen E, Helle-Valle T, Skulstad H, Ihlen H, and Edvardsen T. Early prediction of infarct size by strain Doppler echocardiography after coronary reperfusion. *J Am Coll Cardiol*, 49(16):1715–21, 2007.

[41] Castillo E, Osman NF, Rosen BD, El-Shehaby I, Pan L, Jerosch-Herold M, Lai S, Bluemke DA, and Lima JA. Quantitative assessment of regional myocardial function with MR-tagging in a multi-center study: interobserver and intraobserver agreement of fast strain analysis with harmonic phase (HARP) MRI. *J Cardiovasc Magn Reson*, 7(5):783–91, 2005.

Chapter 7

Discussion and Conclusions

7.1 Limitations and Future Directions

7.1.1 MRI for the Evaluation of Diastolic Function

Cardiac Arrhythmias

Gated-segmented imaging uses information from several heartbeats to reconstruct a single cardiac cycle. Implicit in this imaging strategy is the assumption that each cardiac cycle is the same. While this is a good approximation when subjects are in sinus rhythm, cardiac arrhythmias are not uncommon. Atrial fibrillation (AF), the most common cardiac arrhythmia, affects approximately 1% of the general population and is higher for the elderly and for those with cardiac disease [1]. It is of particular interest to this thesis because it is associated with diastolic dysfunction and is common amongst patient populations of interest [2]. Figure 7.1 shows an example of an image from a subject with AF compared to one in sinus rhythm. Notice that, in AF, the edges of the myocardium are less well defined than in sinus rhythm, as indicated by arrows.

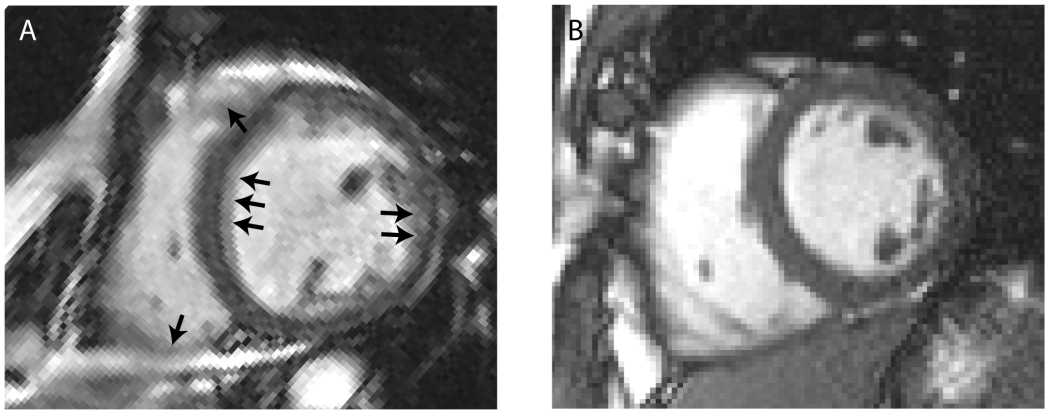

Figure 7.1: Comparison of (A) a subject with atrial fibrillation and (B) one in sinus rhythm.

The direct application of standard cine imaging to subjects with arrhythmia will result in artifacts with the extent of the artifacts depending on the specific nature of the arrhythmia. Arrhythmia rejection can be applied to improve image quality [3]. With this technique, the duration of each heartbeat determined using the ECG tracing is analyzed, and only heartbeats within an acceptance window are used. The disadvantage of this technique is that, by rejecting some heartbeats, the total acquisition time increases. Not only does this extend the length of the exam, but it also increases the duration of a single acquisition, possibly beyond the length of a comfortable breath-hold. In this case, temporal and/or spatial resolution can be sacrificed to shorten the acquisition.

Real-time imaging is another technique that can be applied to image subjects with arrthymias [3]. Real-time imaging refers to acquiring the entire image at once as opposed to segmented imaging where a single image is acquired over multiple heartbeats and then stitched together. The disadvantage of acquiring real-time images is that it takes much longer to acquire an entire image compared to acquiring only a portion of the image. Real-time cines thus have lower temporal resolution and spatial resolution must also be reduced to

minimize acquisition times.

For patients with AF, another strategy is to acquire the cine using prospective gating as opposed to retrospective gating. Prospective gating refers to imaging synchronized with the ECG signal; imaging starts at the peak of the ECG R-wave and finishes before the end of the shortest R-R interval, with the final portion of each heartbeat discarded. Image quality is improved because the earlier portion of the cardiac cycle tends to be more regular. The trade-off is that the entire cardiac cycle is not captured. If image quality is still not adequate, temporal and spatial resolution can again be sacrificed to acquire the images over fewer heartbeats, reducing the possibility of anomalous beats. Despite these modifications, image quality is still usually lower, and it is possible that images supposedly acquired at end-systole and end-diastole reflect these cardiac phases less accurately. Despite these limitations, analysis of heart volumes and mass in patients with AF has been shown to be accurate [4] and reproducible [5].

The surface strain technique introduced in Chapter 6 for the measurement of global left ventricular strain would be well suited for application in patients with arrhythmia. Conventional tissue tracking techniques such as tissue tagging [6] or feature tracking [7] are dependent on ideal imaging quality [8]. Surface strains, while likely still influenced by imaging quality, is an extension of LV volume analysis which has been shown to be quite robust when image quality is not ideal [4, 5]. This hypothesis would need to be verified by measuring inter-observer and intra-observer surface strain reproducibility in subject with AF compared to subjects in sinus rhythm. Ideally, inter-study reproducibility should also be evaluated by scanning the subject twice and asking him/her to get up off the bed between scans. An interesting comparison would be between these results and speckle tracking echocardiography [9]

which is a real-time technique and is thus not compromised by beat-to-beat variations. This comparison would also be valuable because speckle tracking is a commonly used technique for strain imaging.

Temporal Resolution

The temporal resolution of the pulse sequences used in this thesis were approximately 25 ms for tissue tagging, 30–40 ms for SSFP imaging, and 30–60 ms for phase contrast imaging. Many diastolic phenomena occur over time intervals similar to these temporal resolutions, imposing limits on the characterization of fast diastolic events. Phase contrast MRI is the slowest pulse sequence used because of the time necessary for flow encoding gradients and the requirement for 2 flow encoding steps. Newer phase contrast sequences are more time-efficient and use parallel imaging to substantially improve temporal resolution [10].

Throughout this thesis, blood velocity from PC MRI was used to measure mitral valve opening and aortic valve closure times. This was achieved by linearly extrapolating to zero or no flow conditions. Better temporal resolution phase contrast would improve confidence in these measures. In Chapter 3, blood velocity and flow time-courses were measured. The E/A ratio is likely less influenced by temporal resolution because a similar blunting of peak values for both filling waves would be minimized by taking a ratio. However, the measurement of deceleration time involves fitting a line to the downslope of the E-wave and would likely benefit from a better temporally defined peak and end.

A worthwhile endeavour would be to apply higher temporal resolution phase contrast for investigation of propagation velocity in the LA, introduced in Chapter 4, in patient groups. In this chapter, it was reasoned that shorter

temporal delays would be measured in patients with increased LA stiffness. This means that these measurements are more difficult in patient groups than in healthy subjects, necessitating better temporal resolution.

Temporal resolution is also a limitation for the determination of pressure gradients and differences in Chapter 5. The calculation of the inertial component of the pressure gradient requires the differentiation of velocity data over time. It has been shown that a minimum temporal resolution of approximately 44 ms is required to avoid underestimation of the inertial component [11]. Thus, it is likely pressure gradients are underestimated in acquisitions with lower temporal resolution.

Spatial Resolution

Phase contrast sequences are also limited by their spatial resolution. Lower spatial resolution is often a necessary trade-off in order to maintain large fields of view (required for cardiac imaging), sufficient temporal resolution and acquisitions times within reasonable breath-hold durations. As described above, phase contrast MRI is a slow pulse sequence due to its requirement for 2 phase encoding steps. Parameters used for phase contrast in this thesis were approximately 75 phase encoding steps for a field of view of 25 cm in that direction, resulting in an acquired spatial resolution of 3.3 mm. Volume averaging would be expected to be a confounder near chamber walls and its effect is uncertain for complex flow patterns such as the vorticies that form behind the mitral leaflets toward the end of the E-wave. Fortunately, volume averaging is unlikely to be a problem in the more central portion of the LV chamber (the focus of this thesis) where blood velocities vary slowly over space [12].

Poor spatial resolution also impedes the measurement of myocardial tis-

sue velocities, an important echocardiography parameter of diastolic function [13]. The thickness of the left ventricular myocardium is approximately 1 cm at end-diastole [14], which means that only 1 or 2 pixels contain myocardium with the current resolution. Tissue velocities were not measured in this thesis, but with the implementation of a faster phase contrast sequence, better spatial resolution could be acquired enabling tissue velocity measures from the same images used to measure blood velocities. Tissue velocities would provide complimentary information without additional image acquisition.

Common practice in cardiac MRI is to acquire images with an 8 mm slice thickness. Standard imaging views (eg. 4-chamber, 2-chamber) are acquired by intersecting the center of the LA and LV chambers. As a result, partial voluming is minimized because anatomy and velocities are generally constant over the thickness of these centrally placed slices. However, misplacement of the slice or abnormal anatomy may introduce errors due to partial voluming.

Background Phase

Phase contrast is a quantitative imaging technique which uses phase to determine velocity. Differences in eddy currents between flow encoding steps leads to background phase effects that do not represent velocity [15]. This problem is most important when velocities are integrated over space and time to determine the volume of flow because it results in an accumulation of errors. In this thesis, volumes were not determined, avoiding this more serious error, and only blood velocity and flow time-courses were investigated. In these cases, residual background phase results in velocity or flow offsets but does not change the shape of the time curves.

7.1.2 Physiological Determinants of Diastolic Function

A limitation of many cardiac exams, including cardiac MRI, is that the evaluation of cardiac performance is obtained only at a single instance in time. Most parameters of cardiac function depend on a number of factors that fluctuate continuously such as hydration level, body position, heart rate, sympathetic and parasympathetic tone. Thus, cardiac parameters measured during an exam represent only the current loading conditions. Ratios such as E/A [16] and E/E′ [13] have been shown to be less load dependent, and some parameters such as myocardial mass are independent of loading conditions. Heart rate and exercise are important physiological considerations and are discussed in further detail below.

Heart Rate Dependence

Sinus tachycardia refers to a rapid heart rate, for example, during exercise, and is an important limitation of blood velocity parameters of diastolic function. At high heart rates, the E-wave and A-wave begin to overlap, eventually resulting in complete fusion of the 2 filling waves [17]. This occurs at lower heart rates for subjects with impaired relaxation [18]. As a result, the E/A ratio and deceleration time cannot be determined. These parameters assume that the E-wave is independent of atrial contraction and that the A-wave occurs when the LV is fully relaxed. The overlap of filling waves precludes this assumption. In Chapters 3 and 4, only subjects with distinct E- and A-waves were studied since overlap in these filling waves would have produced meaningless results.

An opportunity for future study of diastolic function in subjects with sinus tachycardia would be to use tissue deformation parameters or pressure

gradients. Tissue velocities and parameters of strain are less limited by heart rate because their time-courses occurs over a short time-durations, during the upslope of the early and late filling waves, resulting in little or no overlap at higher heart rates. Similarly, pressure gradients peak during the upslope of the velocity-time curve and were found in Chapter 5 to represent filling velocity.

Exercise

Exercise intolerance is an eventual consequence of all cardiac diseases and has severe implications for quality of life. During exercise, metabolic demands increase and both systolic and diastolic function must respond to meet the demands of exertion [18]. Hearts that appear normal when at rest can show signs of dysfunction when stressed. This is particularly true early in disease, which makes it difficult to detect cardiac dysfunction during a resting exam. For these reasons, the study of diastolic function during exercise is an important area for further research. It would be interesting to surface strain, introduced in Chapter 6, in patient populations during exercise. However, cardiac MRI is not well suited to examinations during exercise for several reasons; exams are typically performed while the subject is lying down and motion must be minimized. This imposes limitations on the type of exercise that can be performed. Solutions include pharmacological stress which can mimic certain aspects of exercise, performing exercise immediately prior to an MRI exam or low-intensity exercise that can be performed while supine in the MRI scanner. As mentioned above, concepts studied in Chapters 3 and 4 would be hindered by elevated heart rates during exercise.

7.1.3 Sample Size

Small sample sizes were used throughout the studies presented in this thesis. While the results from theses studies are useful as a "proof of concept", the small sample sizes limit their general applicability. Futher studies, which include larger groups and more varied physiology and pathology, are required to increase understanding of the proposed diastolic parameters and to establish normal population values.

7.1.4 Application in Patient Populations

The measures of diastolic function, volumetric flow rate in Chapter 3, LA propagation velocity in Chapter 4, pressure gradients in Chapter 5 and surface strains in Chapter 6, presented in this thesis would benefit from further study in other patients groups and physiological conditions. The value of global strain has already been shown in many clinical studies [19–26].

The value of volumetric flow rate and LA propagation velocity are less certain. Both these measures are appealing; volumetric flow is an integrated measure which improves signal to noise, is less dependent on slice prescription and represents global function of the heart, and LA propagation velocity may give a measure of LA chamber compliance, an important parameter that cannot be measured non-invasively. However, it is necessary to more firmly establish the relationship between these measures and the physical mechanisms governing diastolic function. This can be achieved by the study of these parameters in aging, under varying loading conditions and in disease.

Both intra-ventricular and atrio-ventricular pressure differences were found to reflect early filling velocity, limiting their usefulness. However, spatial information in the raw pressure gradient field is lost when integrated to yield

the resulting pressure difference. Therefore, continued study of the pressure gradient field still warrants further investigation.

7.1.5 The Future of MRI for Diastolic Function

More developments are necessary for MRI to become widely adopted for the evaluation of diastolic function both in research and clinically. There are many image contrasts available to MRI and even more variants to pulse sequences and pulse sequence parameters. These options allow for researchers and clinicians to customize exams to specific studies and patients. However, many pulse sequence variants are not widely available and thus cannot be adopted for use in most centers. Variations in techniques and parameters measured also make it difficult to compare results from different studies. The development of a streamlined and time-efficient diastolic MRI exam using widely available pulse sequences with accompanying normal reference values as a function of age and gender would be a valuable asset for establishing guidelines and furthering progress in this field.

Since current assessment of diastolic function is performed using echocardiography, common diastolic parameters measured generally take advantage of the strengths of cardiac ultrasound. Similarly, the most useful diastolic parameters for a cardiac MRI exam should consider both the importance of the diastolic mechanisms modulating the parameter as well as the precision and accuracy of MRI in measuring the parameter. Of the measures studied in this thesis, volumetric mitral blood flow and surface strains likely represent important physiologic phenomena that can be reliably measured using MRI. While LA propagation velocity likely represents the important mechanisms of LA compliance and, by extension, LA pressure, the reliablility of this measurement has not yet been established. Peak early filling pressure gradients

and differences do not appear to offer additional insight into diastolic performance. While the parameters described above represent many aspects of diastolic function, one important parameter that was not studied in this thesis was the ratio of peak early filling blood and mitral annular velocities (E/E'). E/E' is considered one of the most valuable echocardiography-derived diastolic parameters and represents filling pressures. Based on the experience of using phase contrast velocity imaging in the applications presented here, it is likely that tissue velocity can be reliably imaged if spatial resolution can be improved, providing another potential cardiac MRI measure of diastolic function.

Along with developing guidelines for a diastolic MRI exam, it will be important to establish the reproducibility of MRI-derived diastolic parameters, including inter-observer, intra-observer and inter-study reproducibility. Inter-study reproducibility is perhaps one of the greatest strengths of MRI over echocardiography but is not often studied. MRI has superior spatial coverage and unlimited imaging windows. Unrestricted imaging windows improves inter-study reproducibility because consistency in image orientation and spatial placement can be ensured between subjects without restrictions imposed by acoustic window. Spatial coverage improves reproducibility because surrounding landmarks can be used to more accurately localize measurements. For example, in Chapters 3, 4 and 5, slice prescriptions were made as similar as possible between subjects and measurement locations were prescribed retrospectively to ensure consistency between subjects.

Another advantage is that the absolute location of any image acquired using MRI relative to a static frame of reference is known as opposed to echocardiography where measurements are only known relative to the mobile ultrasound transducer. This allows, for example, for the acquisition of evenly

spaced parallel slices using MRI. This feature is used to determine chamber volumes using disk summation, the current gold standard [27, 28], and was also used in Chapter 6 for the calculation of surface strain. It will be important in future work to experimentally demonstrate these advantages in the context of diastolic function by measuring inter-study variability. If it can be established that MRI has superior inter-study variability, the use of MRI for parameters of diastolic function becomes more appealing. This is particularly true for research where sample sizes can be reduced.

Imaging assessment of diastolic function has largely focused on blood and tissue velocities, likely because those are measurements available to echocardiography, the more established tool for evaluation of diastolic function. However, MRI offers other information that can provide context for the study of diastolic function, including gadolinium late enhancement imaging for imaging myocardial scar [29], T_2 weighted imaging for myocardial edema [30] and T_1 imaging for diffuse fibrosis [31] which are all related to reduced cardiac performance. The imaging of lung water can also be performed [32], which can result from elevated pulmonary pressures related to diastolic dysfunction. Important future work will be to study the relationship between these phenomena and diastolic performance.

However, it is likely that even with continued development of cardiac MRI for diastolic function, echocardiography will remain an important imaging tool due to its accessibility and ease of use. In this context, MRI can also be a used to improve echocardiographic measures of diastolic function. Complex spatially varying phenomena are best studied using the more complete spatial coverage offered by MRI. However, once abnormal features are identified and understood, key parameters, measurable using echocardiography, can be developed to identify and represent the more complex phenomena.

7.2 Conclusions

MRI is a safe and non-invasive tool that can be used to study and evaluate diastolic function. Up to now, imaging of diastolic function has largely been performed using echocardiography. However, limitations of spatial coverage and acoustic windows do not allow for the study of certain aspects of diastolic function. MRI offers additional tools for the more complete spatial characterization of diastolic function. In this thesis, MRI was used to study several aspects of diastolic function including myocardial deformation and blood velocity patterns.

The deformation of the entire myocardium during isovolumic relaxation was measured, and the results offered an explanation for experimentally observed volume changes during this interval related to the inward bowing of the mitral valve leaflets. Results suggested that values of isovolumic strain depend on relaxation properties of the LV as well as the material and functional properties of the mitral leaflets. Deformation of the myocardium was also used to develop a method for the measurement of global strain, termed surface strain. Diastolic blood velocity at the mitral valve leaflets are the starting point for the standard evaluation of diastolic function. Using the spatial coverage of MRI, volumetric mitral blood flow and left atrial blood velocities were characterized and offered new blood velocity based measures of diastolic function. Finally, both intra-ventricular and atrio-ventricular pressure differences were found to reflect peak values of blood velocity. Further development of MRI for the study of diastolic function will benefit from faster pulse sequences, standardization of data acquisition and analysis and the evaluation of the reproducibility of MRI-derived diastolic parameters.

7.3 Chapter 7 References

[1] Go AS, Hylek EM, Phillips KA, Chang Y, Henault LE, Selby JV, and Singer DE. Prevalence of diagnosed atrial fibrillation in adults: national implications for rhythm management and stroke prevention: the anticoagulation and risk factors in atrial fibrillation (ATRIA) study. *JAMA*, 285:2370–5, 2001.

[2] Nagueh SF, Appleton CP, Gillebert TC, Marino PN, Oh JK, Smiseth OA, Waggoner AD, Flachskampf FA, Pellikka PA, and Evangelisa A. Recommendations for the evaluation of left ventricular diastolic function by echocardiography. *Eur J Echocardiogr*, 10:165–93, 2009.

[3] Lee VS. *Cardiovascular MR Imaging: Physical Principles to Practical Protocols*. Lippincott Williams and Wilkins, 2005.

[4] Hundley WG, Meshack BM, Willett DL, Sayad DE, Lange RA, Willard JE, Landau C, Hillis LD, and Peshock RM. Comparison of quantitation of left ventricular volume, ejection fraction, and cardiac output in patients with atrial fibrillation by cine magnetic resonance imaging versus invasive measurements. *Am J Cardiol*, 78:1119–23, 1996.

[5] Sievers B, Kirchberg S, Addo M, Bakan A, Brandts B, and Trappe HJ. Assessment of left atrial volumes in sinus rhythm and atrial fibrillation using the biplane area-length method and cardiovascular magnetic resonance imaging with TrueFISP. *J Cardiovasc Magn Reson*, 6:855–63, 2004.

[6] Axel L and Dougherty L. MR imaging of motion with spatial modulation of magnetization. *Radiology*, 171:841–5, 1989.

[7] Maret E, Todt T, Brudin L, Nylander E, Swahn E, Ohlsson JL, and Engvall JE. Functional measurements based on feature tracking of cine magnetic resonance images identify left ventricular segments with myocardial scar. *Cardiovasc Ultrasound*, 7:53, 2009.

[8] Castillo E, Osman NF, Rosen BD, El-Shehaby I, Pan L, Jerosch-Herold M, Lai S, Bluemke DA, and Lima JA. Quantitative assessment of regional myocardial function with MR-tagging in a multi-center study: interobserver and intraobserver agreement of fast strain analysis with harmonic phase (HARP) MRI. *J Cardiovasc Magn Reson*, 7(5):783–91, 2005.

[9] Amundsen BH, Helle-Valle T, Edvardsen T, Torp H, Crosby J, Lyseggen E, Stylen A, Ihlen H, Lima JA, Smiseth OA, and Slrdahl SA. Noninvasive myocardial strain measurement by speckle tracking echocardiography: validation against sonomicrometry and tagged magnetic resonance imaging. *J Am Coll Cardiol*, 47:789–93, 2006.

[10] Baltes C, Kozerke S, Hansen MS, Pruessmann KP, Tsao J, and Boesiger P. Accelerating cine phase-contrast flow measurements using k-t BLAST and k-t SENSE. *Magn Reson Med*, 54:1430–8, 2005.

[11] Thompson RB and McVeigh ER. Fast measurement of intracardiac pressure differences with 2d breath-hold phase-contrast mri. *Magn Reson Med*, 49:1056–66, 2003.

[12] Kilner PJ, Yang GZ, Wilkes AJ, Mohiaddin RH, Firmin DN, and Yacoub MH. Asymmetric redirection of flow through the hearts. *Nature*, 404:759–61, 2000.

[13] Nagueh SF, Middleton KJ, Kopelen HA, Zoghbi WA, and Quiones MA. Doppler tissue imaging: a noninvasive technique for evaluation of left ventricular relaxation and estimation of filling pressures. *J Am Coll Cardiol*, 30:1527–33, 1997.

[14] Salton CJ, Chuang ML, O'Donnell CJ, Kupka MJ, Larson MG, Kissinger KV, Edelman RR, Levy D, and Manning WJ. Gender differences and normal left ventricular anatomy in an adult population free of hypertension. a cardiovascular magnetic resonance study of the framingham heart study offspring cohort. *J Am Coll Cardiol*, 39:1055–60, 2002.

[15] Rolf MP, Hofman MB, Gatehouse PD, Markenroth-Bloch K, Heymans MW, Ebbers T, Graves MJ, Totman JJ, Werner B, van Rossum AC, Kilner PJ, and Heethaar RM. Sequence optimization to reduce velocity offsets in cardiovascular magnetic resonance volume flow quantification–a multi-vendor study. *J Cardiovasc Magn Reson*, 13:18, 2011.

[16] Downes TR, Nomeir AM, Stewart K, Mumma M, Kerensky R, and Little WC. Effect of alteration in loading conditions on both normal and abnormal patterns of left ventricular filling in healthy individuals. *Am J Cardiol*, 65:377–82, 1990.

[17] Appleton CP. Influence of incremental changes in heart rate on mitral flow velocity: assessment in lightly sedated, conscious dogs. *J Am Coll Cardiol*, 17:227–36, 1991.

[18] Kitzman DW, Higginbotham MB, Cobb FR, Sheikh KH, and Sullivan MJ. Exercise intolerance in patients with heart failure and preserved left ventricular systolic function: failure of the Frank-Starling mechanism. *J Am Coll Cardiol*, 17:1065–72, 1991.

[19] Kosmala W, Plaksej R, Strotmann JM, Weigel C, Herrmann S, Niemann M, Mende H, Stork S, Angermann CE, Wagner JA, and Weidemann F. Progression of left ventricular functional abnormalities in hypertensive patients with heart failure: an ultrasonic two-dimensional speckle tracking study. *J Am Soc Echocardiogr*, 21:1309–17, 2008.

[20] Eleid MF, Caracciolo G, Cho EJ, Scott RL, Steidley DE, Wilansky S, Arabia FA, Khandheria BK, and Sengupta PP. Natural history of left ventricular mechanics in transplanted hearts: relationships with clinical variables and genetic expression profiles of allograft rejection. *JACC Cardiovasc Imaging*, 3:988–1000, 2010.

[21] Ng AC, Delgado V, Bertini M, van der Meer RW, Rijzewijk LJ, Hooi Ewe S, Siebelink HM, Smit JW, Diamant M, Romijn JA, de Roos A, Leung DY, Lamb HJ, and Bax JJ. Myocardial steatosis and biventricular strain and strain rate imaging in patients with type 2 diabetes mellitus. *Circulation*, 122(24):2538–44, 2010.

[22] Smedsrud MK, Pettersen E, Gjesdal O, Svennevig JL, Andersen K, Ihlen H, and Edvardsen T. Detection of left ventricular dysfunction by global longitudinal systolic strain in patients with chronic aortic regurgitation. *J Am Soc Echocardiogr*, 24(11):1253–9, 2011.

[23] Saito M, Okayama H, Yoshii T, Higashi H, Morioka H, Hiasa G, Sumimoto T, Inaba S, Nishimura K, Inoue K, Ogimoto A, Shigematsu Y, Hamada M, and Higaki J. Clinical significance of global two-dimensional strain as a surrogate parameter of myocardial fibrosis and cardiac events in patients with hypertrophic cardiomyopathy. *Eur Heart J Cardiovasc Imaging*, 13(7):617–23, 2011.

[24] Fallah-Rad N, Walker JR, Wassef A, Lytwyn M, Bohonis S, Fang T, Tian G, Kirkpatrick ID, Singal PK, Krahn M, Grenier D, and Jassal DS. The utility of cardiac biomarkers, tissue velocity and strain imaging, and cardiac magnetic resonance imaging in predicting early left ventricular dysfunction in patients with human epidermal growth factor receptor II-positive breast cancer treated with adjuvant trastuzumab therapy. *J Am Coll Cardiol*, 57(22):2263–70, 2011.

[25] Ho E, Brown A, Barrett P, Morgan RB, King G, Kennedy MJ, and Murphy RT. Subclinical anthracycline- and trastuzumab-induced cardiotoxicity in the long-term follow-up of asymptomatic breast cancer survivors: a speckle tracking echocardiographic study. *Heart*, 96(9):701–7, 2010.

[26] Stanton T, Leano R, and Marwick TH. Prediction of all-cause mortality from global longitudinal speckle strain: comparison with ejection fraction and wall motion scoring. *Circ Cardiovasc Imaging*, 2(5):356–64, 2009.

[27] Bellenger NG, Davies LC, Francis JM, Coats AJ, and Pennell DJ. Reduction in sample size for studies of remodeling in heart failure by the use of cardiovascular magnetic resonance. *Cardiovasc Magn Reson*, 2:271–8, 2000.

[28] Pennell DJ. Ventricular volume and mass by CMR. *J Cardiovasc Magn Reson*, 4:507–13, 2002.

[29] Green JJ, Berger JS, Kramer CM, and Salerno M. Prognostic value of late gadolinium enhancement in clinical outcomes for hypertrophic cardiomyopathy. *JACC Cardiovasc Imaging*, 5:370–7, 2012.

[30] Carbone I and Friedrich MG. Myocardial edema imaging by cardiovascu-

lar magnetic resonance: current status and future potential. *Curr Cardiol Rep*, 14:1–6, 2012.

[31] Ellims AH, Iles LM, Ling LH, Hare JL, Kaye DM, and Taylor AJ. Diffuse myocardial fibrosis in hypertrophic cardiomyopathy can be identified by cardiovascular magnetic resonance, and is associated with left ventricular diastolic dysfunction. *J Cardiovasc Magn Reson*, 14:76, 2012.

[32] Hopkins SR, Levin DL, Emami K, Kadlecek S, Yu J, Ishii M, and Rizi RR. Advances in magnetic resonance imaging of lung physiology. *J Appl Physiol*, 102:1244–54, 2007.